CERN/LHCC 2001-24
LHCb TDR 6
14 September 2001

LHCb Outer Tracker

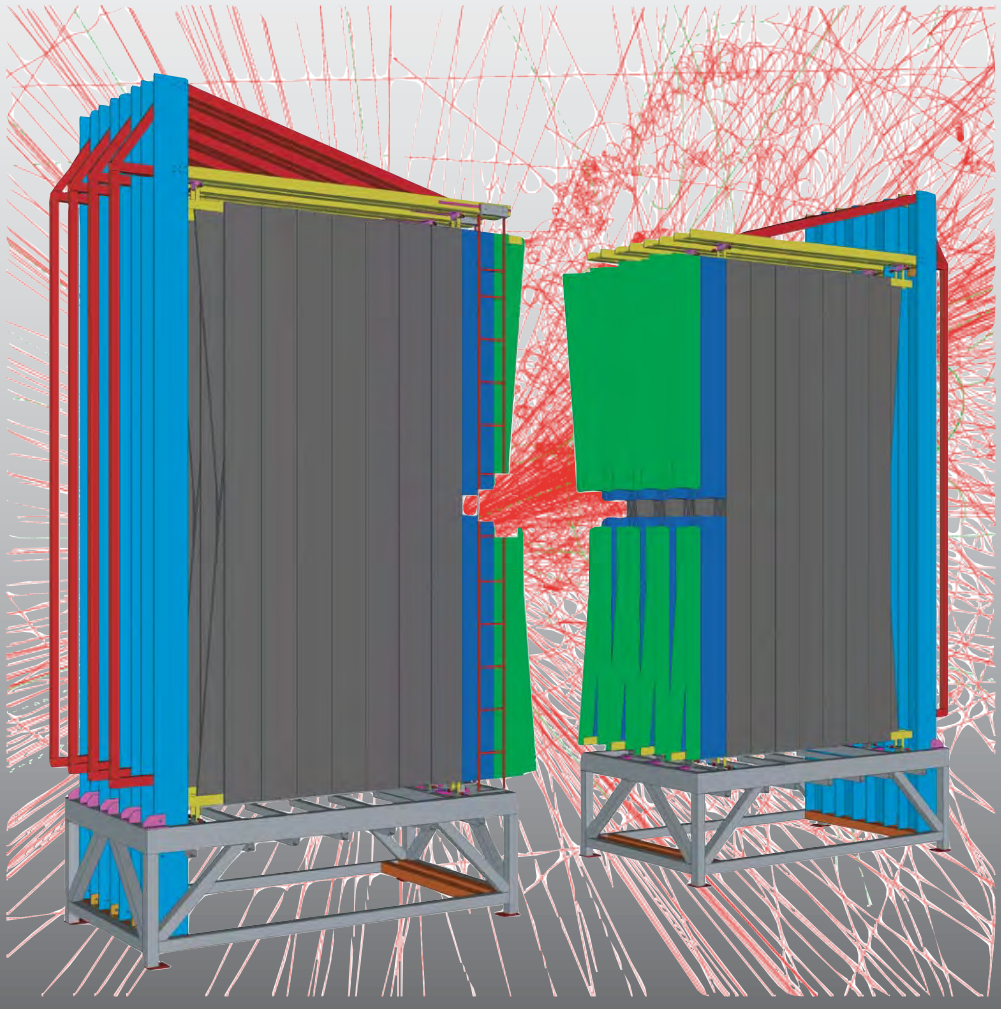

Technical Design Report

CERN/LHCC/2001-024
LHCb TDR 6
14 September 2001

LHCb

Outer Tracker Technical Design Report

Printed at CERN
Geneva, 2001
ISBN 92-9083-200-2

The LHCb Collaboration[1]

Brasilian Center for particles physics, CBPF, Rio de Janeiro, Brasil
P.R.Barbosa Marinho, I.Bediaga, A.F.Barbosa, J.Magnin, J.Marques de Miranda, A.Massafferri, A.Reis, R.Silva

University of Rio de Janeiro, UFRJ, Rio de Janeiro, Brasil
S.Amato, P.Colrain, T.da Silva, J.R.T.de Mello Neto, L.de Paula, M.Gandelman, J.H.Lopes, B.Marechal, D.Moraes(1), E.Polycarpo, F.Vinci do Santos
(1) also at CERN

University of Clermont-Ferrand II, Clermont-Ferrand, France
Z.Ajaltouni, G.Bohner, V.Breton, R.Cornat, O.Deschamps, A.Falvard[1)], P.Henrard, J.Lecoq, P.Perret, C.Rimbault, C.Trouilleau[2)], A.Ziad

CPPM Marseille, Aix University-Marseille II, Marseille, France
E.Aslanides, J.P.Cachemiche, P.Y.Duval, R.Le Gac, O.Leroy, P.L.Liotard, M.Menouni, R.Potheau, A.Tsaregorodtsev, B.Viaud

University of Paris-Sud, LAL Orsay, Orsay, France
G.Barrand, C.Beigbeder-Beau, D.Breton, T.Caceres, O.Callot, Ph.Cros, B.D'Almagne, B.Delcourt, F.Fulda Quenzer, A.Jacholkowska[1)], B.Jean-Marie, J.Lefrançois, F.Machefert, V.Tocut, K.Truong, I.Videau

Technical University of Dresden, Dresden, Germany
R.Schwierz, B.Spaan

Max-Planck-Institute for Nuclear Physics, Heidelberg, Germany
C.Bauer, D.Baumeister, N.Bulian, H.P.Fuchs, T.Glebe, W.Hofmann, K.T.Knöpfle, S.Löchner, F.Sanchez Nieto, M.Schmelling, B.Schwingenheuer, E.Sexauer[3)], U.Trunk

Physics Institute, University of Heidelberg, Heidelberg, Germany
S.Bachmann, P.Bock, H.Deppe, H.B.Dreis, F.Eisele, M.Feuerstack-Raible, S.Henneberger, P.Igo-Kemenes, R.Rusnyak, U.Stange, M.Walter, D.Wiedner, U.Uwer

Kirchhoff Institute for Physics, University of Heidelberg, Heidelberg, Germany
V.Lindenstruth, R.Richter, M.W.Schulz, A.Walsch

[1]This list includes additional colleagues who made particular contributions to the work presented in this TDR.

Laboratori Nazionali dell' INFN, Frascati, Italy
G.Bencivenni, C.Bloise, F.Bossi, P.Campana, G.Capon, P.DeSimone, C.Forti, M.A.Franceschi, F.Murtas, M.Palutan, L.Passalacqua, V.Patera(1), A. Sciubba(1)
(1)also at Dipartimento di Energetica, University of Rome, "La Sapienza"

University of Bologna and INFN, Bologna, Italy
M.Bargiotti, A.Bertin, M.Bruschi, M.Capponi, I.D'Antone, S.de Castro, P.Faccioli, L.Fabbri, D.Galli, B.Giacobbe, I.Lax, U.Marconi, I.Massa, M.Piccinini, M.Poli, N.Semprini-Cesari, R.Spighi, V.Vagnoni, S.Vecchi, M.Villa, A.Vitale, A.Zoccoli

University of Cagliari and INFN, Cagliari, Italy
A.Cardini, M.Caria, A.Lai, D.Pinci, B.Saitta(1)
(1) also at CERN

University of Ferrara and INFN, Ferrara, Italy
W.Baldini, V.Carassiti, A.Cotta Ramusino, P.Dalpiaz, A.Gianoli, M.Martini, F.Petrucci, M.Savrié

University of Florence and INFN, Florence, Italy
A.Bizzeti, M.Calvetti, G.Collazuol, E.Iacopini, M.Lenti, F.Martelli, G.Passaleva, M.Veltri

University of Genoa and INFN, Genoa, Italy
S.Cuneo, F.Fontanelli, V.Gracco, P.Musico, A.Petrolini, M.Sannino

University of Milano-Bicocca and INFN, Milano, Italy
M.Alemi, T.Bellunato(1), M.Calvi, C.Matteuzzi, M.Musy, P.Negri, M.Paganoni, C.Piazzoni
(1) also at CERN

University of Rome, "La Sapienza" and INFN, Rome, Italy
G.Auriemma(1), V.Bocci, C.Bosio, D.Fidanza(1), A.Frenkel, K.Harrison, G.Martellotti, S.Martinez, G.Penso, G.Pirozzi, R.Santacesaria, C.Satriano(1), A.Satta
(1) also at University of Basilicata, Potenza

University of Rome, "Tor Vergata" and INFN, Rome, Italy
G.Carboni, D.Domenici, G.Ganis, R.Messi, L.Pacciani, L.Paoluzi, E.Santovetti

NIKHEF, The Netherlands
G.van Apeldoorn(1,3), R. Arink(1), N.van Bakel(1,2), T.S.Bauer(1,4), A.Berkien(1), E. van den Born(1), J.F.J. van den Brand(1,2), H.J.Bulten(1,2), C.Carloganu (1), L. Ceelie(1), M.Doets(1), R.van der Eijk(1), I.Gouz(1,5), V.Gromov(1), R.Hierck(1), L.Hommels(1), E.Jans(1), T.Ketel(1,2), S.Klous (1,2), B.Koene(1), H.Kruiper(1), M.Merk(1), F.Mul(2), M.Needham(1), O.van Petten(1),

H.Schuijlenburg(1), T.Sluijk(1), J. Stolte(1), J.van Tilburg(1), H.de Vries(1), L.Wiggers(1), R. van Wijk(1), M.Zupan(1), A.Zwart(1)
(1) Foundation of Fundamental Research of Matter in the Netherlands,
(2) Free University Amsterdam,
(3) University of Amsterdam,
(4) University of Utrecht,
(5) On leave from Protvino

Institute of High Energy Physics, Beijing, P.R.C.
C.Gao, C.Jiang, H.Sun, Z.Zhu

Research Centre of High Energy Physics, Tsinghua University, Beijing, P.R.C.
M.Bisset, J.P.Cheng, Y.G.Cui, Y.Gao, H.J.He, Y.P.Kuang, Q.Li, Y.J.Li, Y.Liao, J.P.Ni, B.B.Shao,J.J.Su, Y.R.Tian, Q.Wang, Q.S.Yan

Institute for Nuclear Physics and University of Mining and Metalurgy, Krakow, Poland
E.Banas, J.Blocki, K.Galuszka, L.Hajduk, P.Jalocha, P.Kapusta, B.Kisielewski, W.Kucewicz, T.Lesiak, J.Michalowski, B.Muryn, Z.Natkaniec, W.Ostrowicz, G.Polok, E.Rulikowska-Zarebska, M.Stodulski, T.Szumlak, M.Witek(1), P.Zychowski
(1) also at CERN

Soltan Institute for Nuclear Physics, Warsaw, Poland
M.Adamus, A.Chlopik, Z.Guzik, J.Mendys, A.Nawrot, M.Szczekowski

Horia Hulubei-National Institute for Physics and Nuclear Engineering (IFIN-HH), Bucharest-Magurele, Romania
D.V.Anghel[4)], C.Coca, A.Cimpean, G.Giolu, C.Magureanu, S.Popescu, T.Preda, A.M.Rosca(1), V.L.Rusu[5)]
(1) also at Humbolt University, Berlin

Institute for Nuclear Research (INR), Moscow, Russia
V.Bolotov, S.Filippov, J.Gavrilov, E.Guschin, V.Kloubov, L.Kravchuk, S.Laptev, V.Laptev, V.Postoev, A.Sadovski, I.Semeniouk

Institute of Theoretical and Experimental Physics (ITEP), Moscow, Russia
S.Barsuk, I.Belyaev (1), A.Golutvin, O.Gouchtchine, V.Kiritchenko, V.Kochetkov, I.Korolko(1), G.Pakhlova, N.Levitski, A.Morozov, P.Pakhlov, D.Roussinov, V.Rusinov, S.Semenov, A.Soldatov, E.Tarkovski
(1) also at CERN

Budker Institute for Nuclear Physics (INP), Novosibirsk, Russia
K.Beloborodov, A.Bondar, A.Bozhenok, A.Buzulutskov, S.Eidelman, V.Golubev, P,Krokovnyi, S.Oreshkin, A.Poluektov, S.Serednyakov, L.Shekhtman, B.Shwartz, Z.Silagadze, A.Sokolov, A.Vasiljev

Institute for High Energy Physics (IHEP-Serpukhov),Protvino, Russia
L.A.Afanassieva, I.V.Ajinenko, K.Beloous, V.Brekhovskikh, S.Denissov, A.V.Dorokhov, R.I.Dzhelyadin, A.Kobelev, A.K.Konoplyannikov, A.K.Likhoded, V.D.Matveev, V.Novikov, V.F.Obraztsov, A.P.Ostankov, V.I.Rykalin, V.K.Semenov, M.M.Shapkin, N.Smirnov, A.Sokolov, M.M.Soldatov, V.V.Talanov, O.P.Yushchenko

Petersburg Nuclear Physics Institute, Gatchina, St.Petersburg, Russia
B.Botchine, S.Guetz, A.Kashchuk(1), V.Lazarev, N.Saguidova, V.Souvorov(1), E.Spiridenkov, A.Vorobyov, An.Vorobyov
(1) also at CERN

University of Barcelona, Barcelona, Spain
E.Aguilo, R.Ballabriga(1), S.Ferragut, Ll.Garrido, D.Gascon, R.Graciani Diaz, S.Luengo(1), R.Miquel[6)], D.Peralta, M.Rosello(1), X.Vilasis(1)
(1) also at departament d'Engineria Electronica La Salle, Universitat Ramon Llull, Barcelona

University of Santiago de Compostela, Santiago de Compostela, Spain
B.Adeva, P.Conde, F.Gomez, J.A.Hernando, A.Iglesias, A.Lopez-Aguera, A.Pazos, M.Plo, J.M.Rodriguez, J.J.Saborido, M.J.Tobar

University of Lausanne, Lausanne, Switzerland
P.Bartalini, A.Bay, B.Carron, C.Currat, O.Dormond, F.Dürrenmatt, Y.Ermoline, R.Frei, G.Gagliardi, G.Haefeli, J.P.Hertig, P.Koppenburg, T.Nakada(1), J.P.Perroud, F.Ronga, O.Schneider, L.Studer, M.Tareb, M.T.Tran
(1) also at CERN, on leave from PSI, Villigen

University of Zürich , Zürich, Switzerland
R.Bernet, E.Holzschuh, F.Lehner, P.Sievers, O.Steinkamp, U.Straumann, A.Vollhardt, D.Wyler, M.Ziegler

Institute of Physics and Technologies, Kharkiv, Ukraine
A.Dovbnya, S.Maznichenko, O.Omelaenko, Yu.Ranyuk, V.Shulayev

Institute for Nuclear Research, Kiev, Ukraine
V.Aushev, V.Kiva, I.Kolomiets, Yu.Pavlenko, V.Pugatch, Yu.Vasiliev, V.Zerkin

University of Bristol, Bristol, U.K.
N.H.Brook, J.E.Cole, R.D.Head, A.Phillips, A.Presland, F.F.Wilson

University of Cambridge, Cambridge, U.K.
K.George, V.Gibson, C.R.Jones, S.G.Katvars, C.Shepherd-Themistocleous, C.P.Ward, S.A.Wotton

Rutherford Appleton Laboratory, Chilton, U.K.
C.A.J.Brew[7)], C.J.Densham, S.Easo, B.Franek, J.G.V.Guy, R.N.J.Halsall, J.A.Lidbury, J.V.Morris, A.Papanestis, G.N.Patrick, F.J.P.Soler, S.A.Temple, M.L.Woodward

University of Edinburgh, Edinburgh, U.K.
S.Eisenhardt, A.Khan, F.Muheim, S.Playfer, A.Walker

University of Glasgow, Glasgow, U.K.
A.J.Flavell, A.Halley, V.O'Shea, A.Pickford, F.J.P.Soler

University of Liverpool, Liverpool, U.K.
S.Biagi, T.Bowcock, R.Gamet, M.McCubbin, C.Parkes, G.Patel, V.Wright

Imperial College, London, U.K.
G.J.Barber, D.Clark, P.Dauncey, A.Duane, M.Girone(1), J.Hassard, R.Hill, M.J.John[8)], S.Jolly, D.R.Price, P.Savage, B.Simmons, L.Toudup, D.Websdale
(1) also at CERN

University of Oxford, Oxford, U.K
M.Adinolfi, G.Damerell, J.H.Bibby, M.J.Charles, N.Harnew, F.Harris, I.A.McArthur, J.Rademacker, N.J.Smale, S.Topp-Jorgensen, G.Wilkinson

CERN, Geneva, Switzerland
G.Anelli, F.Anghinolfi, F.Bal, M.Benayoun(1), R.Beneyton, W.Bonivento(2), A.Braem, J.Buytaert, M.Campbell, A.Cass, M.Cattaneo, P.Charpentier, E.Chesi, J.Christiansen, R.Chytracek[9)], J.Closier, P.Collins, G.Corti, C.D'Ambrosio, H.Dijkstra, J.P.Dufey, M.Ferro-Luzzi, F.Fiedler, W.Flegel, F.Formenti, R.Forty, M.Frank, C.Frei, I.Garcia Alfonso, C.Gaspar, P.Gavillet, G.Gracia Abril[10)], A. Guirao Elias, T.Gys, F.Hahn, S.Haider, J.Harvey, B.Hay[11)], E.van Herwijnen, H.J.Hilke, G.von Holtey, D.Hutchroft, R.Jacobsson, P.Jarron, C.Joram, B.Jost, D.Lacarrère, M.Laub[12)], M.Letheren, J.F.Libby, C.Lippmann, R.Lindner, M.Losasso, P.Mato Vila, H.Müller, N.Neufeld, J.Ocariz[13)], K.Osterberg, C.Padilla, U.Parzefall, S.Ponce, F.Ranjard, W.Riegler, F.Rohner, S.Roiser, T.Ruf, S.Schmeling, B.Schmidt, T.Schneider, A.Schopper, W.Snoeys, W.Tejessy, F.Teubert, J.Toledo Alarcon, O.Ullaland, A.Valassi, P.Vazquez Regueiro, P.Wertelaers, A.Wright[14)], K.Wyllie
(1) on leave from Université de Paris VI et VII (LPNHE), Paris
(2) on leave from INFN Cagliari, Cagliari

[1)] now at Groupe d'Astroparticules de Montpellier (GAM), Montpellier, France
[2)] now at Thales Microelectonics, Grenoble, France
[3)] now at Dialog Semiconductor, Kirchheim-Nabern, Germany
[4)] now at Oslo University, Oslo, Norway
[5)] now at Pennsylvania University, Philadelphia, USA
[6)] now at LBNL, Berkeley, USA
[7)] now at Fermilab, Chicago, USA
[8)] now at Collège de France, Paris, France
[9)] now at IT Division, CERN, Geneva, Switzerland
[10)] now at ENWARE, Madrid, Spain
[11)] now at SWX Swiss Exchange, Geneva, Switzerland
[12)] now at Technical University of Prague, Prague, Czech Republic
[13)] now at Université de Paris VI et VII (LPNHE), Paris, France
[14)] now at Lancaster University, Lancaster, UK

Acknowledgements

The Outer Tracker Group and the LHCb collaboration are greatly indebted to all the technical and administrative staff for their important contributions to the design, testing and prototype activities. We are grateful for their dedicated work and are aware that the successful construction and commissioning of the LHCb tracking spectrometer will also in future depend on their skills and commitment. The help provided by the LHC Gas Group in the design of the drift gas system is greatly appreciated. We thank K. Huyser for his support in the document preparation. The cover illustration was designed by R. Arink.

Contents

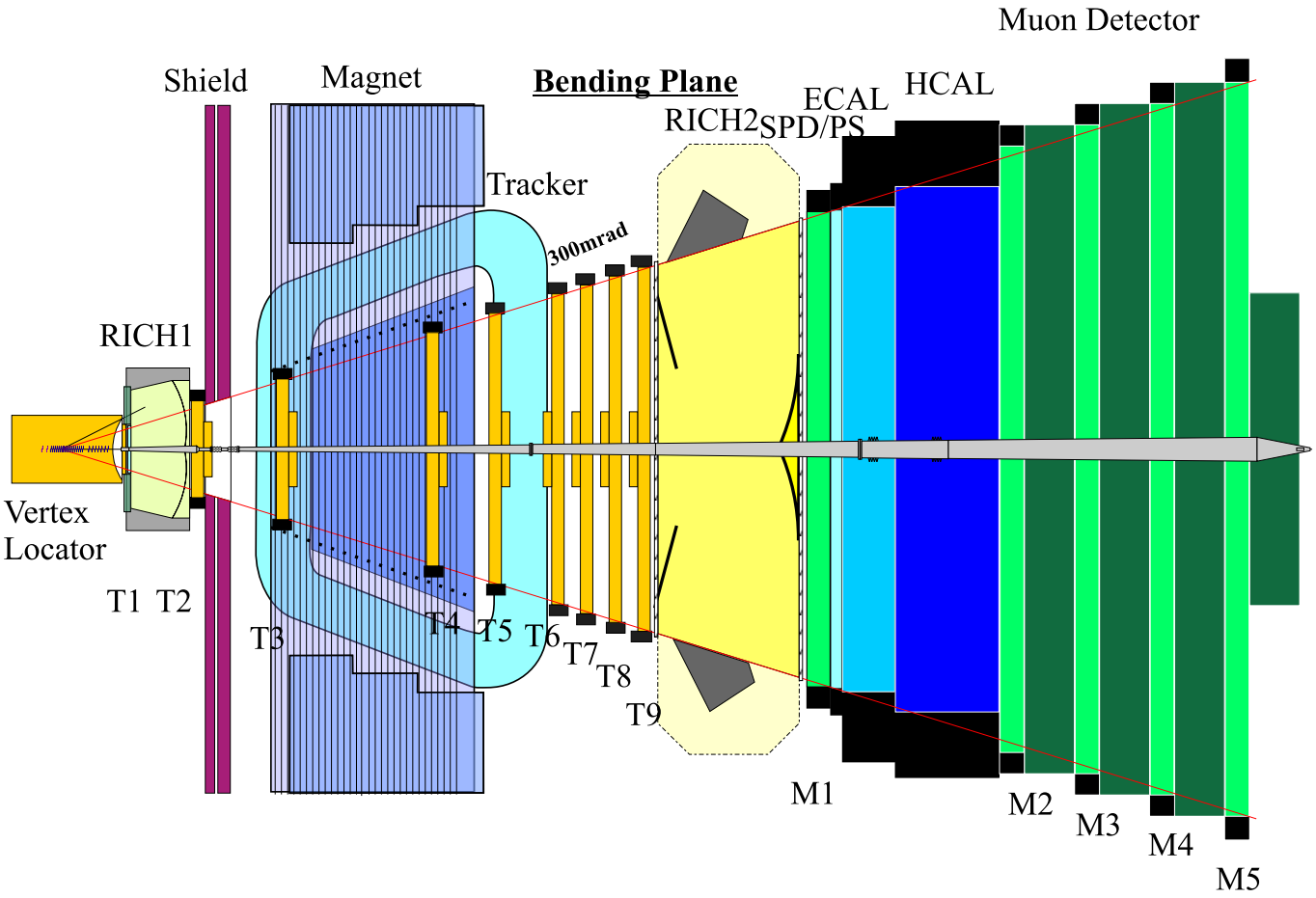

Figure 1: The LHCb spectrometer seen from above, showing the positions of the tracking stations T1 to T9.

1 Introduction

Since production of $b\bar{b}$ pairs at LHC will be strongly peaked at small angles to the beams, the layout of the LHCb detector resembles that of a fixed target experiment. The acceptance extends to 300 mrad in the bending plane (horizontal) and 250 mrad in the non-bending plane (vertical), with an insensitive region of approximately 15 mrad x 15 mrad around the beam pipe. Charge particle tracking behind the vertex region will be performed with a system of nine tracking stations, labelled T1 – T9 in figure 1. The innermost region of each station, where particle flux is highest, will be covered with a fine grained detector known as the Inner Tracker. The coarser grained Outer Tracker will cover the remaining area, which amounts to 98 % of the summed station surfaces. The small station T1, just behind the Vertex Locator, will be built with Inner Tracker technology only. In the other stations, the boundary between Inner and Outer Tracker has been chosen on the basis of studies of track reconstruction efficiency versus cell occupancy: with some safety margin, the Outer Tracker coverage was extended as far as possible towards the beam pipe. Figure 1.1 presents a general view of the set of Outer Tracker stations. Each station consists of several planes, and each plane is assembled from discrete detector modules.

1.1 Performance requirements

The main tracking system, consisting of a series of stations with Inner Tracker and Outer Tracker components, must perform the following tasks:

1. Find charged particle tracks in the region between the vertex detector and the calorimeters and measure the particle momenta. The momentum precision is an important ingredient in the mass resolution of the reconstructed B mesons. For example, a mass resolution of 10 MeV/c^2 in the decay $B_s \rightarrow D_s K$ translates into a requirement on momentum resolution of $\delta p/p = 0.4$ %. A high track reconstruction efficiency is especially important for B decays of relatively high multiplicity. Again taking the decay $B_s \rightarrow D_s(KK\pi)K$ as example, an 80 % reconstruction efficiency of decays that are fully contained in the LHCb acceptance requires a tracking efficiency per final state particle of 95 %.

2. Provide precise measurements of the direction of track segments in the two RICH detectors. This information is used as an input for the particle identification algorithms. In order not to limit the RICH performance, the track angular resolution must at least be 1 mrad at RICH 1 and 0.3 mrad at RICH 2 [1].

3. Link measurements in the vertex detector with the calorimeters and the muon detector.

The layout of the tracking system is optimised for upstream tracking, where one searches for track segments in stations furthest away from the interaction point and traces particle trajectories backwards through the magnet towards the vertex region. Besides the full procedure of track searching and track following for offline analysis, sufficiently fast algorithms must be available to supply momentum information to the level-2 trigger. One method directly links downstream track segments to track segments in the Vertex Locator by use of straight line extrapolations that intersect in the magnet region, without explicit track following through the magnet. Momentum is derived from the size of the 'kink' between the two straight lines. In a different approach one only uses informa-

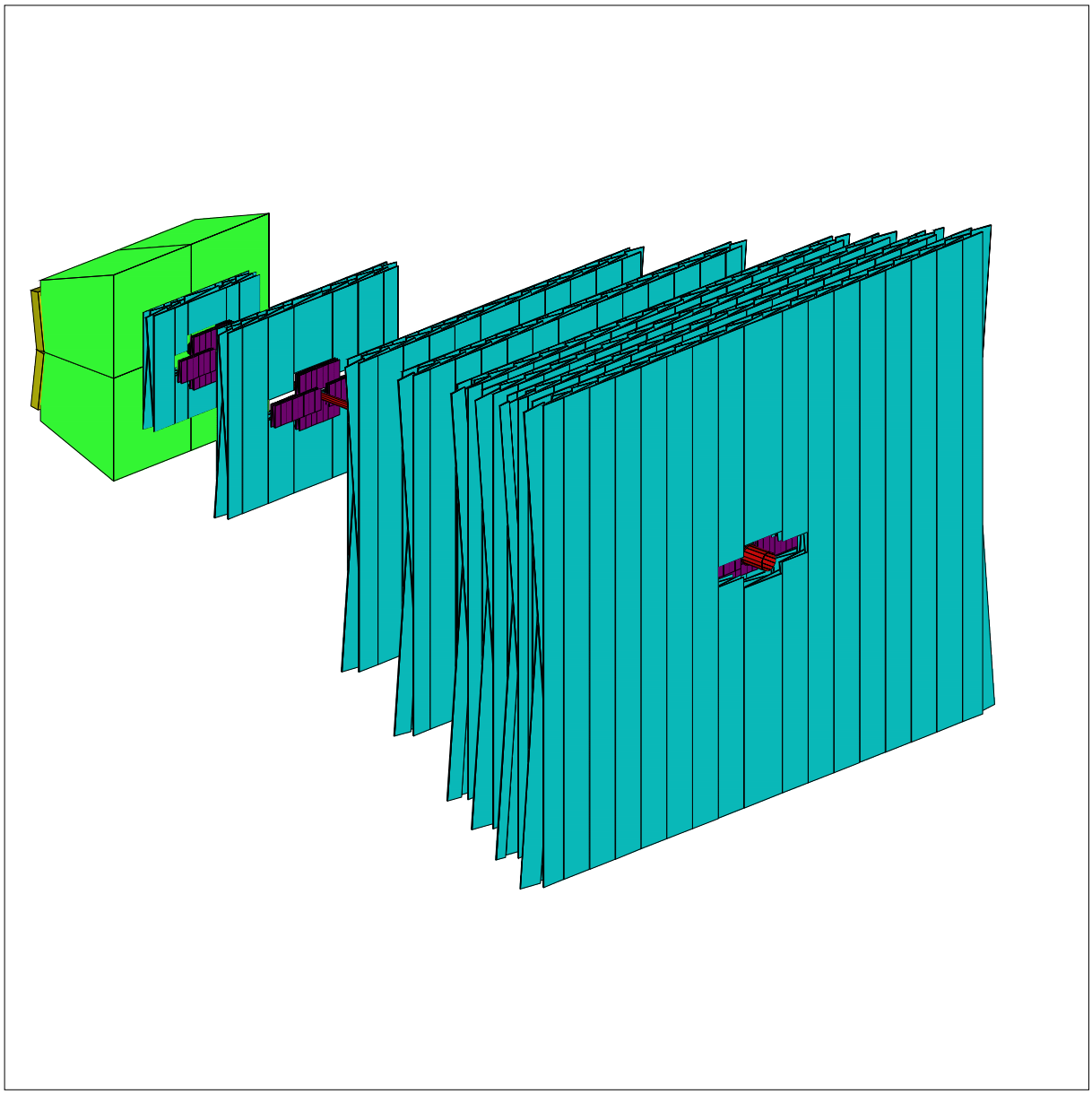

Figure 1.1: View of the set of Outer Tracker stations.

tion from the first tracking stations: track segments found in the Vertex Locator are followed over some length into the magnet region to obtain a momentum estimate.

1.2 Evolution since the Technical Proposal

In the Technical Proposal [2], the detection elements of the Outer Tracker were described as 'drift cells with straw tube geometry', foreseen to be constructed in the manner of a honeycomb chamber, i.e. from pre-formed sheets of conductive foil material. The honeycomb technique has been abandoned. The drift cells will instead be true straw tubes. The reason is that the selected cell material — a carbon doped polyimide — is well suited for winding but not for folding. The material selection is discussed in section 3.1. Wiring of straw tubes of several metres length is more difficult than would be the case for honeycomb chambers. On the other hand, our experience in building prototypes of both straw tube and honeycomb chambers indicates that the choice for straw tubes makes it easier to guarantee good precision on cell size, shape and pitch. Also, the drift time spectrum is better behaved in tubes of circular cross section than in hexagonal cells, where regions of low drift field near the cell corners lead to tails in the time spectrum.

At the time of the Technical Proposal cell sizes of 5 and 8 mm were anticipated. The 8 mm cells were foreseen in regions of low occupancy in stations behind the magnet. A limit of 50 ns — two bunch crossing intervals — has been imposed on the drift time window in order to keep pattern recognition manageable. It was already clear that the maximum drift time would inside the magnetic field exceed the limit of 50 ns if 8 mm wide cells were used. Systematic measurements on fast drift gas mixtures have shown that 8 mm cells are too large in any of the stations for gas mixtures of acceptable composition (no excessively large CF_4 content); after addition of the signal propagation time from avalanche position to the preamplifier, the maximum time delay is above or around the 50 ns limit, and does in any case not leave a safety margin. It was decided to use 5 mm diameter tubes only, rather than building two types of detector modules with only slightly different tube diameters.

As a consequence of the choice for straw tubes, the cell pitch could be reduced. It is inherent in the honeycomb technique that neighbour cells within the same layer can not touch. In our prototypes the bridge between two cells was 1 mm wide, i.e. cells of 5 mm diameter were placed at a pitch of 6 mm. (The fraction 5/6 of active over total area of a single layer was still high compared to a true honeycomb geometry, as used in the HERA-B Outer Tracker, where it is only 2/3.) Straw tubes can in principle be mounted directly next to each other. For reasons of assembly procedure and tolerances, the straw tubes of 5.0 mm inner diameter and 75 μm wall thickness will be mounted at a pitch of 5.25 mm.

The elimination of 8 mm cells and the pitch reduction of the 5 mm cells have increased the channel density, but at the same time the total surface area of the Outer Tracker has been reduced. Table 2.1 lists the set of Outer Tracker stations. Two stations have been eliminated since the Technical Proposal: one near the centre of the magnet and one behind RICH 2. Tracks will be followed through the magnet with three instead of four stations, at positions where the magnetic field starts to rise (T3) and fall (T4 and T5). Simulations have shown that the presence of a fourth station near the magnetic field maximum has no significant effect on track reconstruction efficiency and ghost rates, whereas its elimination has the obvious advantage of reducing the material budget. It had been anticipated that a tracking station between RICH 2 and station M1 of the muon de-

tector would be needed for the measurement of track slopes in RICH 2 and for track following towards the calorimeters and the muon chambers. It has since been shown that such a station is not needed for proper linkage of track measurements with the muon and calorimeter pad information. More recently — after submission of the RICH TDR — studies by the RICH group [3] have led to the conclusion that the quality of particle identification in RICH 2 does not suffer if that station is left out, given that the liberated space can be used to extend the radiator depth of RICH 2 by 33 cm. The 18 % gain in photon yield compensates for the reduced precision on track directions inside the radiator, which must now be determined by extrapolation from stations T6 – T9 rather than interpolation between T6 – T9 and a station behind RICH 2.

Furthermore, it has been shown [3] that planes of horizontally mounted straw tubes for precise measurement of the vertical component of track directions in the RICH detectors are not necessary. Such planes, additional to the set of planes optimised for track following and momentum measurement, had originally been foreseen in the stations just before and after RICH 1 and RICH 2. Track slopes in the RICH detectors can be determined with sufficient precision if these stations are fitted with the standard set of planes only: vertical wires and wires running under $\pm 5^o$ with respect to the vertical.

Detector planes with (almost) horizontally oriented drift tubes would have posed severe occupancy problems, since the vertical magnetic field tends to spread particles from near the beam pipe into the equatorial plane of the experiment. For this same reason, the boundary between Inner and Outer Tracker has been readjusted. In the Technical Proposal, the Inner Tracker was assumed to cover a rectangle of 60 cm horizontally by 40 cm vertically. It has been changed to the geometry sketched in figure 2.2. Inner Tracker lobes of 20 cm height extend to 60 cm from the beam pipe in the equatorial plane. At the same time the central rectangle has been reduced in width. These boundary adjustments have increased the channel count of the Inner Tracker, but they do not reduce the number of channels in the Outer Tracker, where the sole effect is that some straw tube modules become slightly shorter.

Relatively small changes in channel count have resulted from station displacements along the beam direction with respect to the positions assumed in the Technical Proposal. Shifts in station positions were necessary to adjust to the new magnet design, for re-optimisation of the station distribution after removal of one of the magnet stations, to accommodate a 7 cm upstream shift of the entrance wall of the RICH 2 vessel, and to allow for mounting of the Inner Tracker on Outer Tracker station frames. Within limits set by hardware restrictions, station positions were fine-tuned towards optimal track reconstruction efficiency and momentum resolution. The final positions are listed in table 2.1.

The number of channels within the LHCb acceptance is 101 k. In table 8.2 of the Technical Proposal it had been estimated at 110 k. The actually installed number of detector channels will be somewhat larger than 101 k. Where possible, straw tube modules of standard width will be allowed to extend outside the acceptance, instead of building special modules of smaller width. There will be a similar overshoot in the readout electronics: components will be built to handle channels in multiples of 32 per drift cell layer only.

Ongoing optimisation studies of the LHCb spectrometer may lead to a further reduction of the number of tracking stations. This would have no effect on the design of detector modules and of the readout electronics, but would of course reduce the number of detector channels to below the number given in table 2.1.

2 Detector specifications

2.1 Station arrangement

Momentum measurement essentially consists of determining the p_t kick between track segments on either side of the magnet. In other words, momentum resolution depends on track parameter precision in the low-field regions of the spectrometer. Stations inside the magnet are needed for track following – proper linkage of segments before and after the magnet – but do not contribute significantly to momentum resolution. Their number should not be larger than necessary for efficient track following, otherwise they may even diminish the spectrometer performance due to multiple scattering and energy loss in their material.

The LHCb tracking system has been primarily designed for upstream tracking: track segments found in the stations behind the magnet are followed backwards through the magnet towards the vertex region. Table 2.1 lists the position, lateral dimensions, arrangement of detection planes and channel count of each Outer Tracker station. Figure 2.1 shows the station positions within a plot of the variation of magnetic field strength along the length of the LHCb spectrometer. The z positions of the stations have been chosen on the basis of optimisation studies of track reconstruction efficiency and momentum resolution. The optimisation is not sensitive to station shifts of the order of 10 cm. On that scale, hardware considerations were taken into account. Emphasis is heavily on measurement precision in the x-z bending plane: drift cells have their wires running vertically (X planes) and under $\pm 5^o$ from the vertical (U and V planes). Spacing between successive planes of a station is such that the heart lines of the outermost planes are 17 cm apart. This lever arm allows an initial determination on station level of the slope of track segments in the bending direction with a precision of the order of 1 mrad. The X planes, which purely measure track coordinates in the bending direction, are placed at the extremities of the station lever arm to maximise the power of a fast first pass of track finding in x-z projection only.

Stations T6 – T9 span a lever arm of 1.6 m and experience only a relatively small stray magnetic field[2]. They provide 'track seeds', almost straight track segments that point towards the magnet region with good angular resolution. Stations T5 and T4 follow tracks upstream as they bend into the magnet gap. Their positioning is such that the number of possible track continuations to be considered is on average the same in T5 and in T4. At station T5 the magnetic field is at half its maximum value. T4 is still one metre away from the region of highest field, where occupancy due to curling low-momentum tracks would be highest. Station T3, placed where the magnetic field has from the side of the interaction point risen to half its maximum value, fulfils the same function for the case of downstream tracking. (Downstream tracking will be more difficult than upstream tracking. Because of the rather abrupt rise of the field when entering the magnet gap from the vertex side, search windows for track following have to be quite large. Nevertheless, it is the only way to determine momenta of particles swept out of the acceptance by the magnetic field.) Station T2 plays a crucial role in the momentum measurement: the T2 data have a large weight in determining the track segment on the vertex side of the magnet.

Station T2 also serves for measuring, together with T1, track slopes in RICH 1. Given that the track angular resolution will be around 0.4 mrad, it is not a limiting factor on the per-

[2] Of the 4.2 Tm field integral over the length of the LHCb detector, 0.3 Tm are covered by T6 –T9.

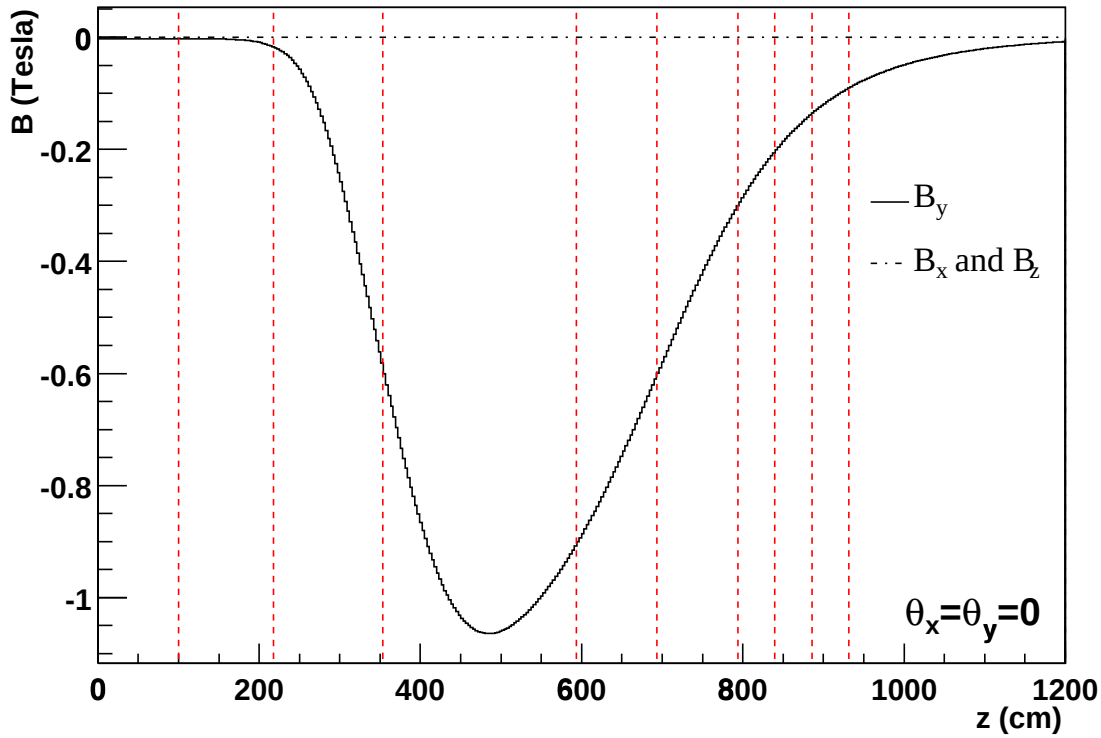

Figure 2.1: Magnetic field strength close to the beam pipe. The vertical lines show the positions of tracker stations T1 to T9.

station	z_{max} (mm)	active area x_{max} (mm)	active area y_{max} (mm)	planes (drift direction)	channel count active	channel count electronics
2	2275	704	581	X U V X	4.3 k	4.6 k
3	3635	1125	929	X U V X	6.8 k	7.2 k
4	6035	1867	1541	X U V X	11.4 k	11.8 k
5	7035	2176	1796	X U V X	13.1 k	13.3 k
6	8038	2486	2052	X U V X	15.1 k	15.4 k
7	8497	2628	2170	X U V X	16.0 k	16.4 k
8	8956	2770	2287	X U V X	16.8 k	16.9 k
9	9415	2912	2404	X U V X	17.5 k	17.9 k
					101.0 k	103.5 k

Table 2.1: Positions, active areas, detection planes and channel counts of the Outer Tracker stations. The exit face of a station is at position z_{max}. The outer acceptance boundary is 300 mrad in x and 250 mrad in y. Wires in U and V stereo planes run under $\pm 5^o$ from the vertical. The number of electronics channels exceeds the number of channels in the detector acceptance because of 32-fold readout modularity per detection layer.

formance of RICH 1. The station T1 (which has no Outer Tracker component) is placed directly behind the vertex tank and links the tracking system with the vertex detector. Track slopes in RICH 2 are obtained by extrapolation of track segments measured in T6 – T9. Since the function of RICH 2 is to perform particle identification at high momenta, multiple scattering in the material of the entrance wall of the RICH vessel does not strongly affect the angular resolution for tracks of interest. It is for this reason that a tracking station behind RICH 2 is not needed. Still, the performance of RICH 2 is more sensitive to tracking precision than is the case for RICH 1, because the resolution on Cherenkov angle per photon is higher (0.58 mrad in RICH 2, 1.45 mrad in RICH 1).

The shape of the inner boundary of the Outer Tracker acceptance is shown in figure 2.2. Its size was determined by the requirement that occupancies at the nominal LHCb luminosity of $2x10^{32}cm^{-2}s^{-1}$ should not exceed 10 % in the track seeding stations T6 – T9 and 15 % in the track following stations T2 – T5, in order to obtain good track reconstruction efficiency and low ghost rates (see chapter 4). The vertical extension of the central hole as given in the figure is indicative only. In stations T5 to T9 it in fact increases from 38.2 cm to 42.2 cm to allow mounting of Inner Tracker modules of standard size around the conical beam pipe. In T2 – T4 it increases from 50.5 cm to 58.1 cm. In T2 the wings extend over 17 cm rather than 34 cm. The horizontal dimensions of 17 cm, 34 cm and 51 cm = 34 cm + 17 cm correspond to widths of standard Outer Tracker modules. The active area of the Inner Tracker extends 1 cm into the Outer Tracker acceptance.

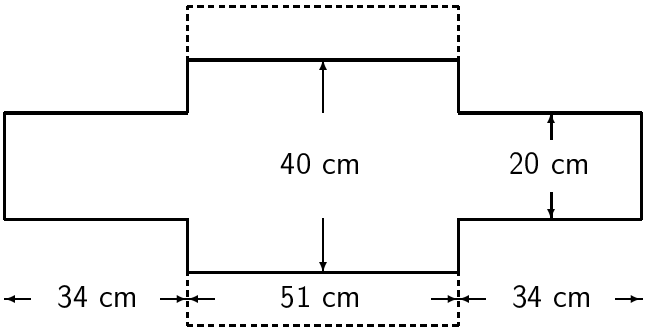

Figure 2.2: Inner boundary of the Outer Tracker acceptance. In stations T2 – T4 the vertical extension of the central hole is larger (dashed lines).

2.2 Straw tube modules

Each station plane is assembled from discrete modules, see figure 1.1 and detailed figures in section 5.2. A module contains two staggered layers of straw tubes, which makes a total of 8 detection layers per station. The modules are designed as stand-alone detector units, providing their own mechanical rigidity and gas hermeticity. They define the modularity of the readout electronics and of the drift gas and high voltage distributions. The standard module width is 64 tubes per layer. All tubes have an inner diameter of 5.0 mm and a wall thickness of 75 μm. The tube pitch within a layer is 5.25 mm. The wire planes of the two tube layers within a module are 5.5 mm apart. The full width of a module, including 0.5 mm strips that serve as the lateral walls of the module box, is 340 mm. The straw tubes are mounted on sandwich panels. The panels serve at the same time as the main elements of the module box (see figure 5.1 for a drawing of the module cross section). Modules within the same detection plane do not overlap. At the boundary between adjacent modules, the inactive area per layer corresponds to exactly one tube width. Simulations show this loss to be entirely acceptable, given that there are 8 layers per station. Modules are mounted on a frame structure. The left and right halves of the station frame can independently be moved towards or retracted from

the beam pipe. Mounting pins define the module positions with respect to alignment targets on the frame. An optical alignment system will monitor relative movements of the stations.

The choice of an $Ar/CF_4/CO_2$ mixture as drift gas was determined by the fact that fast drift is crucial, while there is no need for the ultimate in drift coordinate resolution. For good track reconstruction efficiency and low ghost rates, the time overlap between drift signals from different bunch crossings must be minimised. With the proper amount of CF_4 admixture, the sum of drift time and signal transmission time from avalanche to preamplifier can be kept below 50 ns (two LHC bunch intervals) in all straw tubes in all stations. The presence of a CF_4 component in the drift gas limits the choice of construction material for the straw tubes. Decomposition of CF_4 molecules in the avalanche process contaminates the gas with fluorine radicals, which may react with exposed surfaces. It is for this reason that the inner wall of the straw tubes will consist of a carbon doped polymer foil rather than a metallic layer.

Electron capture by CF_4 molecules limits the drift coordinate resolution, but at the foreseen mixing ratio $Ar(75)CF_4(15)CO_2(10)$ it will not be worse than 200 μm. In chapter 4 it is shown that such a single-cell position resolution does not dominate the uncertainty on momentum measurement. Up to 100 GeV/c its contribution to the momentum error is smaller than that from multiple scattering in the detector material. The single cell efficiency for isolated tracks is almost 100 %, except for the last 250 μm near the straw tube wall. The two staggered straw tube layers within a module together provide fully efficient coverage[3].

[3]Except for some pathological angles of incidence that are not possible for tracks from the vertex region and that may only occur for particles from secondary interactions in detector or beam pipe material.

2.3 Readout electronics

A preamplifier-shaper-discriminator with short input peaking time and low noise level is required for accurate timing of the leading edges of straw tube signals. The ASDBLR chip [4, 5] developed for the ATLAS Transition Radiation Tracker and its offspring, the ASDQ chip [6] developed for the CDF Central Outer Tracker, excellently match the requirements. They both feature active baseline restoration circuitry to suppress the slow ion-tail signals. At the foreseen gas amplification and discriminator threshold settings, the mean dead time per hit (i.e. the double pulse resolution) is in the range of 30 – 40 ns. While this is in itself a good result, the fast drift makes it almost equal to the drift time window, which means that the straw tubes have essentially no double hit capacity within the same event.

The readout window of drift signals will be limited to 50 ns. The electronics nevertheless does allow for raising the window to 75 ns. Timing information will be encoded in $(25/2^5)$ ns $=$ 0.78 ns bins by adding 5 bits of fine time to the LHC bunch clock. A dedicated TDC chip for the LHCb Outer Tracker is under development at the ASIC laboratory in Heidelberg. The 32-channel OTIS (Outer Tracker Time Information System) chip [7] will be produced in radiation hard 0.25 μm deep submicron CMOS process. It can thus be incorporated in the on-detector electronics, which keeps the amount of cabling limited. The development schedule foresees full prototypes to become available in 2002.

Since the OTIS chip is still in a rather early stage of development, it is prudent to have a fall-back solution based on an already existing TDC. For this purpose a readout scheme based on the HPTDC chip [8] has been developed. A full prototype of that chain is presently being tested. The HPTDC has a data-driven architecture. The LHCb electronics specifications [9] assume a synchronous clock driven layout.

As a consequence, hit and trigger losses can not be fully excluded when using the HPTDC. Since this chip is not radiation hard, it can not be mounted directly on the detector. The time path for OTIS development (and for a possible decision to activate the fall-back solution) are discussed in sections 5.3 and 6.2.

Upon event acceptance by the L0 trigger, zero-suppressed TDC data are transported over optical links to the L1 buffers and logic located in the counting room. After receipt of a L1 accept signal the data is delivered to nearby Readout Units. It is presently not foreseen that data from the Outer Tracker will themselves contribute to the L0 and L1 triggers. Momentum information from a fast tracking algorithm will be used in the L2 trigger decision.

3 Prototype results and other design ingredients

There have been two main lines of development work: response optimisation of straw tube drift cells and selection of cathode material. Results on the behaviour of straw tubes, as a function of the mechanical and electrical layout of detector modules and of the drift gas mixture, are presented in section 3.3. Considerations and test results regarding the choice of cathode material are presented in section 3.1. On this subject we have profited from earlier work by ATLAS, HERA-B and COMPASS. The material choice concerns long-term behaviour ('aging effects') but does not otherwise affect the drift cell properties. Therefore, the two R & D lines of response optimisation and material selection could be pursued in parallel. The two lines have joined in the ongoing activity of testing entire detector modules of almost final design in a realistic irradiation environment (test of 'global aging'). Conditions in HERA-B closely resemble those in LHCb, both in incident rate and in particle composition. The HERA-B collaboration has allowed us to install prototype modules at a high rate location in their spectrometer. First results are reported in section 3.4. Tests on global aging will continue, in HERA-B, with a 20 MeV proton beam in Heidelberg and with an X-ray source.

3.1 Selection of cathode material

The drift gas must contain a CF_4 component in order to collect all drift signals within a time window of 50 ns (two LHC bunch crossing intervals). At electron energies of a few eV, which occur at the onset of the avalanche region, the cross section for electron capture by CF_4 is large, of the order of $10^{-18} cm^2$ [10]. This has two consequences. First, there is an appreciable drift signal attenuation, which contributes to the error on the drift coordinate measurement (the nearest primary ionisation cluster may go undetected) and which in principle leads to some loss of efficiency. In section 3.3 it will be shown that drift signal attenuation does not significantly affect the performance of our detector.

A potentially more dangerous result of electron capture by CF_4 molecules is the creation of free fluorine radicals by CF_4 dissociation. These may attack construction materials of the detector, possibly after first reacting with trace impurities in the drift gas. A gold-tungsten anode wire without pores or cracks in the gold layer is not in danger. Addition of a few percent of CF_4 to the drift gas is in fact sometimes used as a remedy against anode wire aging: it cleans the wire surface of polymer deposits from the avalanche. However, the use of an exposed cathode surface of aluminium or copper should be avoided when the drift gas contains an appreciable fraction of perfluorocarbons. Detectors using such a mixture — ATLAS Transition Radiation Tracker, HERA-B Outer Tracker and Transition Radiation Detector, COMPASS Straw Tube Tracker — have instead opted for a carbon-loaded polymer as cathode material, which offers the additional advantage of having a large radiation length. For instance, ATLAS compared straw tubes with an exposed aluminium surface and tubes made of a multi-layered material with 4 μm of carbon-doped polyimide as surface layer, with a $Xe(70)CF_4(20)CO_2(10)$ gas filling. The former started to deteriorate at 0.2 C/cm charge dose, whereas the latter were still unharmed at several C/cm [11]. By irradiation with a radioactive source, HERA-B compared honeycomb drift cells of carbon-doped polycarbonate foil (trademark Pokalon) and cells where the same foil material had been covered with a copper layer. The copper layer was visibly degraded after a charge dose of 2 C/cm, while

the naked Pokalon was still unharmed after a dose of 4 C/cm [12].

The highest charge dose to be expected in the LHCb Outer Tracker can be estimated as follows. The boundary with the Inner Tracker has been set in such a way that the hottest cells of the Outer Tracker will have a mean occupancy per event of ∼15 %. The averaging includes 'pile-up events' with more than one inelastic p-p interaction in the same bunch crossing. Possible time overlap between drift signals from events belonging to different bunch crossings has also been taken into account, see chapter 4. Assuming an inelastic p-p cross section of 80 mb, the average data taking luminosity of 2×10^{32} cm^{-2} s^{-1} leads to rates of 9.3 MHz and 3.0 MHz for bunch crossings with one and more than one inelastic interaction, respectively. At the maximum cell occupancy of 15 %, the inelastic event rate of 12.3 MHz translates into a particle rate of almost 2 MHz integrated over the cell length. The rate variation along the length of a cell will depend on the position of the cell. (In first approximation, in cells above and below the Inner Tracker the track density scales as $1/r^2$, where r is the distance to the beam line. In cells to the left and right of the Inner Tracker, an equatorial plane population is superimposed on the $1/r^2$ distribution). At 2 MHz integrated rate, the highest local rate per cm of cell length is approximately 250 kHz. With $Ar(75)CF_4(15)CO_2(10)$ as drift gas, a minimum ionising particle creates on average 30 – 35 ionisation electrons per drift cell. Because of electron capture by CF_4 before avalanche development, the charge collected per particle is less than the product of gas gain and number of ionisation electrons. One may include the effect of attachment as an apparent reduction of gas gain. The effective gain was measured with a ^{55}Fe source and a charge integrating amplifier [4] At the foreseen working point of 1550 V, it is 2×10^4. So the collected charge per particle is $7 \times 10^5 \times e \simeq$ 100 fC. At 250 kHz incident rate per cm wire length, this leads to an integrated charge dose of 2.5 C/cm after 10 run years of 10^7 s.

We have experimented with carbon-loaded polycarbonate (Pokalon) and polyimide (Kapton) films, and to some extent with the multilayered product used in the ATLAS Transition Radiation Tracker. The Pokalon material can be folded into a permanent shape at room temperature. It has been chosen by HERA-B for its Outer Tracker honeycomb chambers. The carbon doping is 30 % by volume. Our samples were from a batch used for the HERA-B series production. Kapton film with a volume doping of carbon is available from Du Pont under product designation Kapton XC in a wide range of values of resistance per square, dependent on the volume fraction of soot particles and on the film thickness. This material is not suited for the production of honeycomb chambers, because folding would require a temperature of at least 400 centigrades. One instead produces straw tubes: a ribbon of Kapton foil is wound on a mandril and covered with a second, staggered layer of windings. The second layer is not exposed to the drift volume and may be of the same or of a different material. That question will be addressed in section 3.2, here only the material choice for the exposed inner layer is discussed. For the inner layer we experimented with XC-160 foil (25 % carbon by volume, 40 μm thickness, resistance approximately 370 $\Omega/\Box$) and, less extensively, with XC-275 (69 μm, 230 $\Omega/\Box$). A tube of 5 mm diameter wound of two layers of XC-160 has a resistance of 12 kΩ/m. Given that the precise value of the cathode foil resistance was found to be unimportant for the straw tube performance, we have concentrated on XC-160, the lighter of the two.

The Kapton XC product has been chosen by COMPASS for its straw tube detectors. The

[4] The fast ASDBLR preamplifier that will be used in the actual set-up integrates only one quarter of the signal charge.

ATLAS and HERA-B transition radiation detectors use a multi-layered cathode foil, which we further refer to as 'TRD foil'. It consists of a Kapton substrate which on one side carries a conductive layer of 2000 Å aluminium under a surface cover of 4 μm of carbon-loaded Kapton, and on the other side a polyurethane layer. Tubes are wound from two layers of this material, bonded together at the polyurethane sides. At the time when this material was developed, Kapton XC was not yet on the market. Comparative tests of the multi-layered TRD foil and Kapton XC have been performed by COMPASS [13]. They prefer Kapton XC because of its mechanical robustness (no surface damage when wire supports are slid into the tubes, etc.) and the constant quality of the product. The firm[5] which has produced tubes from both materials has similarly commented favourably on the mechanical characteristics of Kapton XC. As to aging resistance, COMPASS considers both products to be adequate. The multilayered material has been tested extensively by ATLAS [11] on radiation hardness (γ-ray dose of 80 Mrad per straw, total neutron fluence of order 10^{15} per cm^2) and on aging related to the integrated avalanche charge dose (up to 18 C/cm). COMPASS performed local aging tests on Kapton XC tubes filled with $Ar/CF_4/CO_2$ in a low-energy proton beam up to 1.2 C /cm [14].

When our own material tests started, HERA-B had already observed apparent cathode aging of Pokalon-C chambers operated with an $Ar/CF_4/CH_4$ drift gas mixture under exposure to a hadron beam. The observed fluctuations of signal current and dark current, and persistence of current after beam turn-off (Malther effect), could be due to (local) loss of cathode surface conductivity. No such effects were seen after replacement of the quencher CH_4 by CO_2 and applying a gold coating to the cathode foil. We tested drift cells filled with the $Ar/CF_4/CH_4$ mixture in an 11 MeV proton beam at the Tandem Van de Graaff accelerator in Utrecht. HERA-B had observed that Pokalon-C chambers operated with this gas at an exchange rate of one volume per hour started to draw current already after a charge dose of 10 mC/cm when exposed to a 100 MeV beam of alpha particles. Our tests [15] were conducted on Pokalon-C and Kapton XC cells with a gas refresh rate of several volumes per hour, up to a charge dose of 130 mC /cm. No effects were seen: no shift in the relation between current and high voltage, no persistent current after beam switch-off, no other residual currents.

In more extreme circumstances, degradation of foil material exposed to $Ar/CF_4/CH_4$ *was* clearly observed. Foils of Pokalon-C and Kapton XC, as well as the multi-layered TRD foil, were over an area of several mm^2 exposed to a glow discharge in the gas mixtures $Ar(65)CF_4(30)CO_2(5)$ and $Ar(74)CF_4(20)CH_4(6)$, in a setup where their functioning as cathode of a proportional counter could immediately afterwards be tested [15]. Of course, a sustained glow discharge does not simulate realistic aging conditions. The purpose of these tests was to compare the robustness of the different foil materials and to compare the effects of the CH_4 and CO_2 admixtures. The TRD foil was very quickly damaged: the thin carbon loaded top layer was destroyed after 1 minute of glow discharge. Pokalon-C and Kapton XC foils exposed to about 2 C of charge dose under $Ar/CF_4/CO_2$ showed carbon deposits from decomposed gas molecules, but counter operation at unchanged working point remained possible. Under $Ar/CF_4/CH_4$ the situation was different: after the discharge treatment, the system started counting at lower high voltage and the current initiated by the presence of a source persisted after removal of the source. This apparent Malther effect is consistent with the fact that the damaged region of the foils had become poorly conducting. No aging effects were seen in irradiation tests with a

[5] Lamina Dielectrics Ltd, Billingshurst, England.

Sr^{90} source of straw tube and honeycomb cells filled with $Ar/CF_4/CO_2$ mixtures [15].

Kapton XC straw tubes were tested on radiation hardness — as opposed to effects due to avalanche charge collection — by keeping high voltage off during exposure, and checking afterwards for proper operation at the HV working point. The tubes were placed in a proton beam of sufficiently degraded energy to be just stopped in the tube material. The absorbed energy dose of 0.7 Mrad did not result in any observable effects on chamber operation. The highest local dose on the Outer Tracker is estimated [16] at 1 Mrad in ten years of LHCb operation.

Conclusion

Given that the drift gas mixture $Ar/CF_4/CH_4$ appears to carry risks of cathode surface degradation and anode wire aging due to the simultaneous presence of fluorine radicals and hydrogen, we have chosen for $Ar/CF_4/CO_2$ as drift gas. HERA-B and COMPASS earlier made the same choice. It is difficult to judge how hard the evidence is that Pokalon-C cells filled with the $Ar/CF_4/CO_2$ mixture might suffer aging effects in the LHCb environment. HERA-B has by far the largest experience with this material. They decided that the safe approach was to coat the Pokalon cathode surface with a gold layer. Very important is the fact that the manufacturer of carbon-doped Pokalon has discontinued commercial production. If we were to order the material, the production facility would have to be put in place again, at prohibitive cost.

Carbon-doped polyimide exposed to a drift gas containing CF_4 has been shown to be aging resistant, either in the form of a thin surface layer (multilayered foil, tested by ATLAS to 18 C/cm) or as a homogeneous film (Kapton XC, tested by COMPASS to 1.2 C/cm with our intended gas mixture). Kapton XC is mechanically much more robust, which is especially important for the procedure of inserting wire supports into the tubes. It also is a readily available industrial product, whereas the multilayered TRD foil is made by a research institute which is not a member of the LHCb collaboration.

Thus, we have selected Kapton XC film as the inner layer of the Outer Tracker straw tubes. The choice for Kapton material implies that the Outer Tracker should be made of straw tubes. Folding or moulding into honeycomb shape would be entirely impractical, since it would have to be done at temperatures in excess of 400 centigrades.

3.2 Electrical configuration

Outer Tracker operation under LHCb conditions will only be possible with fast front end electronics. The length of the straw tubes (up to 2 $\times$ 2.4 m) and the large bandwidth of the front end electronics make the readout system sensitive to various kinds of external pickup, cross talk and oscillations. Design optimisation from the point of view of signal transmission is therefore very important. The studies of electrical properties of long straw tubes of various types are described in detail in [18].

Wire termination

Signals will be read out at the wire ends near the top and bottom of a station. The anode wire resistance of 110 Ω/m causes significant signal attenuation and smearing: the attenuation length for high frequencies ($>$ 10 MHz) is $\sim$6 m. Since the straw tubes of the Outer Tracker are quite long (up to 2.4 m), the signal attenuation will be noticeable and can affect the coordinate resolution of the detector. The effect will be most pronounced for the regions furthest away from the preamplifiers, i.e. near the y=0 plane, where track density will be highest. In order to optimise chamber performance in that region, it was decided to leave

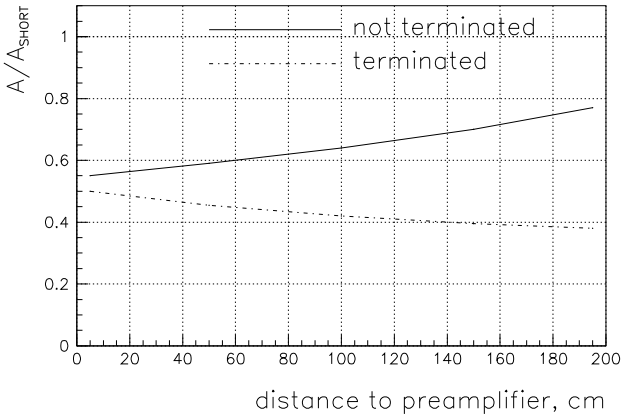

Figure 3.1: Signal attenuation in a long chamber.

the far end of wires electrically open. In this case both direct and reflected components of a signal from the far end will arrive at the preamplifier almost simultaneously, doubling the amplitude and thus compensating for signal attenuation. For signals occurring closer to the preamplifier, the arrival time difference will not exceed 20 ns even for the longest straw tubes of the detector. The superposition will lead just to some elongation of the signal and not to double discriminator firing.

Figure 3.1 shows the ratio of signal amplitude in a 2 m long straw tube to that in a short chamber (30 cm) under the same operating conditions, as a function of the distance to the preamplifier, for terminated and unterminated designs. The advantage of the unterminated design is clearly seen. It should be noted also that even in this case the amplitude in the long tube is significantly less than in the short one. Therefore, coordinate resolution must be expected to become gradually worse with increasing tube length. A second advantage of the unterminated option is that less material will be present in the hottest region of the detector.

In principle, the unterminated design requires good impedance matching at the preamplifier end, in order to suppress higher order reflections. In practice it is difficult to provide perfect matching at the preamplifier using RC networks. Not only is the input impedance of the ASDBLR (ASDQ) preamplifier frequency dependent [5, 6], but also the characteristic impedance of the straw tube varies with frequency within the signal bandwidth ($\sim 3 - 30$ MHz) due to the significant sense wire resistance. It was nevertheless found experimentally that good signal shape can be achieved by addition of a single series resistor of 150 Ω at the preamplifier input. The averaged shapes of ^{55}Fe signals from the far and near ends of a 3 metre long straw tube are shown in Fig.3.2. The signals show no significant higher order reflections; in addition to the suppression by approximate impedance matching at the preamplifier, they are also suppressed by attenuation when travelling along the tube.

Outer winding of straw tubes

The choice of material for the outer winding of the straw tubes is of importance for signal transport from avalanche to preamplifier. After the material of the inner winding was chosen to be carbon-loaded Kapton (Kapton XC) in order to minimise risks of cathode surface aging, we still considered three different possibilities for the outer winding: Kapton XC, i.e. the same material as the inner winding; pure Kapton; aluminium foil. Figure 3.3 shows a module layer with the the three types of tubes under assembly. Pure Kapton and aluminium foils are much cheaper than Kapton XC foil. Kapton XC and aluminium foils are conductive. In this case the cathode potential (ground) for the inner winding can be defined simply by contact to the outer winding. For an outer winding of pure Kapton one should instead develop more intricate end pieces, providing direct electrical contact to the inner Kapton XC winding. Aluminium foil has low resistance and can pro-

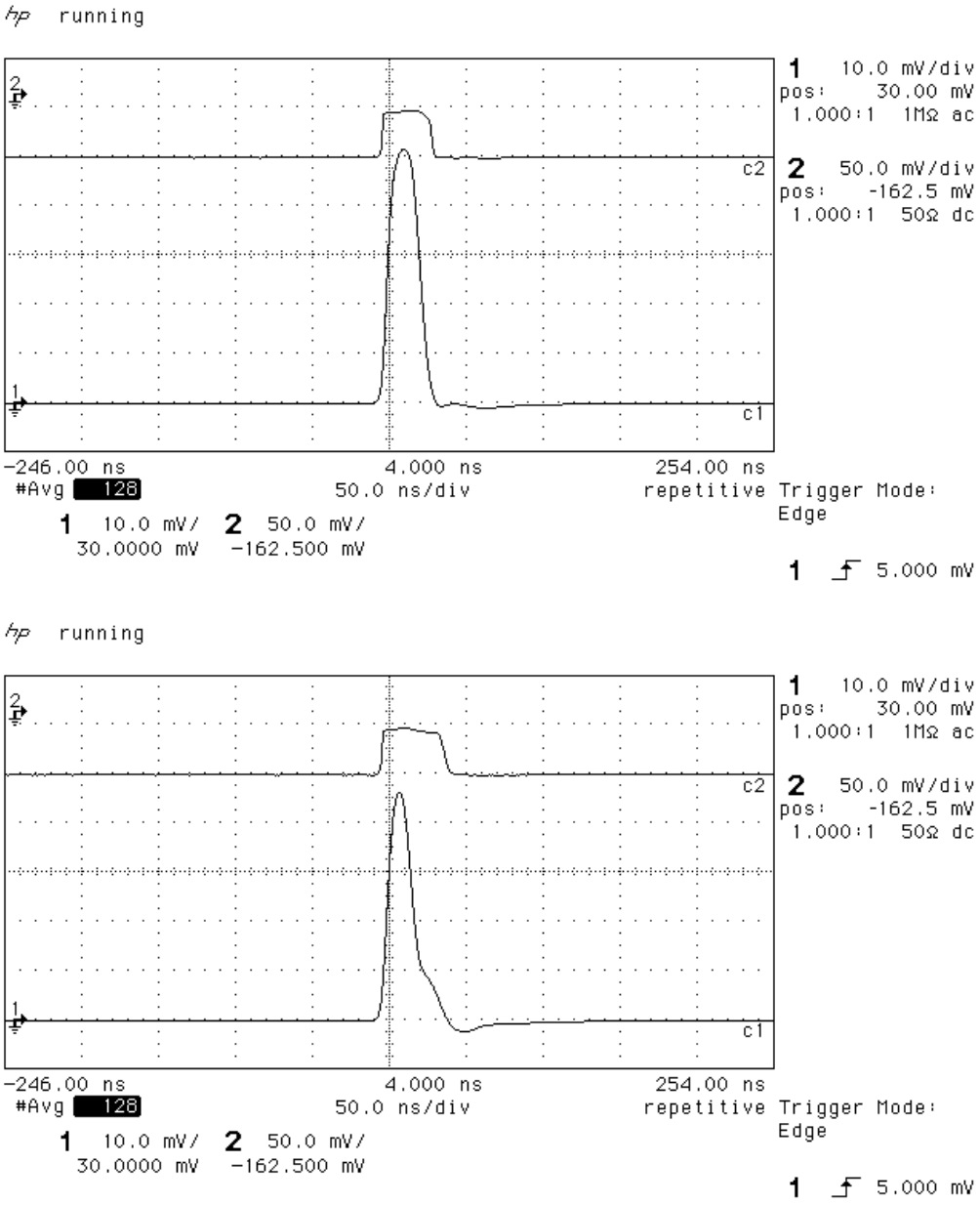

Figure 3.2: Shapes of ^{55}Fe signals from the far end (top) and near end (bottom) of a 3 metre long straw tube.

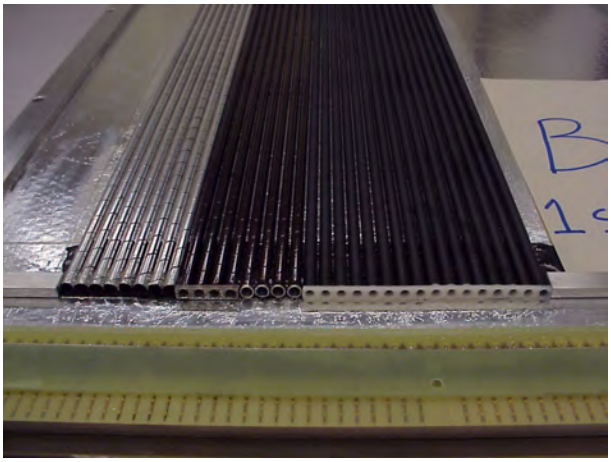

Figure 3.3: Layer of a test module with different foil materials as outer windings. From left to right: aluminium, pure Kapton, Kapton XC.

vide electrical shielding for each tube individually, which can reduce the cross talk level of the detector. On the other hand, an aluminium winding adds more to the material budget because of its lower radiation length (8.9 cm versus 28.6 cm for Kapton).

Beam tests of a prototype equipped with both double Kapton XC tubes and Kapton XC + aluminium tubes clearly showed [17] the expected reduction in cross talk between tubes with an aluminium winding. Their rate of digital cross talk was 1/6 of that between double Kapton XC tubes. (If a 25 μm aluminium shielding foil was placed between the two layers of tubes, the cross talk rate between double Kapton XC tubes reduced to about 3 times the rate of Kapton XC + aluminium tubes.) Since the observed rates include contributions from cross talk in front end electronics, the difference in intrinsic cross talk behaviour of the two types of tube is even more pronounced, as shown by the laboratory tests described below.

The definite choice for an aluminium outer winding was made after extensive laboratory studies [18] of the signal behaviour in double Kapton XC and Kapton XC+aluminium straw tubes, The 25 μm thickness of aluminium foil is a reasonable compromise between requirements of good electrical conductivity, minimal thickness of material and acceptable mechanical properties. The electrical resistance of 25 μm aluminium foil is $\sim 10^{-3}\Omega/\Box$, which provides good enough electrical screening. A 20-25 μm thick foil is optimal from the mechanical point of view: it is robust enough for handling and thin enough to produce no residual mechanical deformations. As outer winding of straw tubes, it increases the amount of material by $\sim 0.08\ \%X_0$ per detector module of two straw tube layers with respect to Kapton or Kapton XC. For proper detector operation, the ground foil of the sandwich panels on which the straw tubes are mounted must be reliably connected to the ground plane of the preamplifier board, otherwise the system becomes sensitive to external pick-up and inclined to oscillations.

The laboratory tests described in [18] were performed on a 1.6 m long prototype containing straw tubes with all three types of outer winding. The chamber was irradiated with a ^{55}Fe source and high voltage was supplied to only one of the tubes (active channel). The amplitude of signals was measured in the active channel and its neighbours. The analog cross talk level was defined as the ratio of these amplitudes. All possible effects of coupling between preamplifier channels were excluded, so the results represent intrinsic properties of the detector.

The analog cross talk for all types of straw tube showed a variation of $\sim$30 % along the tube length, reaching its maximum at the far end. The detailed comparison of properties of different straw types can be found in [18]. The most important result is that the analog cross talk level in Kapton XC+aluminium tubes was at least 3 times lower than in double Kapton XC or Kapton XC+Kapton tubes. Namely, at the far end of the chamber it was 1.8 %, 1.7% and 0.5% of the pulse height in the active channel, respectively, for

double Kapton XC, Kapton XC+Kapton and Kapton XC+aluminium tubes. This gives a sizeable difference in the fraction of parasitic signals crossing the discriminator threshold.

The expected rate of digital cross talk (average number of parasitic hits in the readout electronics per track) can be calculated from the analog cross talk using amplitude spectra of charged particles. Such spectra were measured in beam tests of straw tubes filled with the gas mixture $Ar(65)CF_4(30)CO_2(5)$ at reasonable working point (1750 V, effective gas gain $\sim 3 \times 10^4$). Assuming discriminator threshold settings of 2.2 fC visible charge (near the value used in beam tests), the calculations for this mixture give digital cross talk levels of 40% and 3% for double Kapton XC (or Kapton XC+Kapton) and Kapton XC+aluminium tubes, respectively.

The analog cross talk values characterise the electrical design of the chamber and do not depend on signal amplitude. In contrast, the digital cross talk level derives from the analog one via signal spectrum and discriminator threshold and therefore depends on the chamber operation parameters. This means that the above values of digital cross talk level can be considered only as indicative. However, the important conclusion about the advantage of the aluminium outer winding holds at any setting.

These studies revealed a nontrivial fact: at some grounding schemes, signals in a system of Kapton XC+aluminium straw tubes can show oscillatory behaviour, inducing significant parasitic signals to neighbouring channels. A layout was tested where 2 m long straw tubes were placed at 1 mm above the ground foil and where they had no contact to each other, except at the preamplifier end. In this case, the crosstalk between neighbouring channels was 5% by amplitude, which is even much worse than in the case of double Kapton XC tubes. The active and parasitic channels both showed oscillatory behaviour at a frequency of

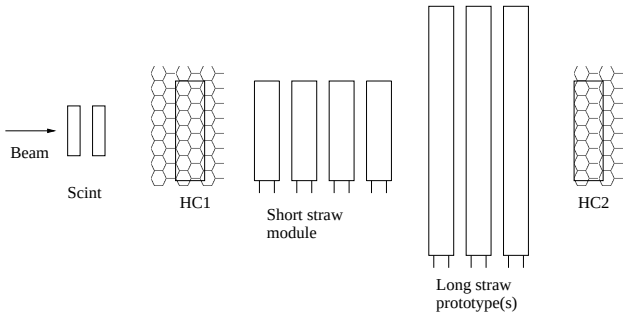

Figure 3.4: Principle of the testbeam setup.

about 37 MHz. The reason of this was understood and confirmed via PSpice simulation. The problem is that neighbouring straw tubes with aluminium outer windings form a transmission line with low attenuation. When the tubes are connected to ground only at the preamplifier end, each pair of neighbouring straw tubes acts as a quarter-wavelength resonator at $\sim$ 37 MHz. It was found that in order to damp such oscillations, the aluminium outer windings of tubes should have good (low-resistance) electrical contact to the ground plane and/or to each other, continuously over their length or at intervals not larger than about 20 cm. Such contact can be provided, for example, using conductive glue. The conclusion is therefore that the grounding design is very important for proper operation of the Kapton XC+aluminium straw tubes.

3.3 Beam tests of prototypes

Extensive beam tests of straw tube prototype modules were performed in 1998-2001 [17, 19, 20, 21, 22]. The drift cell behaviour as a function of drift gas mixture and magnetic field was investigated using a set of short chambers. The performance of long prototypes was studied to verify the principles of electrical and mechanical design. All prototypes employed straw tubes of 5.0 mm inner diameter, with a 25 μm diameter anode wire. The tests were performed with 10 GeV/c pions at the T7

beam of the PS accelerator at CERN. A typical testbeam setup is shown in Fig.3.4. It consists of a module with several layers of short straw tubes, long prototypes, two honeycomb chambers (HC1 and HC2) and trigger scintillation counters. Our setup did not have a high precision external tracker. Instead, the parameters of the chambers were determined using autocalibration procedures described in [19, 23]. The set of short straw tube layers was made up of four chambers, each with two staggered layers of 16 straw tubes. The straw tubes of double Kapton XC, 30 cm long, were directly mounted on sandwich panels clad with inner and outer ground foils. The wire spacing in a layer was 6 mm, the distance between the two wire planes of a chamber was 5.5 mm. The four chambers were mechanically mounted as a single module, 14 cm long along the beam direction, with all wires parallel to each other.

A variety of long prototypes has been tested. As an example, figure 3.5 shows a set of 1-metre modules being readied for test beam. The last series of tests used a 3.2 metre prototype with a layout that closely resembles the final design. The cross section in the active region is in fact entirely identical (see figure 5.1): two staggered layers of 64 straw tubes each, wire spacing of 5.25 mm, 5.5 mm distance between the two wire planes, Kapton XC+aluminium type tubes mounted directly on sandwich panels with only an inner grounding foil. Electrical contact between straw tubes and grounding foils was provided by spots of silver paint at intervals of 20 cm along the tubes. The straw tubes and anode wires were split midway along the module length, electrically forming two 1.6 m long half-chambers.

For the studies of drift cell behaviour, the set of short straw tube chambers was placed between the poles of the T7 magnet which can deliver a field strength up to 1.37 T. This is close to the highest field to be experienced in any re-

Figure 3.5: Set of 1-metre prototypes.

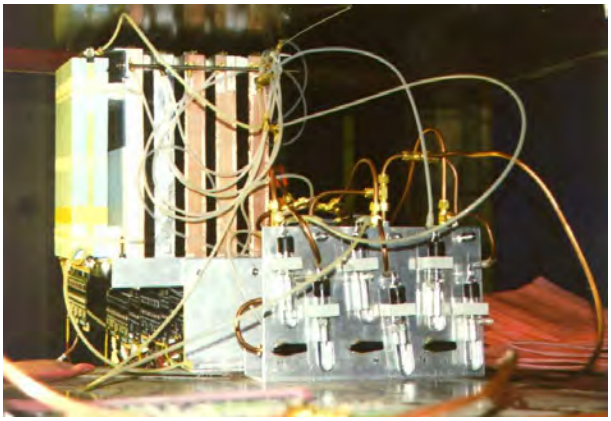

Figure 3.6: Set of short straw tube chambers inside the gap of the magnet at the T7 PS beam line.

gion of the LHCb Outer Tracker. Figure 3.6 shows the short chambers inside the magnet gap. Long prototypes under study were placed closely downstream from the short chambers, with the wires in the same direction. The use of the short module was necessary in order to make track reconstruction possible. The honeycomb chambers HC1 and HC2 were used for a rough measurement of the second track coordinate. These chambers have two staggered layers each, with 32 channels at 9 mm pitch.

The readout electronics and data acquisition system used for the beam tests are described in [24]. The main components are:

- Boards carrying ASDBLR preamplifier chips [5, 25], installed directly on the chambers.
- TDC boards built around the TDC32 chip developed at CERN [26]. This chip provides a time measurement binning of 0.78 ns.
- An event builder (NIMROD module) which combined data from several TDC boards into a single event structure.
- A trigger processor (DDAQT module) which received primary trigger signals from the coincidence of scintillation counters and provided timing signals to the NIMROD module.
- A VME controller, which read out the data from NIMROD via VME bus towards local disk storage.

Studies of drift cell behaviour

The LHCb timing requirement for the Outer Tracker is that all signals should arrive within 50 ns (two bunch crossing intervals). Taking into account signal propagation time in the straw tube, this limits the maximal drift time to 40 ns for the large tracking stations outside the magnet (max. tube length 2.4 m) and 43 ns for the stations inside the magnet at B_{max} ~1.4 T (max. tube length 1.8 m). To meet these requirements, it is necessary to use a fast gas mixture. The common choice is to use a mixture containing CF_4. It was shown in Section 3.1 that gas mixtures based on Ar, CF_4 and CO_2 can be safely used in chambers with Kapton XC cathodes. In our beam tests we studied mixtures with different fractions of Ar, CF_4 and CO_2.

The maximal drift time and Lorentz angle depend on the concentration of CF_4; drift velocity increases with CF_4 concentration. On the other hand, it is well known that CF_4 based mixtures seriously suffer from electron attachment [27]. We indeed observed [20] sizeable effects when comparing ^{55}Fe amplitude spectra for gas mixtures $Ar(65)CF_4(30)CO_2(5)$ and $Ar(80)CO_2(20)$. The high voltages were chosen such that the effective gas gain in both cases was about 2×10^4. The energy resolutions (FWHM) at the full absorption peak (5.9 KeV) for these mixtures were 42.2% and 19.6%, respectively. Assuming that there is no attachment in the Ar/CO_2 mixture, this allows an estimate of the electron attachment coefficient κ, defined as the ratio of the number of ionisation electrons to the number of those reaching the anode, in the $Ar/CF_4/CO_2$ mixture. A sim-

ple method taken from [27] gives κ=4.6, compatible with the value of $\sim$5 reported by [28] for the mixture $Ar(75)CF_4(25)CH_4(5)$. This means that out of the 30-35 ionisation electrons produced on average by a charged particle in a straw tube of 5 mm diameter, only 7 lead to an avalanche at the anode wire. (Note that we performed this measurement for a 65/30/5 composition of the $Ar/CF_4/CO_2$ mixture. For the preferred 75/15/10 mixture, the attachment coefficient has been estimated at $\sim$3 from a measurement of total collected charge per incident particle.)

Such significant loss of ionisation electrons may affect performance. The possible loss of the nearest ionisation cluster leads to a worse drift coordinate resolution. In addition, the pulse height distribution of signals becomes broader, which further spoils the resolution, because of larger jitter on the threshold crossing time. Another effect of the broader dynamic range of signals is the higher fraction of large amplitudes in signal spectra at the same efficiency, which should lead to some increase in cross talk level. The electron attachment increases with the CF_4 concentration. Therefore, for the final system it is preferable to keep the CF_4 percentage as low as possible, within the timing requirements. Another good reason to do so is that CF_4 is rather expensive.

The studies of drift cell properties were performed with the short straw chambers, placed between the poles of the magnet in the area of homogeneous field. The wires were oriented vertically, along the field direction. The threshold of the ASDBLR preamplifiers was set to 2.7 fC. We measured the following performance parameters:

- efficiency, coordinate resolution and cross talk level as a function of high voltage, without magnetic field;
- total drift time as a function of magnetic field, at high voltage values on the efficiency plateau.

All measurements were done for the same plane of straw tubes, viz. the fifth out of eight, counting downstream along the beam. As an example, the drift time spectra for the mixture 65/30/5 at several values of the magnetic field are shown in Fig.3.7. The effect of the magnetic field is clearly seen. The shape and length of the time spectra of the $Ar/CF_4/CO_2$ mixtures are understood, in the sense that they can be closely reproduced with the GARFIELD simulation program [29]. In particular, the characteristic non-monotonous dependence of drift velocity on the electric field manifests itself in these spectra as a bump at 20-30 ns. The total drift time was determined as an interval containing 98% of the signals, with 1% of signals arriving before the beginning and 1% after the end of the interval.

For the measurement of the efficiency, we used the algorithm described in [19]. In order to avoid possible biases, tracks were reconstructed using all layers except the layer under study. The coordinate of the crossing point of the reconstructed track and the studied layer was calculated for each event. Then we looked for a hit in that layer within a certain window around the calculated crossing point. The average straw tube efficiency was calculated as $\epsilon = N_{hits}/N_{tracks} * q_{geom}$, where q_{geom} is a geometrical factor equal to the ratio of wire pitch over straw tube diameter.

Figure 3.8 shows an example of the relation between drift time and track distance from the sense wire. The coordinate resolution was measured in the following way. After proper position calibration and t-r relation fit, the distribution of residuals for all straw tubes in the selected layer was fitted with a Gaussian plus a constant term, and the standard deviation of the Gaussian was taken as the value of the resolution. The fact that the tracks were them-

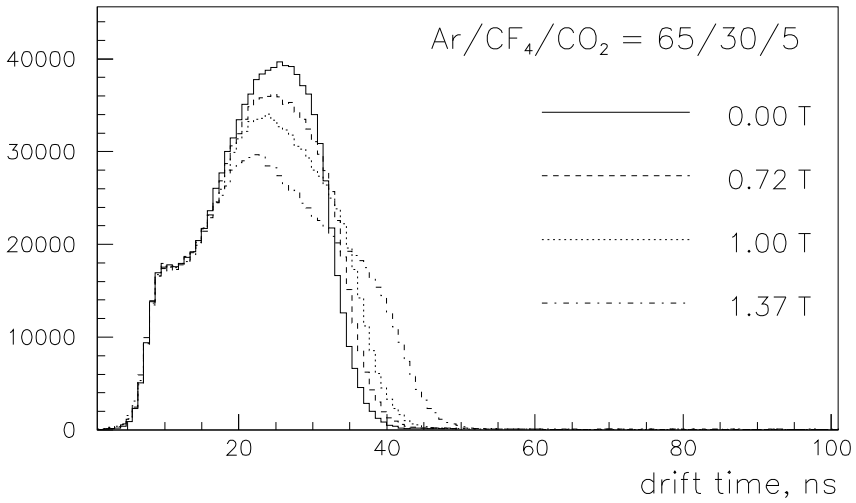

Figure 3.7: Drift time spectra at different values of the magnetic field

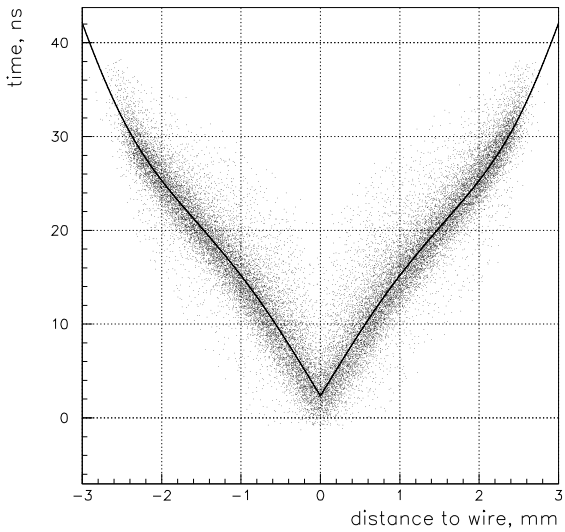

Figure 3.8: Relation between drift time and drift distance in the gas mixture $Ar(75)CF_4(15)CO_2(10)$ without magnetic field.

selves reconstructed with straw tube chambers, was accounted for via proper scaling of residuals [23].

Our definition of cross talk level was the following: for the set of events with one reconstructed track, which had an associated hit in the selected layer, we took as a measure of cross talk level the average number of non-associated hits in this layer per event, assuming that they all arise from cross talk. Of course, the cross talk level in small chambers may differ from that in the final system. In the test beam studies, the cross talk level was rather an indirect measure of the dynamic range of signals, and used for comparison of gas mixtures.

The total drift times for seven different gas mixtures at four values of magnetic field are given in Table 3.1. From this table one can conclude that the mixture 75/15/10 is the one which has minimal CF_4 content and still meets the LHCb timing requirements for all stations.

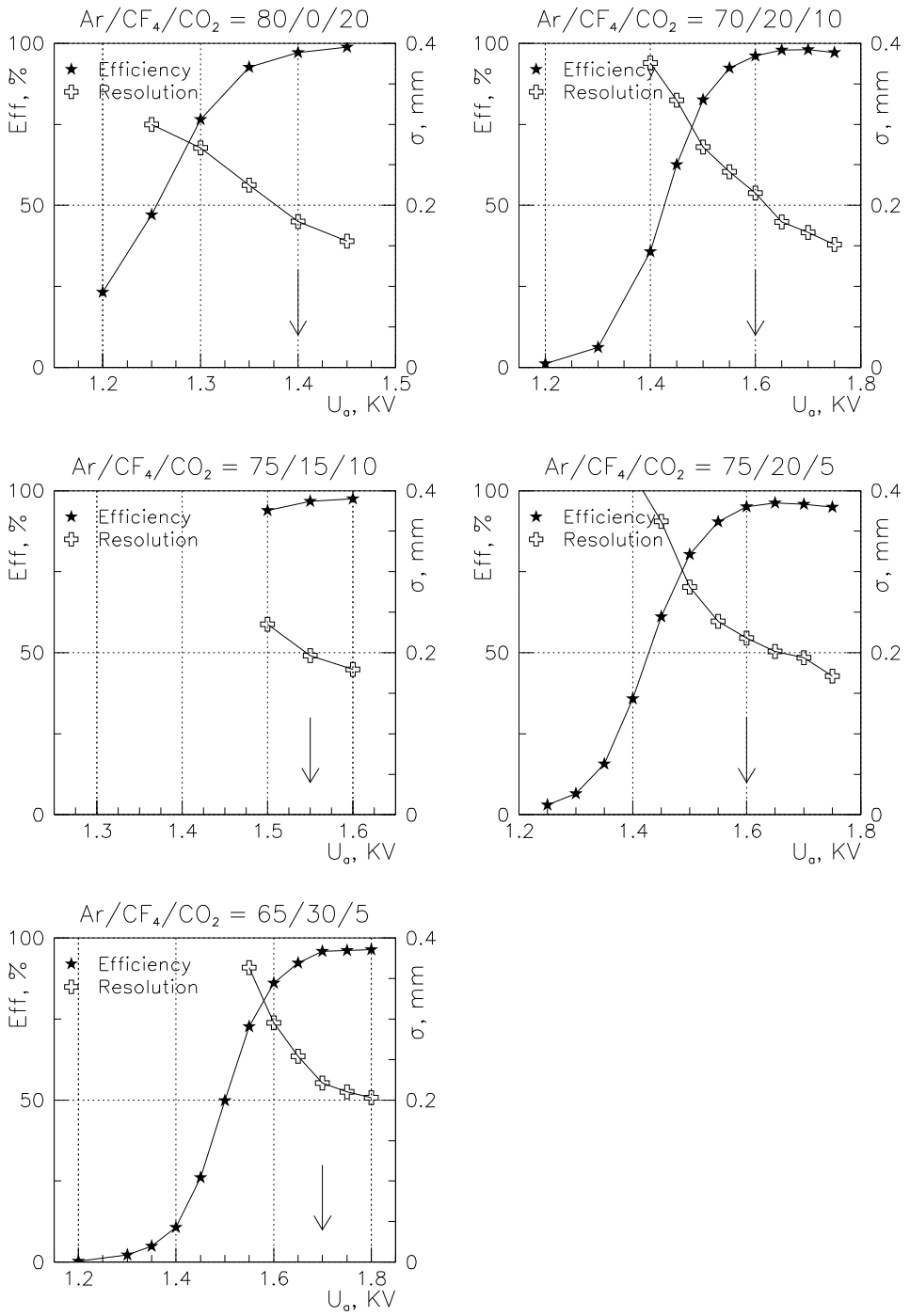

Figure 3.9: Efficiency and resolution as a function of high voltage for various gas mixtures

mixture $Ar/CF_4/CO_2$	τ, ns B = 0 T	τ, ns B = 0.72 T	τ, ns B = 1.0 T	τ, ns B = 1.37 T
80 / 0 / 20	41.2	43.2	44.8	49.1
65 / 5 / 30	39.0	40.5	42.2	45.1
75 / 15 / 10	**32.5**	**34.5**	**36.3**	**40.9**
75 / 20 / 5	31.4	33.1	35.1	40.8
70 / 20 / 10	31.4	33.0	35.2	39.3
70 / 25 / 5	29.2	30.9	32.8	37.5
65 / 30 / 5	28.2	30.1	32.0	36.0

Table 3.1: Total drift times for various mixtures and magnetic field values

mixture $Ar/CF_4/CO_2$	U, kV	eff, %	σ, μm	τ, ns B=0 T	τ, ns B=1.37 T	cross talk
80 / 0 / 20	1.40	97.2	180	41.2	49.1	6.1 %
75 / 15 / 10	**1.55**	**96.7**	**196**	**32.5**	**40.9**	**6.0 %**
75 / 20 / 5	1.60	95.0	218	31.4	40.8	5.0 %
70 / 20 / 10	1.60	96.2	215	31.4	39.3	5.4 %
65 / 30 / 5	1.70	95.9	221	28.2	36.0	4.9 %

Table 3.2: Parameters of gas mixtures at the beginning of the plateau.

The coordinate resolution and efficiency as functions of the high voltage are shown in Fig. 3.9 for five gas mixtures. The arrows point to the beginning of the plateau, which was taken as the lowest HV at which the efficiency exceeds 95%. The essential parameters of these gas mixtures are given in Table 3.2. The effect of CF_4 concentration is visible, but is not dramatic. The drift coordinate resolution at the beginning of the plateau is correlated with the percentage of CF_4, rising from 180 μm for the mixture without CF_4 to 220 μm with 30% of CF_4. In cross talk level there is no clear effect at all: the variations from 4.9% to 6.1% are not correlated with CF_4 content, and can rather be attributed to the precision of determination of the beginning of the plateau (the high voltage scanning step was 50 V).

Summarising, the optimal gas mixture for the Outer Tracker is $Ar(75)CF_4(15)CO_2(10)$. If found necessary during LHCb operation, the CF_4 content can be varied between nil and 30 % without major influence on resolution and efficiency.

Studies of a full scale prototype.

The full scale prototype described above was tested at the CERN PS beam in April 2001. We used the selected gas mixture $Ar(75)CF_4(15)CO_2(10)$. The resolution of the ancillary short chambers was $\sim$180 μm, see Fig. 3.9. We tested the long module at 10 points along its length, i.e. at 5 points per half-length module. At each point, efficiency, drift time resolution and cross talk level were measured at several values of high voltage. The dependence of efficiency and resolution on high voltage at one of the points (120 cm from the preamplifiers) is shown in Fig. 3.10. Fig. 3.13 shows the module performance (efficiency, resolution and cross talk level) as a function of beam position. The origin of the horizontal axis corresponds to the split between the two half-

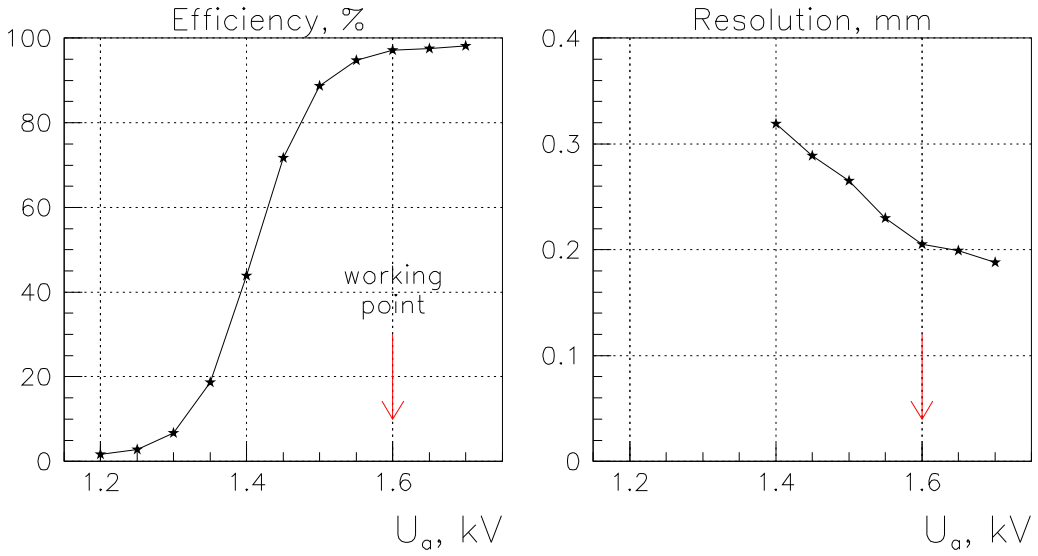

Figure 3.10: Efficiency and resolution in the long prototype as a function of high voltage

modules. The chamber shows high efficiency and good coordinate resolution. Digital cross talk is at the acceptable level of 5 %. The performance is very uniform over the whole module length and validates the decision to have no electrical termination of the wire ends at the split. The slight increase of efficiency and cross talk and slight improvement of resolution towards the centre of the module agree with the expectation that the signal amplitude from the far end of a wire is maximal (see Fig. 3.1). Cross talk between the two layers of a half-module and between the half-modules was found to be negligible (<0.3 %).

The efficiency scan of a straw tube in the region around a wire locator is shown in Fig. 3.11. One sees that the 10 mm long wire locator causes an inefficiency zone of about 12 mm FWHM. The presence of wire locators did not cause any problems with stability of operation. Module efficiency is the logical OR of the efficiencies of the two individual straw tube layers. An efficiency scan over the width of the long prototype is shown in Fig. 3.12. The module efficiency is around 99.8 %.

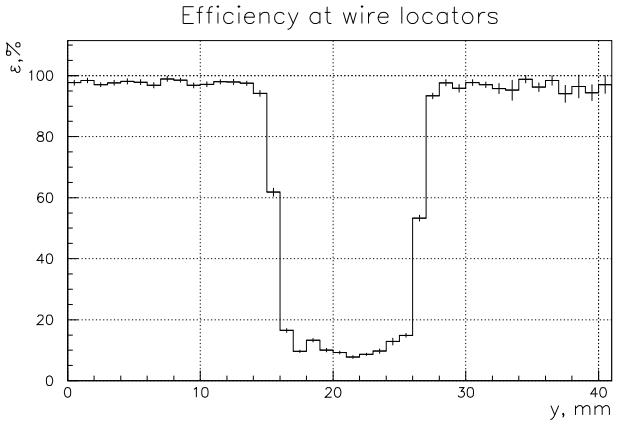

Figure 3.11: Efficiency scan in the region of a wire support

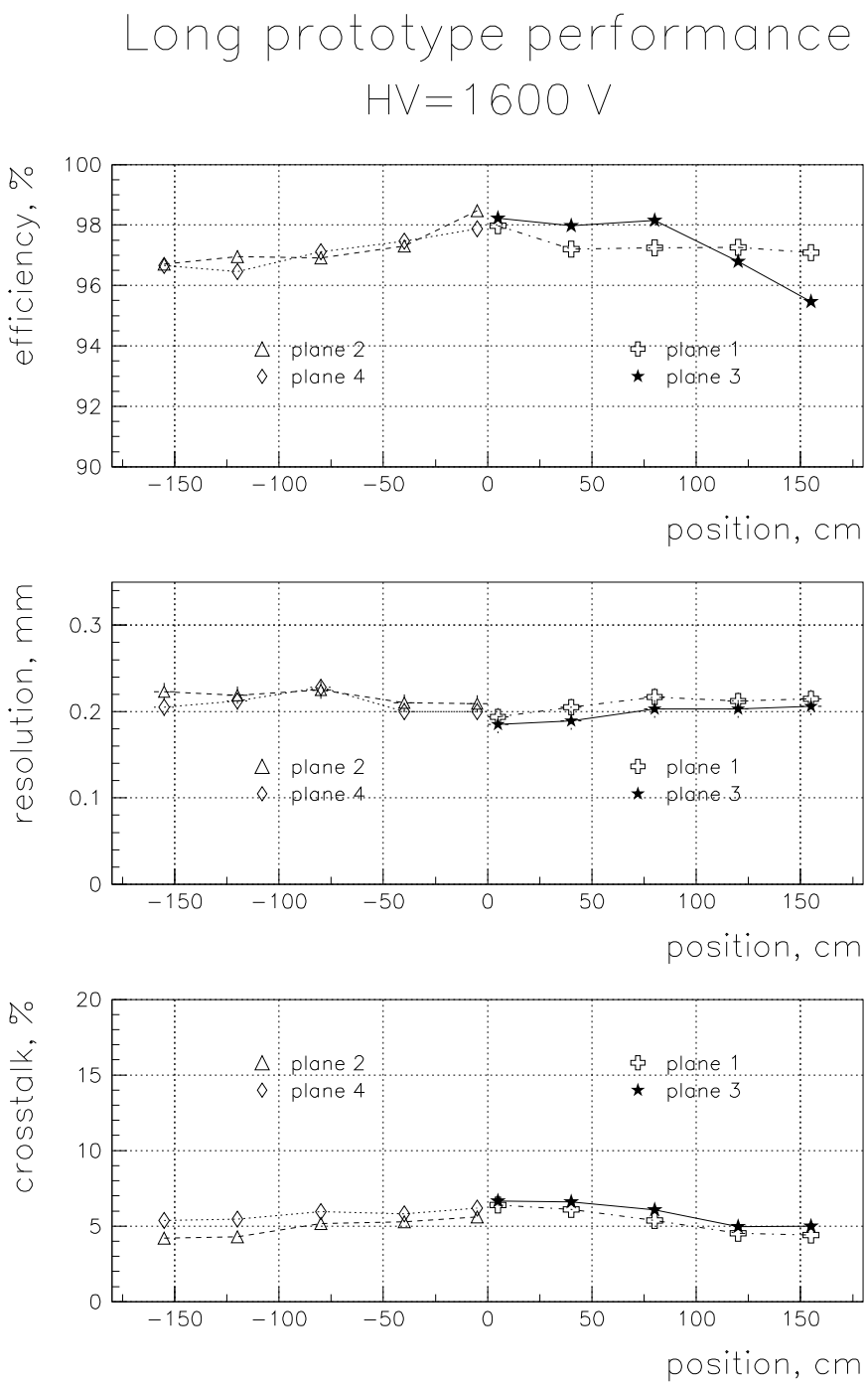

Figure 3.13: Efficiency, resolution and cross talk level in the long prototype as a function of position along the tube.

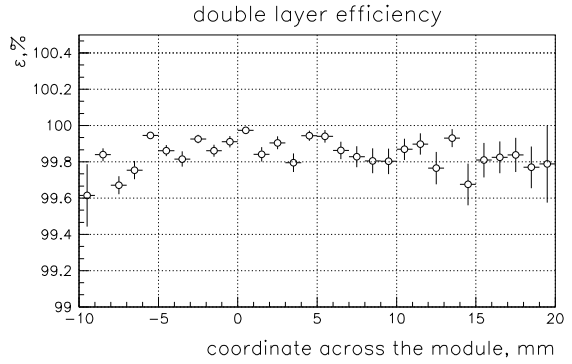

Figure 3.12: Efficiency scan of the full scale prototype over the width of the module.

Gain stability

Drop in gas gain due to space charge effects has been measured by straw tube irradiation with 9 keV X-rays. At the 1550 V working point of the default gas mixture $Ar(75)CF_4(15)CO_2(10)$, the gain remained constant up to a flux of 20 kHz/cm and dropped by 5 (12) % at 50 (100) kHz/cm. Since the number of ionisation electrons per 9 keV photon is 10 – 12 times as high as for a minimum ionizing particle, this result indicates constancy of gas gain up to the highest local particle flux in the Outer Tracker, estimated at 250 kHz/cm in section 3.1.

3.4 Aging tests of prototype modules

A prototype module containing two layers of 32 Kapton XC straw tubes of 2 m length was installed close to the proton beam pipe during the HERA-B run of the year 2000. The module closely resembled the final layout (presence of wire locators etc.) and was operated with $Ar(65)CF_4(30)CO_2(5)$ drift gas. Currents and signal amplitudes were monitored. The hottest straw tube received an integrated charge dose of 0.8 C, with an estimated highest local dose of 55 $\pm$ 14 mC/cm. Straw tube currents normalised to the HERA-B interaction rate remained constant and there were no significant changes in pulse height distribution. Before and after the HERA-B exposure, signal currents were measured as a function of the position of a ^{90}Sr source along the straw tube length. With as movable slit arrangement, the tubes were scanned in steps of 1 cm. The current profiles of individual wires measured before and after the irradiation in HERA-B are identical, see the example in fig. 3.14.

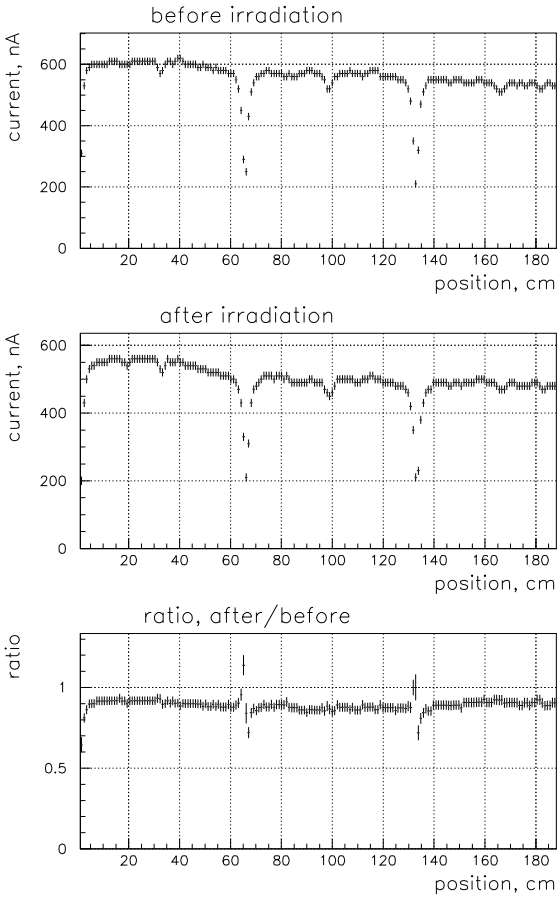

Figure 3.14: Current from a straw tube as a function of irradiation position, before and after exposure of the straw tube module in HERA-B.

The deep dips show the positions of the wire

locators. Three smaller dips occur where the tube was externally supported, which slightly displaced the tube centre from the anode wire. The wire end at the origin of the plot had received a much higher charge dose than the end at x = 180 cm, so an effect on the current-to-voltage relationship should have shown up as a general slope superimposed on these local features. The plot of current ratios does not show a significant effect. (The difference in absolute current values of the two curves is due to a slightly different source mounting.) Measurement of current profiles will be included in the acceptance tests of series production modules. It provides a fast check that the anode wire is sufficiently well centred in the tube for operational stability.

Exposure tests in HERA-B will continue. They offer the unique possibility to irradiate complete modules in a realistic environment. In 2001 and 2002, modules will be placed near the beam pipe behind the HERA-B electromagnetic calorimeter, where they will be exposed to particle rates up to 10 times higher than expected in LHCb. Accelerated aging tests with an X-ray source (factor 20 with respect to real life in LHCb) are also under way.

3.5 Conclusions

1. Having decided to use 5 mm diameter drift cells only, sufficiently fast drift can be obtained with a gas mixture that contains only 15 % of CF_4, at all magnetic field values that will be experienced by Outer Tracker detector modules. With the default gas mixture $Ar(75)CF_4(15)CO_2(10)$ the design value of 200 μm drift coordinate resolution per drift cell has in test beam conditions been realized. If in actual LHCb running conditions a somewhat faster drift turns out to be advantageous, the CF_4 content can be increased without seriously affecting the resolution. For instance, by switching to the mixture $Ar(65)CF_4(30)CO_2(5)$ the drift time window is shortened by 12 % at the expense of a 10 % loss in drift time resolution. In order to minimise the risk of aging of drift tube materials, the guideline will be to operate the detector with the lowest possible CF_4 concentration in the drift gas.

2. The straw tubes will have an inner winding of carbon doped polyimide (Kapton XC). An outer winding of 25 μm aluminium provides good cross talk suppression, much better than can be achieved with a common shielding foil between layers of tubes that are not self shielding. In all other respects, tubes with different outer windings show essentially the same behaviour. Thus, self shielding tubes will be used. The phenomenon of resonant coupling between such tubes was not anticipated. Its suppression in the frequency range of the preamplifier bandwidth requires good Ohmic contact between the tubes, continuously along their length or at intervals of not more than 20 cm. The contact may be directly from tube to tube or via the aluminium cladding of the sandwich panel carrying the tubes.

3. Wire supports of Noryl (and other materials) have been tested in various shapes. They do not noticeably affect high voltage stability. Drift tubes remain fully efficient to 2 mm from the edge of the support.

4. The ASDBLR preamplifier suits our requirements. Matching of the input impedance to the characteristic impedance of the straw tube transmission line will be improved by addition of a 150 Ω discrete resistor. The effective dead time of the preamplifier after arrival of a signal, i.e. the limit it sets on double pulse resolution, depends on pulse amplitude. At the foreseen working point the mean value is 35

ns. This is close to the collection time of ionisation clusters along a track segment, which means that the preamplifier does not significantly degrade the double pulse resolution. Still, comparing with the 50 ns time window of signal arrivals within a single event, it is clear that the drift tubes have essentially no double hit capacity per event. This fact has been taken into account in the performance simulations reported in chapter 4. It has been decided to leave the far end of anode wires electrically open, instead of suppressing signal reflection with a terminating impedance. The amplitude gain of signals from the far end weighs heavier than the increase in effective dead time for signals from the near end which have the longest delay between direct and reflected pulse.

5. According to laboratory tests, digital cross talk from an active straw tube to all surrounding tubes is, at high voltage and discriminator threshold settings as used in beam tests, intrinsically at the level of 3 %. Some contribution from cross talk in front end electronics must still be added. Test beam results typically show a total cross talk rate of 5 %. This value has been included in performance simulations.

4 Performance

Performance studies of the LHCb tracking system have gone through several iterations, to follow the evolution of the hardware design of the experiment since the Technical Proposal. A particularly important improvement has been the replacement of the aluminium beam pipe foreseen in the Technical Proposal by a beam pipe of aluminium-beryllium alloy. On the other hand, early estimates of the material budgets of subdetector systems have been too optimistic.

The design of the tracking system has been re-evaluated in the light of these changes, in particular with respect to:

- the number of stations and their positions
- the definition of the border line between Inner and Outer Tracker
- the choice of the angle of the stereo planes

The following performance indicators have been used for design optimisation:

- detector occupancy
- track finding efficiency
- track parameter resolutions

The performance has been studied with simulated $b\bar{b}$ events and minimum bias background events, mimicking the expected LHCb particle environment. In this chapter the procedures of event generation and detector response simulation are outlined. The results of the optimisation studies are summarised and strategies for the inclusion of tracking information in the level-2 trigger are presented. For the proposed detector set-up the efficiencies for reconstructing the final state particles of two benchmark B-decays and the reconstructed mass resolutions are calculated.

4.1 Event simulation and detector response

Simulation studies are based on the following programs: Pythia+QQ, SICB/GEANT, TRAIL/GAUDI. Proton-proton interactions at $\sqrt{s} = 14$TeV are generated using the Pythia (v6.1) event generator [30], using a multiple-interaction model characterised by varying impact parameter and a running p_T cut-off. The model parameters have been tuned [31] to reproduce existing low-energy data. Particle decays are handled by the QQ package [32], which relies as much as possible on measured branching fractions. The resulting final state particles are tracked through the LHCb detector setup with the SICB program [33] which is based on GEANT3 [34]. All particle interactions with materials in the detector are simulated and the energy loss in the sensitive detector elements is recorded. The Outer Tracker detector response (the measured drift time) to these energy depositions is simulated in the GAUDI/OTR software. Finally the response signals of the Outer Tracker, the Inner Tracker and the VELO are simultaneously analysed in the TRAIL package, performing the track reconstruction. Apart from the Pythia and GEANT event simulations, the detector response and track reconstruction programs are object oriented C++ software.

4.1.1 Detector description

The detector geometry and response are simulated in detail. Detector modules of the Inner and Outer Tracker are individually implemented, including realistically staggered z-positions, overlap areas of Inner and Outer Tracker and dead spaces. The geometry is illustrated in the GEANT drawings shown in fig 4.1. A simulated module of Outer Tracker straw

tubes consists of two staggered layers of tubes, sandwiched between two cover plates, with an equivalent amount of 0.67 % X_0 material (see section 5.1.2). Dead areas between modules are taken into account. Additional materials inside the fiducial volume (Inner Tracker mounting frames, cables at localised areas) are implemented.

For each track, the entrance and exit point in the module, as well as the time-of-flight of the track and the energy lost traversing the module, are stored and used as starting point of the detector response simulations.

4.1.2 Detector response

The Outer Tracker detector response simulations are described in detail in [36]. They have been tuned to prototype results obtained in test beam experiments.

Drift time

The relation between drift time t and track impact parameter d with respect to the sense wire is approximated with the linear relationship

$$t = t_{max} \times \frac{d}{r_{cell}}$$

where r_{cell} is the cell radius and t_{max} is the maximum drift time in the cell, taking into account the local magnetic field strength. Assuming the drift gas to be $Ar(75)CF_4(15)CO_2(10)$, the maximum drift time as function of the magnetic field is parametrised as:

$$t_{max}(B) = p_0 + p_1 \times B^2$$

with $p_0 = 32.5$ ns and $p_1 = 3.9$ ns T^{-2}.

Since the dependence of the drift coordinate resolution on the magnetic field is small, a constant single cell resolution of 200 μm is assumed (see table 3.2).

Efficiency

The single cell efficiency η is parametrised as:

$$\eta(l) = \eta_0 \ (1 - e^{-\rho l})$$

where l is the path length of the traversing particle in the cell and ρ can be thought of as an effective ionisation density which contains effects of electron attachment and discriminator threshold setting. The test beam data are well described by this parametrisation with the fitted parameters $\eta_0 = 0.99$ and $\rho = 1.47 mm^{-1}$, representing an overall efficiency of 97 % of a straw tube.

Time window

The last ingredient of the response simulations concerns the finite window of 50 ns for acceptance of a hit. Each track hit is assigned a digitisation time which is taken as the sum of the time-of-flight of the traversing particle, the drift time in the tube and the signal propagation time towards the preamplifier. The sensitive time window has a different offset for each station in order to compensate for the time-of-flight of the particles. If the digitisation time falls inside the window, the hit is registered, if not the detector is inefficient for this track. As a consequence, curling tracks in the magnet area can become invisible to the simulated detector. On the other hand, curling tracks from previous crossings can contribute hits to the event. Finally, a dead time of 30 ns is taken into account following each hit. A second hit within 30 ns in the same straw tube will not be registered.

4.1.3 Simulation of multiple interactions

The tracking system is designed to operate at an average luminosity of $\mathcal{L} = 2 \times 10^{32} cm^{-2} s^{-1}$, while it should be able to function for limited periods at a maximal luminosity of $\mathcal{L} =$

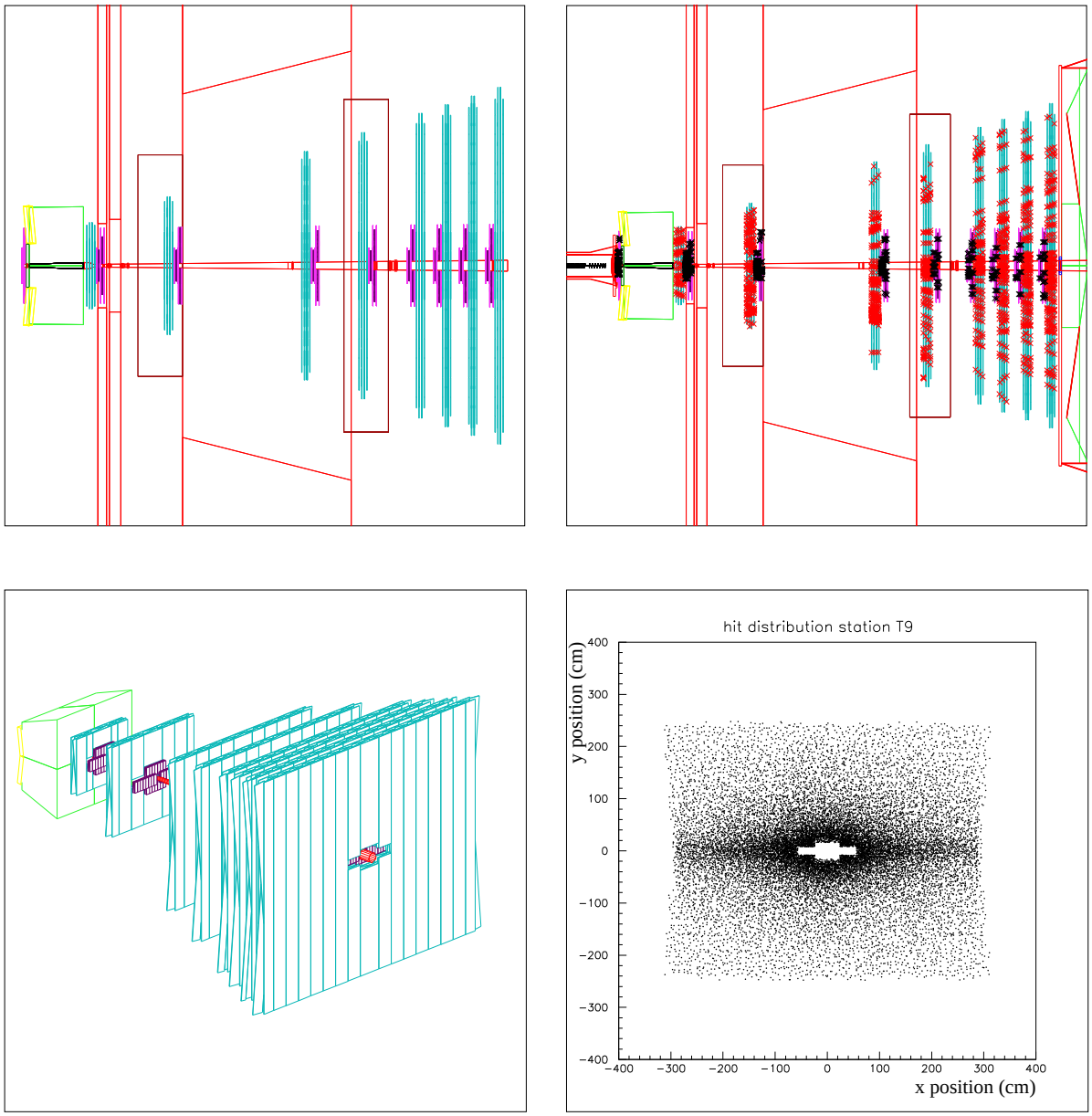

Figure 4.1: Implementation of the simulated tracking system: a) $x - z$ view of the station arrangement; b) hits observed in a typical event; c) a 3-d view of the spectrometer; d) hit distribution in station T9 integrated over 1000 events

$5 \times 10^{32} cm^{-2} s^{-1}$. We refer to these operation modes as "nominal" luminosity and "high" luminosity running, respectively.

Operation at these luminosities implies that in a given $b\bar{b}$ event there will be two sources of background observed by the detectors:

- *"Pile-up":* backgrounds from one or more pp interactions occurring in the same bunch-bunch collision as the $b\bar{b}$ event. At nominal and high luminosity the number of minimum bias interactions per bunch-bunch collision is Poissonian distributed with averages of 0.53 and 1.33, respectively.

- *"Spill-over":* backgrounds from previous or subsequent bunch-bunch interactions. Detector signals from consecutive bunch crossings can overlap for the following reasons:

  - The time-of-flight of curling tracks in the magnet can reach up to hundreds of nanoseconds ("loopers"). As a consequence, a triggered event might contain hits in the magnet stations belonging to tracks from much earlier collisions.
  - The maximum signal delay of a straw tube is 50 ns, i.e. the sensitive time window is equal to a period of two bunch crossings. In practice this implies that an outer tracker read-out event will contain, in addition to the hits from the current crossing, hits due to interactions in neighbouring bunch crossings. If an event occurred in the previous bunch-bunch collision, all hits with drift times larger than 25 ns will occur in the sensitive time window. If an event occurred in the subsequent bunch-bunch collision, all hits with drift time less than 25 ns will fall inside the window.

The spill-over background is, just as pile-up, luminosity dependent. At higher luminosity the probability for a minimum bias event to occur in a neighbouring bunch crossing increases. A $b\bar{b}$-event produced at $t = 0$ while running at nominal luminosity will on average contain the following relative hit contributions from consecutive bunch crossings: 0.6 % (t_0 = -75 ns), 2.1 % (t_0 = -50 ns), 11.0 % (t_0 = -25 ns), 80.3 % (t_0 = 0), 6.0 % (t_0 = 25 ns). The effect is not symmetric over spills before and after t=0 due to the time-of-flight effects. The numbers quoted are averaged over all stations. For station T4 they are somewhat different due to the presence of looping tracks in the magnet; loopers produced at t_0 = -100 ns or earlier contribute 1.5 %. This effect, only present in station T4, has been neglected in further simulations.

In the following, the term *event* will be used to include hits from pile-up and spill-over in addition to hits from the $b\bar{b}$ event proper.

4.1.4 Detector occupancies

The detector occupancy is defined as the fraction of channels in a specified detector region that is hit within the 50 ns time window of an event. Occupancy values are important ingredients in the optimisation of the combined layout of the Inner and Outer Tracker detectors.

Pattern recognition studies show that the efficiency of track reconstruction drops when occupancy rises, while ghost rates increase. We have arrived at the following requirements:

- The *average* occupancy in the hottest parts of the track seeding stations should be less than 10 %.

- The *average* occupancy in the hottest parts of the magnet stations should be less than 15 %.

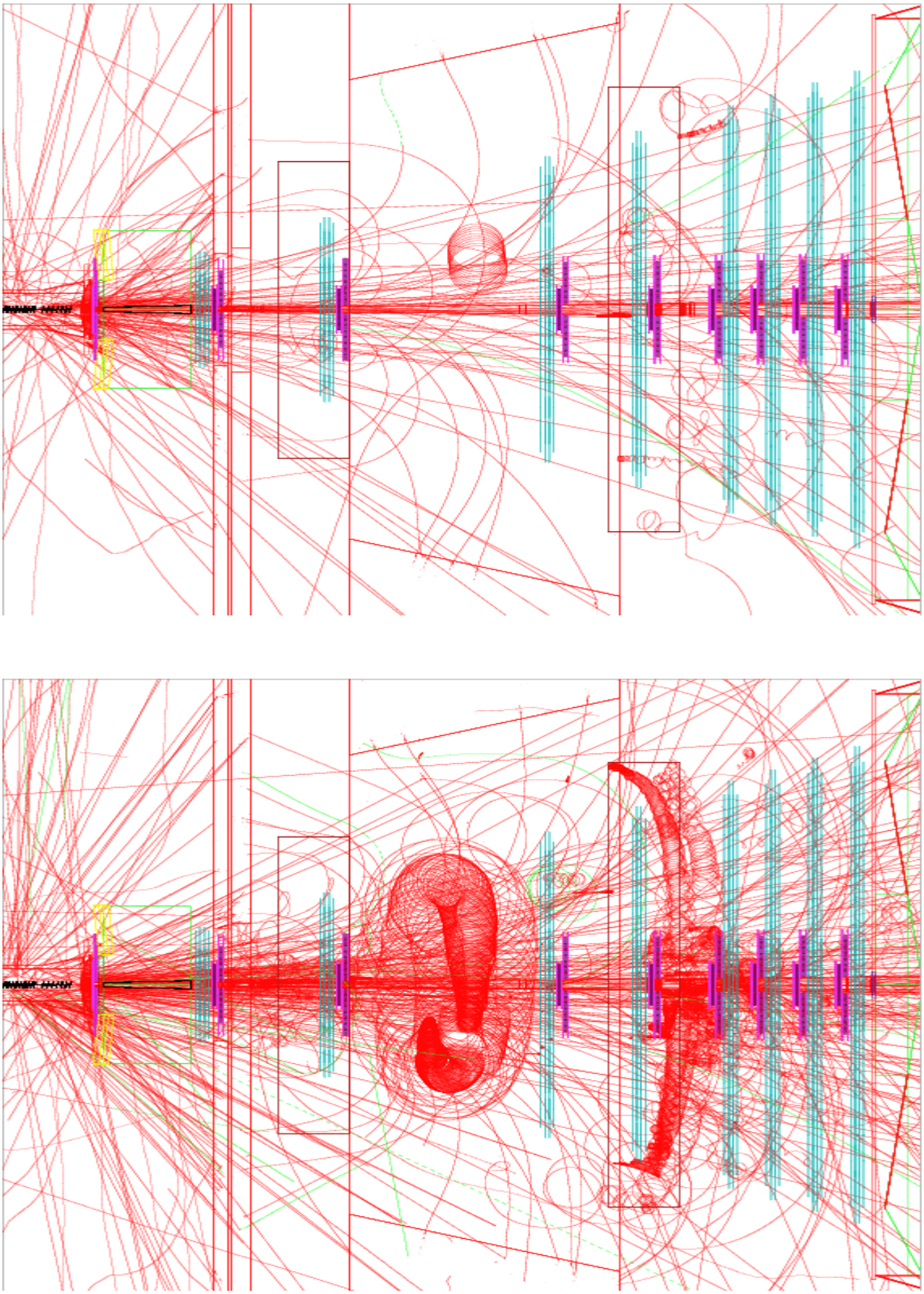

Figure 4.2: Event displays of simulated $B \to \pi^+\pi^-$ events. Top: event with low track multiplicity. Bottom: event with high track multiplicity.

There are two factors that determine the occupancy: the number of incident tracks and the granularity of the detector. The total number of tracks seen in the event consists of primary tracks from the pp-interaction and secondary tracks originating from interactions with the detector or beam pipe material. The number of primaries and the number of secondaries per primary track both follow statistical distributions, with large fluctuations from event to event. As a result, one can distinguish typical low multiplicity ("quiet") and high multiplicity ("crowded") events. Examples of a quiet and a crowded $B \rightarrow \pi^+\pi^-$ event are given in fig.4.2.

In a first approximation[6] the track density in a measurement plane perpendicular to the beam line scales as $1/r^2$, where r is the distance to the beam line. To keep the detector occupancy low, the region around the beam pipe is equipped with the fine grained Inner Tracker, and the outer region by the more coarsely grained Outer Tracker. Occupancy studies are reported in detail in [37] and [38]. As an example figure 4.3 shows the average cell occupancy in station T7 as function of the x-coordinate of the straw tube. The steps at $x = 255$ mm and at $x = 596$ mm reflect the "cross" geometry of the boundary between Outer and Inner Tracker. The tuning of that boundary towards acceptable occupancies in all parts of the detector is discussed in section 4.2.3.

The large event-to-event fluctuations in track density lead to large fluctuations in the detector occupancy. As an example, the occupancy distribution for a densely occupied region in station T3 is shown in fig 4.4. The average occupancy in this region is 17 %, but a tail up to 40 % occupancy is observed. The fact that the distributions have a long tail of high occupancy implies that events will occur that are very difficult to treat both in the trigger and in the reconstruction.

[6]Clearly, for curling tracks in the magnetic field this approximation does not hold.

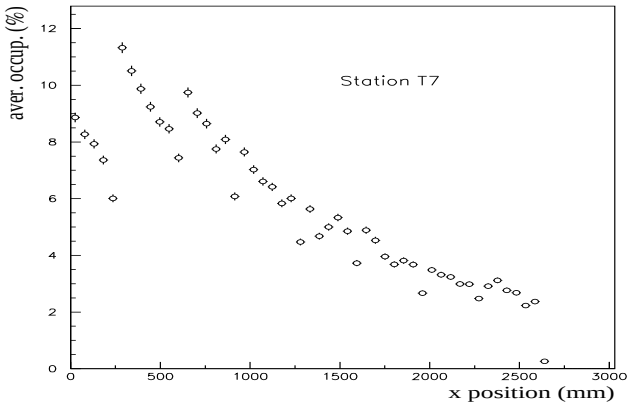

Figure 4.3: Average channel occupancy as a function of position in station T7.

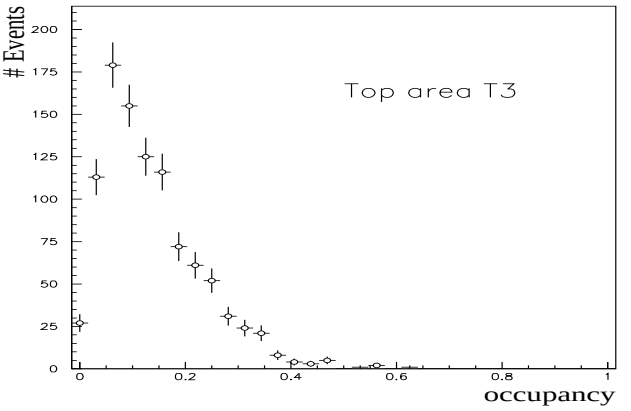

Figure 4.4: Occupancy distribution on event-to-event basis for a cell just above the Inner Tracker in station T3. (see Fig. 4.7)

4.2 Detector Optimisation

4.2.1 Station positioning

In the optimisation process we considered the following general requirements:

- Limit as much as possible the number of tracking stations, in order to minimise the amount of material in the spectrometer.
- Avoid a tracking station in the central part of the magnetic area, where the track density is highest.
- Since flanges in the beam pipe are a source of secondaries, stations should not be placed just behind them.

More specifically, the requirements for positioning of individual stations are the following:

- *Stations T1 and T2:* Stations T1 and T2 are placed immediately before and after the RICH 1 detector, such that the track interpolation between T1 and T2 suffers minimally from multiple scattering distortions in the entrance and exit windows of the RICH detector. Recent studies [39] suggest that the Inner Tracker station T1 might not be needed, since the trajectory at the upstream side of RICH 1 is measured accurately by the VELO. Station T2 performs an important role in the track momentum measurement. Except for tracks of highest momenta, the measurements in the vertex detector are less effective in the momentum fit, due to multiple scattering in the RICH and VELO detectors. This effectively decouples the trajectory measurements in the vertex area from the momentum measurement in the main tracking area.
- *Station T3:* This station is essential in downstream track following. It must be positioned in the "turn-on" region of the magnetic field: no too far in the magnet such that a straight line trajectory is still a fair approximation, but far enough into the field to gain momentum information in order to extrapolate to station T4. Due to the fast turn-on of the field on the upstream side of the magnet, the positioning of station 3 is rather delicate. For instance, placing it 30 cm closer to the vertex region would result in a 10 % to 40 % reduction in downstream track following efficiency, where the size of the reduction depends on the track momentum.
- *Stations T4 and T5:* The central region of the magnet should be avoided because of the high density of curling secondary tracks. The two stations are positioned for optimal performance of the upstream track following algorithm. They are positioned such that the number of possible track continuations is equal in T4 and T5.
- *Stations T6 - T9:* The four tracking stations in the seeding region must be placed such that the lever arm in the region of low magnetic field is maximised, while at the same time tracks remain close to straight lines. For a 2 GeV/c track the deviation from a straight line between T6 and T9 is approximately 1 cm.

4.2.2 Beam pipe

The number of secondary particles in an event depends on the amount of material seen by incident primary particles. A particularly sensitive area is the very forward region where the track density is high, i.e. the beam pipe. Since the Technical Proposal the design of the beam pipe has undergone many improvements, resulting in the baseline design of an aluminium-beryllium

alloy pipe, with a reduced number of massive elements (flanges, bellows) in comparison to the Technical Proposal.

The large impact of the beam pipe on occupancy is illustrated in fig 4.5. In this plot the relative increase in Outer Tracker occupancy is shown for five different beam pipe designs, compared to an imaginary situation of no beam pipe. Averaged over the different tracking stations, the presence of the aluminium-beryllium pipe increases the detector occupancy by 60 %. For the aluminium – stainless steel pipe described in the Technical Proposal, the increase was 200 %. The solution of asymptotic luxury (a full beryllium pipe) would even reduce the effect to approximately 30 %.

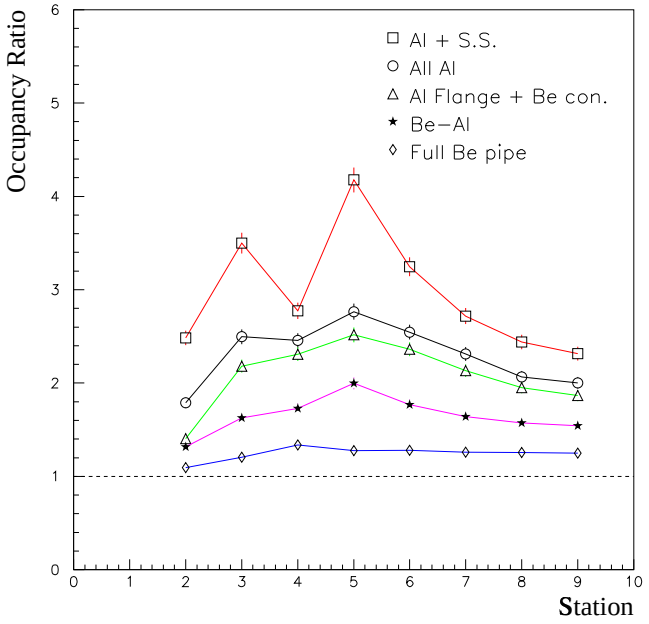

Figure 4.5: Relative change of Outer Tracker occupancy in each tracking station for various beam pipe designs: 1) aluminium pipe with stainless steel flanges; 2) full aluminium pipe including aluminium flanges; 3) aluminium pipe with beryllium parts; 4) aluminium-beryllium alloy pipe; 5) full beryllium pipe.

4.2.3 Inner boundary of the Outer Tracker

Since the track density decreases with distance from the beam, the limit on acceptable occupancy determines where the boundary between the high granularity Inner Tracker and the coarser grained Outer Tracker should lie. Table 4.1 shows average Outer Tracker occupancies in the areas *above* and *aside* the Inner Tracker for several values of the height and width of the Inner Tracker. Comparing these results with the requirements of maximally 10 % (15 %) average occupancy in the seeding (magnet) stations, it is clear that a rectangular Inner Tracker would have to be considerably larger than foreseen in the Technical Proposal, where its dimensions were assumed to be 60 cm (width) x 40 cm (height).

ITr Height	OTr *top* area occup.			
	T2	T3	T4	T5 - T9
40 cm	15%	22%	10%	8%
60 cm	9%	15%	6%	6%
80 cm	6%	10%	5%	5%
ITr Width	**OTr *side* area occup.**			
	T2	T3	T4	T5 - T9
60 cm	13%	20%	14%	14%
80 cm	11%	16%	12%	12%
120 cm	7%	12%	10%	10%

Table 4.1: Outer Tracker occupancy in the hottest areas around a rectangular Inner Tracker of different values of height and width.

The cross shaped boundary shown in figure 2.2 allows to fulfil the Outer Tracker occupancy requirement at minimum surface area of the Inner Tracker. The precise size of the cross was chosen such that Inner and Outer Tracker modules of standard widths can be used. The occupancies of the hottest Outer Tracker areas in case of the cross geometry are shown in figure 4.6. Their locations are indicated in figure 4.7.

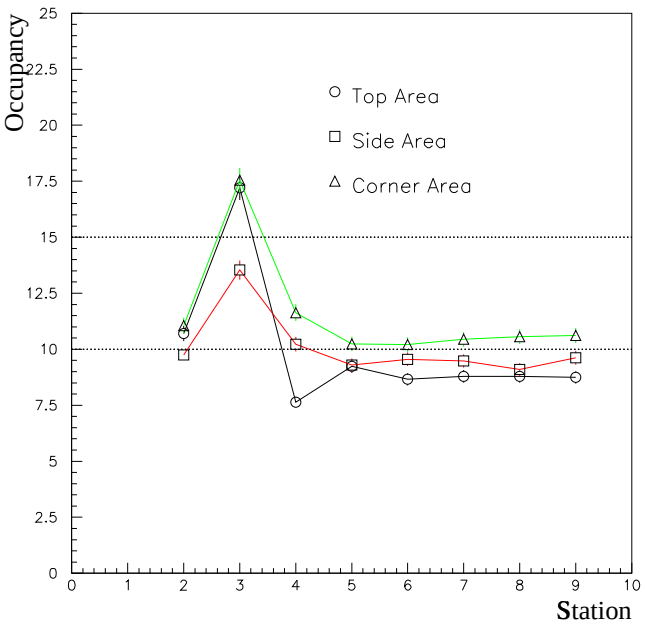

Figure 4.6: Occupancies in the hottest Outer Tracker areas for each station with the final detector dimensions. The areas are: 1) *above and below* the Inner Tracker, 2) *aside* of the Inner Tracker, 3) in the *corner* of the cross. Occupancy values are plotted in units of 1 %.

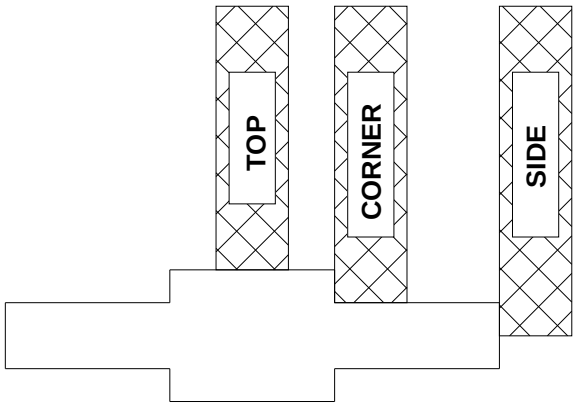

Figure 4.7: The "top", "side" and "corner" areas of highest Outer Tracker occupancy.

4.3 Track Reconstruction

Tracks are reconstructed by combining hit measurements of the Outer Tracker, Inner Tracker and VELO [40, 41]. Although tracks can be reconstructed independently in the vertex region and in the main tracking region, a similar separation between tracks of Outer and Inner Tracker is not practical. Instead, the reconstruction across the main tracking spectrometer uses hit information from both detector systems in an integrated fashion. It is for this reason difficult to separate the Outer Tracker and Inner Tracker contributions to the track reconstruction performance. The numbers presented in this section reflect the performance of the total tracking system. The simulated Inner Tracker is entirely a silicon detector with realistic resolutions and efficiency, as described in [42].

4.3.1 Track fitting

We use the Kalman filter method to reconstruct tracks across the spectrometer. The aim is to reconstruct the full track state vector and the covariance matrix from measured track impact points in a sequence of detection planes perpendicular to the beam axis (z-axis). We have chosen to parametrise the track state vector as $(x, y, t_x, t_y, Q/p)$, where the slopes are defined as $t_x = p_x/p_z$, $t_y = p_y/p_z$, and Q is the particle charge. The track fit procedure is described in detail in [40, 43].

In the final result, the Kalman Filter method is mathematically equivalent to a least-squares fit. However, it combines several advantages which make it very attractive for track reconstruction in LHCb:

- The progressive inclusion of measurements avoids the need for time-consuming global fitting at each step in the track search.

- Random perturbations to the track trajectory due to multiple scattering and energy loss in the detector material can be efficiently included into the fit, also for inhomogeneously distributed material.
- Measurements from detectors using different technologies and different measurement angles can be combined in a straightforward manner.

The momentum resolution for minimimum ionising particles is plotted in figure 4.8 as function of the particle momentum. The observed resolution can be parametrised as follows:

$$(\delta p/p)^2 = A_{ms}^2 + (B_{res} \times p)^2$$

with $A_{ms} = 3.84 \times 10^{-3}$ and $B_{res} = 3.6 \times 10^{-5}$. The first term represents the contribution from multiple scattering, the second term is due to the finite coordinate resolution of the detectors. Comparing the values of the constants A_{ms} and B_{res}, one sees that the momentum resolution is up to 100 GeV/c dominated by multiple scattering. At higher momenta the detector resolution becomes more important. The distribution of momentum resolution for all tracks above 1 GeV/c is displayed in figure 4.9.

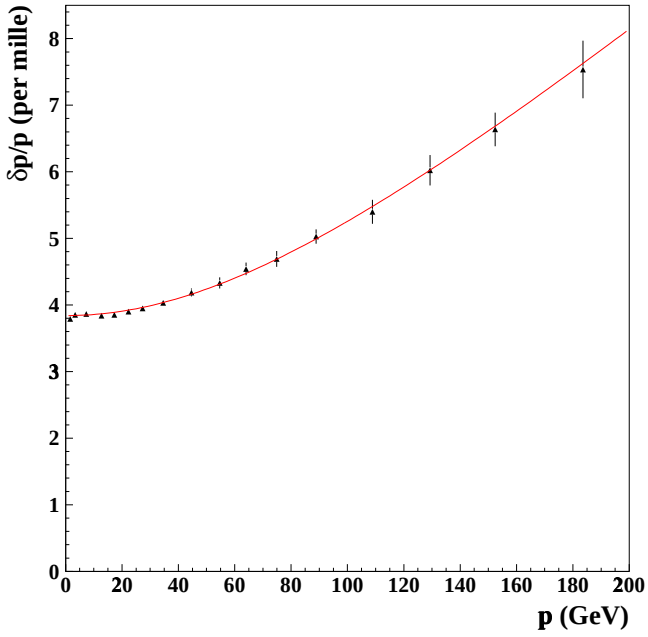

Figure 4.8: Momentum resolution $\delta p/p$ as a function of track momentum.

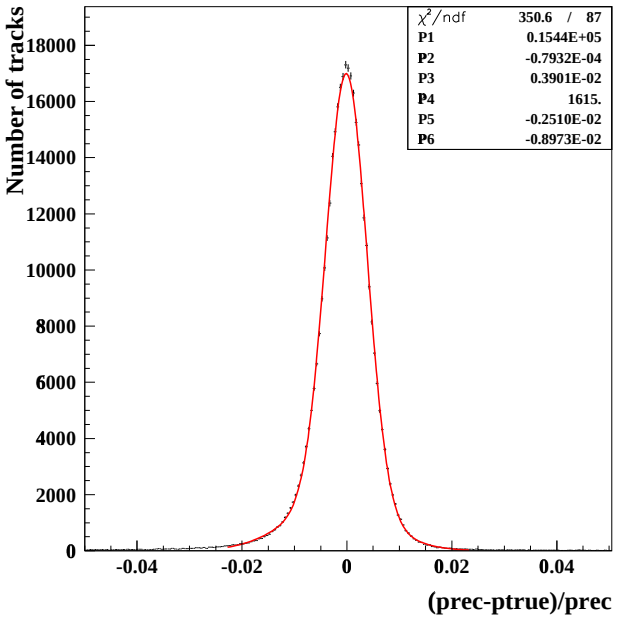

Figure 4.9: Momentum resolution distribution for all tracks above 1 GeV/c. The average resolution is $\delta p/p = 0.39$ %.

4.3.2 Pattern recognition

Two regions in the LHCb spectrometer are used for track finding: the vertex region and the downstream region of low magnetic field. Track seeds found in the downstream region are followed in opposite direction through the magnet to be linked with tracks segments found in the vertex detector. This procedure, referred to as upstream tracking, is attractive for two reasons:

- For a good first extrapolation of the trajectory into the magnetic field, an initial momentum estimate of the track is needed. By assuming that a track seed originates

from the vertex region, the p_t-kick of the magnet provides a momentum resolution of 2%.

- The magnetic field at the downstream side of the magnet has a long tail of moderate field value. Stations placed in this field tail see a slowly increasing track curvature, which results in an improvement of the momentum estimate from station to station, while at the same time an error on the momentum estimate only leads to a small deviation of the projected trajectory from the true one.

These advantages are not enjoyed by a track following method that starts at the vertex detector and proceeds in the downstream direction.

Track seeding

In order to have robust track seeding, four stations (T6 – T9) are placed in the low field region between $z \simeq 8$ m and $z \simeq 9.5$ m. A minimum of three stations is strictly required to find a curving track. The fourth station is added for redundancy in case of inefficiency. Hits in the stations T6 – T9 are combined in a pattern recognition algorithm for track seeding [44]. The algorithm first combines x-coordinate measurements to form local track vectors ("stubs") in each of the seeding stations. A two-dimensional trajectory in the x-z plane is obtained by linking these stubs with a parabolic track fit, which takes into account the presence of a small magnetic field. Adding combinations of hits in the stereo planes finally results in 3-d track seeds.

Defining a track seed to be efficiently found if more than 70 % of the associated hits are correctly assigned, the average efficiency for tracks originating from the vertex area and traversing the seeding region is 95 %. The seeding efficiency as a function of track momentum is plotted in figure 4.10.

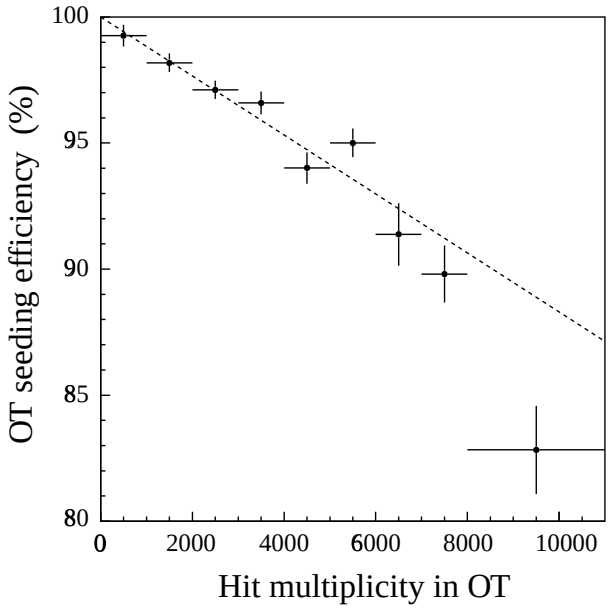

Figure 4.11: Track seeding efficiency versus the total number of Outer Tracker hits in stations T6 – T9.

In figure 4.11 the efficiency of track seeding is plotted as function of the total number of Outer Tracker hits in stations T6 – T9. For the lower multiplicity events the efficiency falls linear with the number of hits. The efficiency drops significantly when more then 8000 hits are present.

Track following

The reconstructed track seeds are used as an input to the Kalman procedure of following tracks in the upstream direction through the magnetic field. In this procedure track parameters are determined recursively as track continuations are found at each station. At each station the track parameters are updated, which is equivalent to re-fitting of the track from station T9 up to the current station. Using the updated track state vector, a prediction into the subsequent station is made by a Runge Kutta trajectory extrapolation across the magnetic field.

The track prediction in a station is used to open up a search window for candidate track continuations. At each station maximally 10 possi-

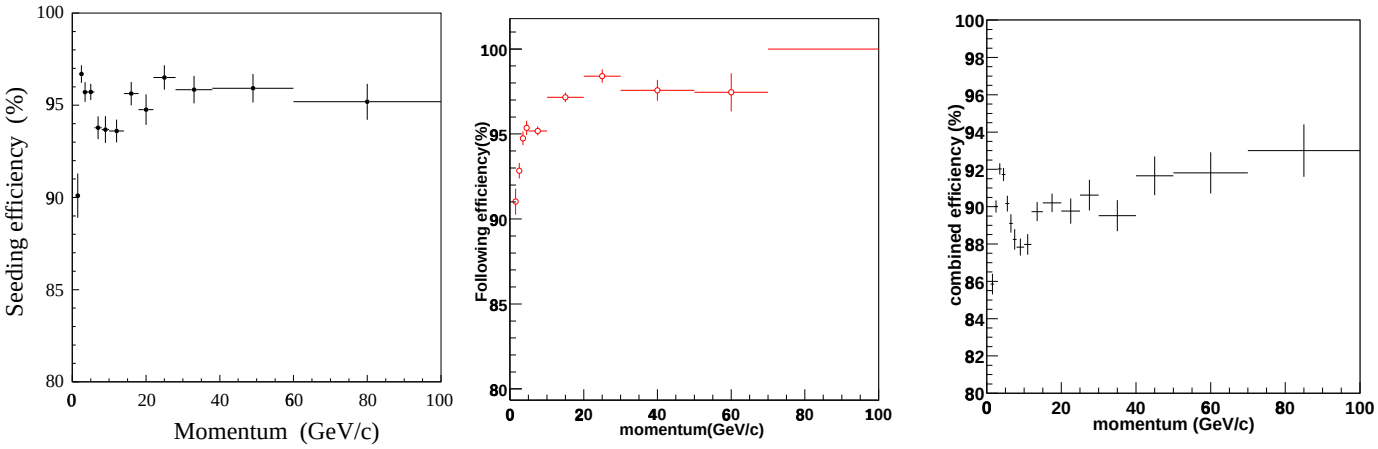

Figure 4.10: Pattern recognition efficiencies as a function of momentum. Left: track seeding. Middle: track following. Right: combined seeding and following.

ble track continuations are allowed. All these branches are followed while a quality criterion is assigned to each track, based on the total number of hits on the track and on the total χ^2 contribution of the hits in the track fit. The quality criterion is applied in order to accept continuations of good quality only, thus reducing the ghost rate to very low values. The efficiency of the track following algorithm versus track momentum is plotted in fig 4.10. The average track following efficiency is 95 %. An extensive description of the track following procedure can be found in [45].

The third plot in fig 4.10 gives the final track reconstruction efficiency in the main tracker after the combined operations of seeding and following [46]. The average track reconstruction efficiency is 90%.

Matching with vertex tracks

The efficiency of combining tracks in the main tracker with track segments found in the VELO has been separately studied [39]. Track extrapolations of the main tracker are matched to the straight tracks in the vertex detector. Not including the inefficiency in the individual track searches, the matching procedure has an efficiency of 99 %.

4.4 Track slopes in the RICH detectors

Reconstruction of the Cherenkov angle from photon hits recorded in the RICH detectors requires a measurement of the charged track direction, which defines the centre of the photon ring. The tracking detector arrangement presented in the Technical Proposal included a station downstream of RICH 2 and planes for y-coordinate measurement in all tracking stations immediately before and after the two RICH detectors. The need for these dedicated detector planes and for a tracking station downstream of RICH 2 was investigated in a combined study of track reconstruction and particle identification [3]. The intrinsic single photon angular precisions of RICH 1 and RICH 2 are 1.45 mrad and 0.58 mrad respectively, indicating that the requirement on track angular precision is more stringent in RICH 2 than in RICH 1.

RICH 1

Without the planes for y-coordinate measurement in T1 and T2, the angular resolution of track segments in RICH 1 degrades from 0.3 mrad to 0.4 mrad. The effect on the particle identification performance was found to be

negligible (see figure 4.12). Based on this result, the dedicated planes in T1 and T2 were removed from the tracker layout.

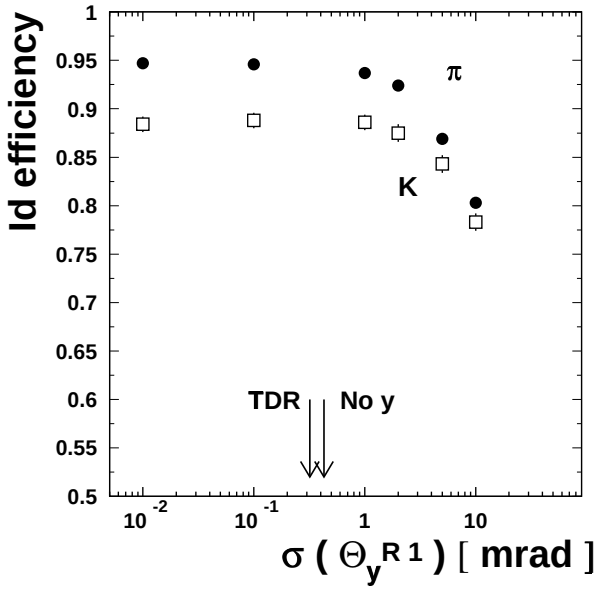

Figure 4.12: Variation of pion and kaon identification efficiencies with angular tracking precision in RICH 1.

RICH 2

In a similar study, the need for a tracking station behind RICH 2 (called "T11" in the Technical Proposal) was evaluated. The momentum dependence of the track angle precision can be described with the following parametrisation:

$$\sigma^2 = \left(\frac{c_1}{p}\right)^2 + c_2^2$$

The values of the constants c_1 (multiple scattering term) and c_2 (term due to track measurement error) are listed in table 4.2, with and without a tracking station behind RICH 2. For example, a track of momentum 70 GeV/c will have an error at the mid-point of RICH 2 of 0.07 mrad (0.10 mrad) when reconstructed with (without) measurements from a backing station.

Comparing these numbers to the resolution of the Cherenkov ring (0.58 mrad per photon for

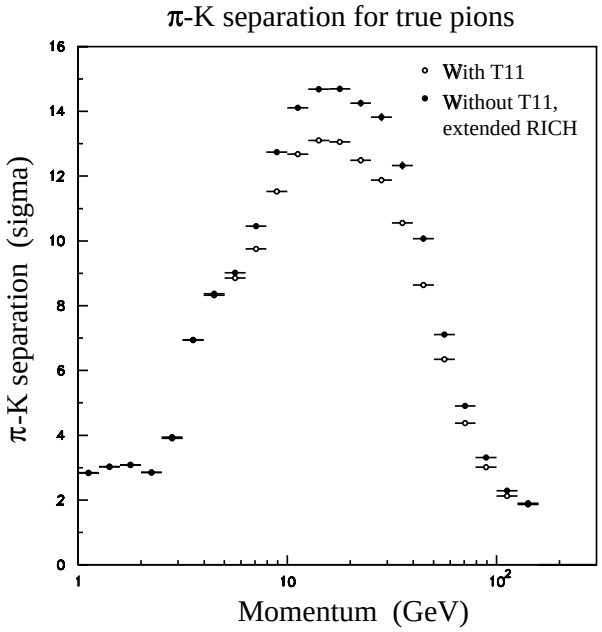

Figure 4.13: Separation between pion and kaon hypotheses for true pions as a function of momentum, with and without station "T11".

	with T11	without T11
$c_1(x)$ [mrad GeV]	1.53	1.46
$c_1(y)$ [mrad GeV]	1.87	2.22
$c_2(x)$ [mrad]	0.042	0.062
$c_2(y)$ [mrad]	0.048	0.068

Table 4.2: Parameters of track angle precision at the entrance of RICH 2, with and without the benefit of a backing station "T11".

$\approx$ 19 photons per ring) the loss in performance without "T11" is small. The loss in particle separation power is in fact fully recovered by extending RICH 2 by 33 cm into the region liberated by the tracking station, which provides a gain of 18 % percent in photon yield. This is illustrated in fig 4.13.

In a second step, the need for y-coordinate measurement planes in station T9 in front of RICH 2 was reconsidered. In table 4.3 the angular resolution of reconstructed tracks at the entrance of the RICH 2 detector is compared for four different cases. The reference geometry corresponds to the situation where planes

stereo angle	angular resolution (μrad)
5^o	94.6 ± 2.7
7.5^o	85.5 ± 2.4
10^o	82.3 ± 2.4
reference	75.8 ± 2.1

Table 4.3: Angular resolution of track segments at the entrance of the RICH 2 detector for different arrangements of tracking planes in stations T6-T9.

for y-coordinate measurement are present in T9 and where the U and V planes of the stations T6 – T9 are under an angle of 5^o. In the other cases there are no y-planes and the stereo angle in T6 – T9 is varied. There is no large difference between the reference geometry and the case where the y-planes have been omitted while the stereo angle has been increased to 10^o. Moreover, it has been shown [3] that $\pi - K$ separation in RICH 2 is not significantly affected if the stereo angle is reduced to 5^o. In spite of the degradation in track angular resolution with respect to the reference geometry, the error on track direction is still small compared to the single photon resolution of 0.58 mrad.

On the basis of the RICH performance study it was decided to remove station "T11" and the planes for y-coordinate measurement in T9.

4.5 Choice of stereo angles

Since the main component of the magnetic field is vertical, the coordinate of interest for momentum measurement is the x-coordinate. Each station contains two measurement planes providing (x, z) coordinates of tracks. In order to reduce combinatorics of possible track candidates, a station additionally contains two planes with drift cells under small stereo angles. The efficiency of the pattern recognition algorithms for track seeding and track following were studied as function of the value of the stereo angle. The efficiency for seeding has a flat maximum between 2.5^o and 7.5^o, while the track following studies slightly prefer angles somewhat smaller than 5^o, see figure 4.14. The processing time for track seeding increases significantly for stereo angles larger then 10^o due to combinatorics..

Taking also into account the studies of RICH performance as summarised in the previous section, the stereo planes were chosen to be at $+5^o$ and -5^o with respect to the x-measurement planes.

4.6 Tracking at trigger level 2

The level-2 trigger algorithm adds momentum information to the tracks used in the level-1 vertex algorithm, in order to recognise fake secondary vertices. The momentum information is obtained from fast tracking, for which two studies have been done: downstream tracking and magnet matching.

4.6.1 Downstream tracking

In downstream tracking, track segments found in the vertex region are extrapolated up to station T4 in the magnet. Assuming the track to be either of high (20 GeV/c) or low (5 GeV/c) momentum the VELO tracks are extrapolated to station T3. By including the measurements of station T3 a rough momentum measurement is obtained, enough to follow the track into station T4. Adding the measurements in station T4 finally gives a momentum resolution of $\delta p/p \approx 0.6\%$. The exact positioning of station T3 in the magnetic field is important: not too far in order to find the extrapolations, but far enough to gain some momentum measurement.

The efficiency for downstream tracking is defined as the number of tracks in the LHCb acceptance that are successfully followed from the

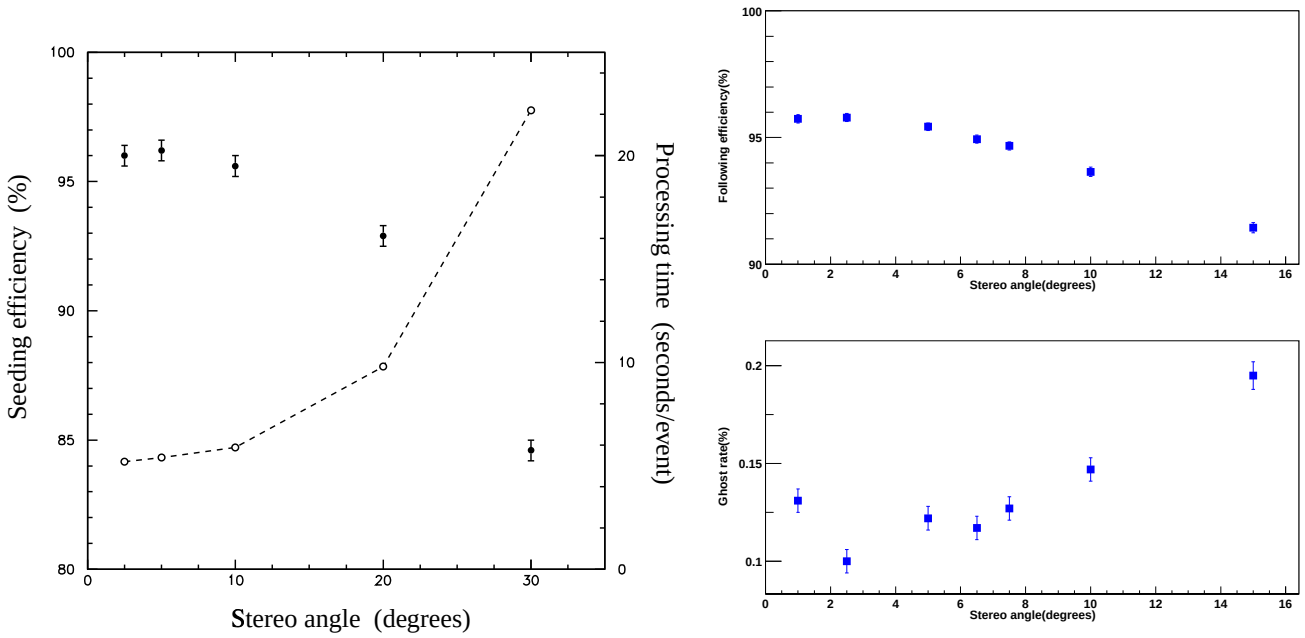

Figure 4.14: Track seeding efficiency (left, solid circles) and algorithm processing time (left, open circles), track following efficiency (top right) and ghost rates in track following (bottom right) as functions of the stereo angle.

vertex up to station T4. This efficiency is plotted as function of the track momentum in figure 4.15. The figure shows the efficiency in two cases: a dedicated search for high momentum tracks and a dedicated search for tracks of moderate momentum. The average efficiency for tracks with momenta between 5 GeV/c and 20 GeV/c is 80 %, while tracks above 20 GeV/c can be found with 90 % efficiency.

4.6.2 Magnet matching

Track segments of the seeding region (T6 – T9) can be directly matched to vertex tracks. This method [47] uses straight line extrapolations of both the seeding tracks and the vertex tracks to the plane at the centre of the magnet. The "kink" between the straight line extrapolations is a measure for the p_t-kick in the magnetic field. From the size of the kink the momentum is obtained with a precision $\delta p/p = 1.3\%$ (see figure 4.16).

The matching method relies on the assumption that a dedicated fast search for high momentum track seeds is feasible at trigger level-2. Calculating the efficiency for the matching procedure for all tracks with momenta above a threshold momentum p_{thresh} as function of the threshold p_{thresh}, the results in fig 4.16 are obtained. For example, seed tracks with momenta above 5 GeV/c can be matched to vertex tracks with an efficiency of 92 %.

4.7 Physics Performance

We haven tested the physics performance of the tracking system with two benchmark B-decays: the two-particle decay $B_d \longrightarrow \pi^+\pi^-$ and the four-particle decay $B_s \longrightarrow D_s^{\mp}(KK\pi)K^{\pm}$.

The reconstruction of B-decays is done using LHCb standard algorithms implemented in the AXSELECT analysis package [48].

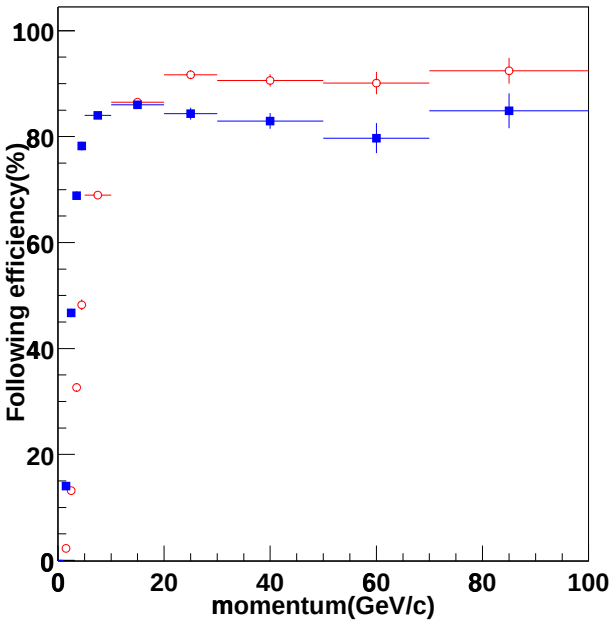

Figure 4.15: Efficiency of downstream track following as function of momentum, with the algorithm optimised for momenta around 5 – 10 GeV/c (black squares) and above 20 GeV/c (open circles).

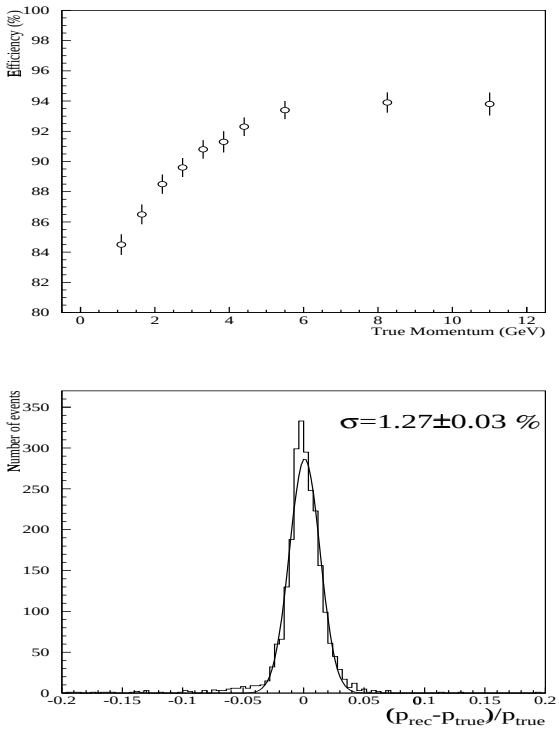

Figure 4.16: Magnet matching. Top: integrated efficiency of matching track segments of the vertex and seeding regions for all tracks with momenta above the specified momentum. Bottom: momentum resolution for the matched tracks.

4.7.1 Reconstruction efficiency

We define the efficiency related to track reconstruction, $\varepsilon_{\text{tracking}}$, as the actual number of reconstructed B events divided by the number that would be obtained if the pattern recognition were fully efficient for all tracks within the LHCb acceptance. In the pattern recognition procedure we apply the individual steps of track seeding and track following, while we assume full efficiency for finding track continuations in the vertex detector.

The efficiencies obtained [46] are: $\varepsilon_{\text{tracking}} = (94\pm2)\%$ for $B_d \to \pi^+\pi^-$ and $\varepsilon_{\text{tracking}} = (79\pm 4)\%$ for $B_s \to D_s^{\mp}K^{\pm}$.

The efficiency for the individual B decay tracks is $(97\pm1)\%$ (for $B_d \to \pi\pi$) and $(95\pm1)\%$ (for $B_s \to D_sK$). These numbers are higher than the average track efficiency of 90% quoted in section 4.3.2, due to the fact that the momenta as well as transverse momenta of B decay particles are significantly higher than those of tracks from the underlying event.

4.7.2 Momentum and mass resolution

The invariant mass resolutions of decaying particles depend on the resolution of the momentum measurements of the individual tracks and on the angular resolution of tracks at the decay vertex. Track angles are mainly determined by the vertex detector, momenta by the main tracker.

Precise mass measurements in $B_d \to \pi^+\pi^-$

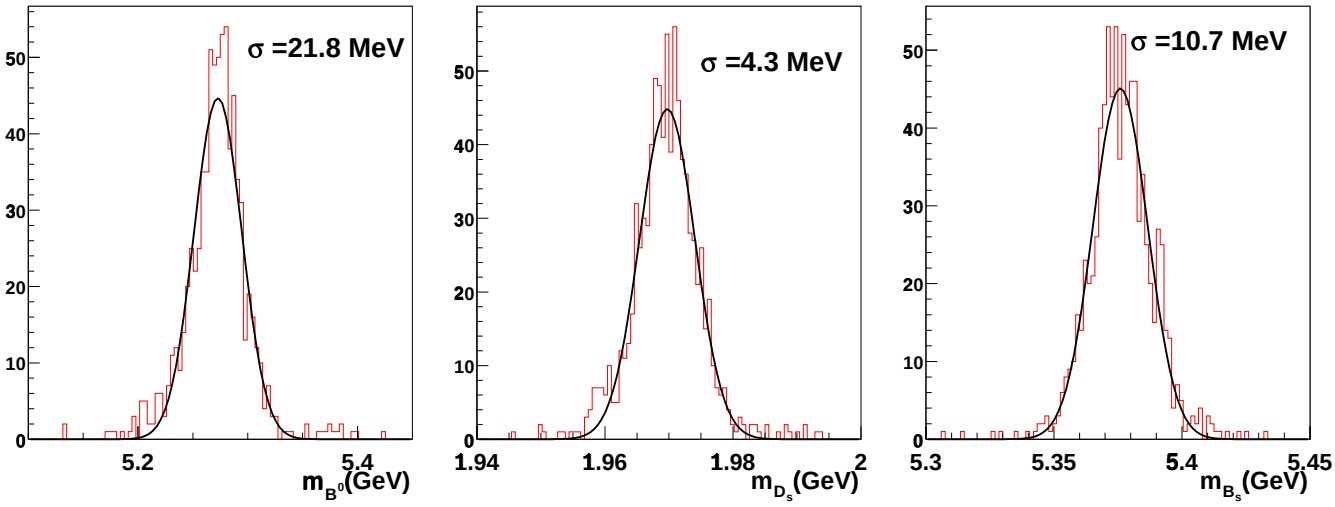

Figure 4.17: Reconstructed mass distribution for (from left to right) $B \rightarrow \pi\pi$, $D_s \rightarrow KK\pi$ and $B_s \rightarrow D_s K$ decays.

and $B_s \rightarrow D_s K$ are important for suppression of combinatoric backgrounds. The mass resolution obtained in the simulation study of the $B_d \rightarrow \pi^+\pi^-$ decay is 22 MeV/c^2. For the decay $B_s \rightarrow D_s K$ a mass resolution of 11 MeV/c^2 was found. Figure 4.17 in addition displays the mass resolution for reconstructed $D_s \rightarrow KK\pi$ decays.

σ (MeV/c^2)	$B_d \rightarrow \pi\pi$	$D_s \rightarrow KK\pi$
full reconstruction	21.8	4.3
perfect momentum	4.3	3.0
perfect angle	21.4	3.1

Table 4.4: Comparing the mass resolution for reconstructed $B_d \rightarrow \pi\pi$ and $D_s \rightarrow KK\pi$ decays with the hypothetical cases of perfect momentum reconstruction and perfect track angle reconstruction of the final state particles.

The effect of the momentum measurement on mass resolutions was studied for $B_d \rightarrow \pi^+\pi^-$ and $D_s^- \rightarrow K^-K^+\pi^-$ decays. If one assumes the momenta of the final state particles to be known exactly, the mass resolution improves from 21.8 MeV/c^2 to 4.3 MeV/c^2 in the case of $B \rightarrow \pi\pi$, demonstrating that the track momentum resolution is limiting the mass reconstruction. In the case of the $D_s \rightarrow KK\pi$ decay, the resolution improves from 4.3 MeV/c^2 to 3.0 MeV/c^2, implying a balanced contribution of momentum and track angle measurements. In table 4.4 the mass resolutions obtained with realistic and ideal reconstructions are summarised.

5 Technical design

5.1 Straw tube modules

5.1.1 Module description

A module contains two staggered layers of straw tubes inside a gas tight box. Each module is a stand-alone detector unit, served by its own branches of the drift gas and high voltage systems. Modules of standard width contain 64 straw tubes per layer. Modules with 32 tubes per layer occur above and below the Inner Tracker acceptance area (see figure 5.19) and at the left and right border regions of some of the stations in the magnet region (see figure 5.18). Behind the magnet, there is sufficient space for extending the horizontal span of stations beyond the nominal acceptance to allow the use of modules of standard width at the left and right borders. (Tubes outside the acceptance will only be read out in as far as they share the electronics modularity of 32 channels per layer with tubes inside the acceptance.)

A module box consists of two sandwich panels, two end pieces and two lateral strips that join the panels along the length of the module. Fig. 5.1 shows the module cross section. The sandwich panels have a 10 mm thick core of honeycomb material (Nomex, density 23 kg/m^3) and 0.1 mm thick carbon fibre facings. The lateral strips are made of 0.5 mm thick carbon fibre or glass fibre epoxy. Modules have a standard width of 340 mm and will be mounted in station frames at a module pitch of 341.25 mm. The boundary region between adjacent modules is detailed in figure 5.2. The inactive surface at the boundary has a width of exactly one straw tube per layer. Simulation studies show that this loss is inconsequential for track reconstruction efficiency. Therefore, more elaborate designs for tighter lateral joining or overlapping of modules have been discarded.

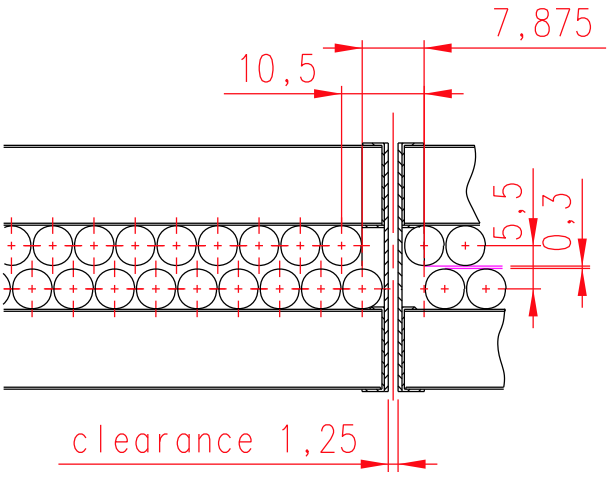

Figure 5.2: Border region of a module.

The gold-tungsten anode wires have a diameter of 25 μm. In order to avoid wire etching[7] due to reactions with radicals from CF_4 decomposition, the wire must be of high quality, free of pores and cracks in the gold layer. Straw tubes consist of two layers of windings. The material[8] of the inner winding is a polyimide film of 40 μm thickness with a 25 % volume doping of carbon. We use 25 μm aluminium foil as outer winding [9]. As illustrated in figure 5.3, the windings of a single layer almost touch but do not overlap in order to avoid uneven stresses in the film material, which would tend to produce shape undulations along the length of the tube. The windings of the inner and outer layers are staggered with respect to each other (out of phase by half a cycle). The two layers are glued together with approximately 10 μm thickness of polyester adhesive. Since the windings of the inner layer do not overlap, there remains a nar-

[7] HERA-B has reported that wire etching in their similar gas mixture is suppressed by maintaining a water concentration of at least 300 ppm in the drift gas.

[8] Manufactured by Du Pont, product designation Kapton XC-160.

[9] Depending on the outcome of winding tests, this may be reduced to 20 μm without affecting electrical properties.

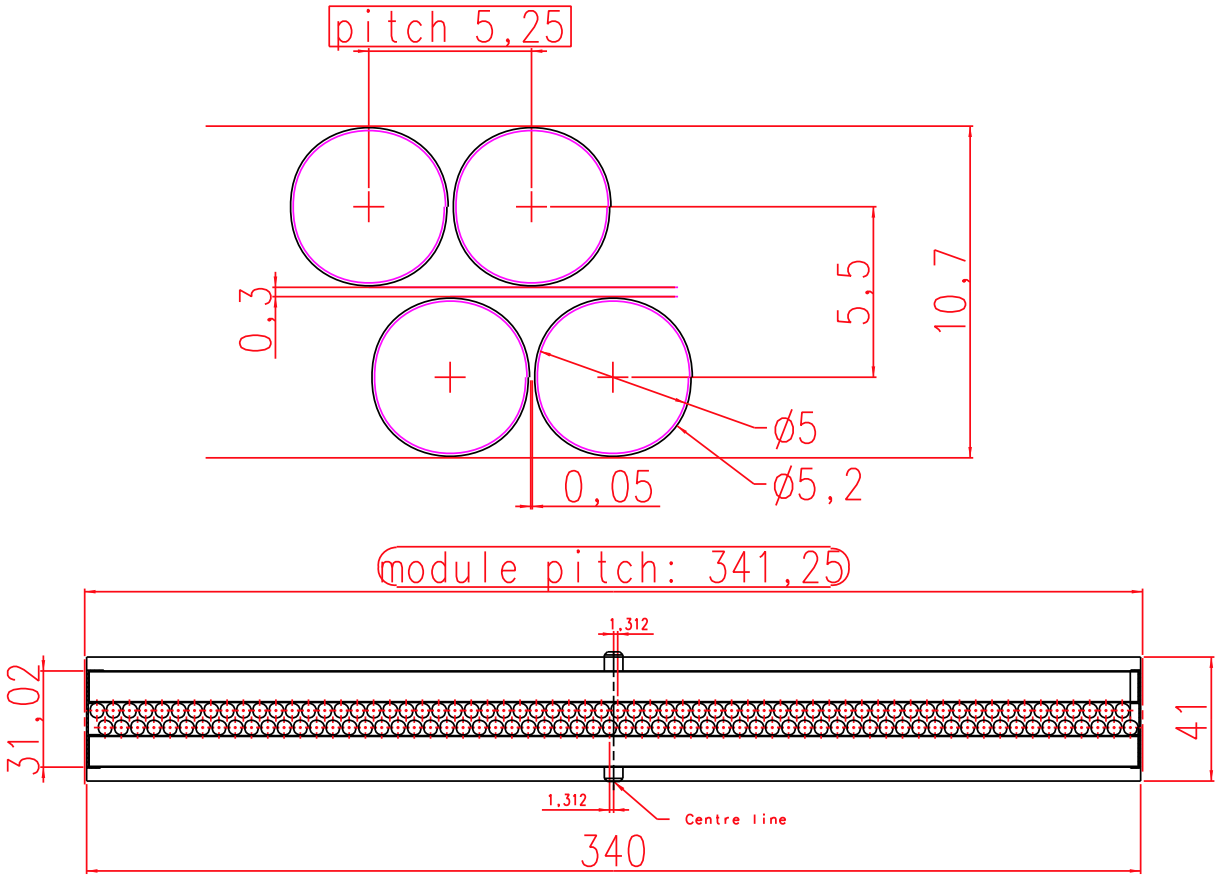

Figure 5.1: Cross section of a straw tube module.

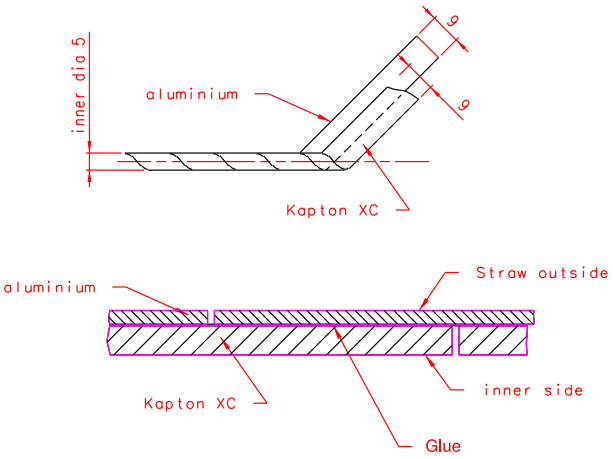

Figure 5.3: Winding pattern of the straw tubes. The two layers are wound from 9 mm wide strips of carbon loaded Kapton and aluminium foil, staggered by half a winding cycle.

row slit (specified to be at most 0.3 mm wide) where the adhesive is exposed towards the tube volume. This is the second reason, next to the primary one of insuring electrical contact between inner and outer winding, for making the adhesive conductive with a 5 % admixture of graphite.

The Kapton XC material of the inner layer has a resistance of about 370 $\Omega/\Box$. The precise resistance of this layer has been shown to be unimportant, as long as it is low enough for proper definition of the electrostatics of the drift cell, i.e. for efficient neutralisation of ion charge. Propagation of the drift signal from the avalanche position to the preamplifier proceeds via the transmission line formed by the anode wire and the highly conductive outer winding of the straw tube.

Aluminium foils of 20 μm thickness cover the inner facings of the sandwich panels. The foils are electrically connected to the ground of the HV distribution boards on the module. The straw tubes are glued onto these foils with Araldite 103, except that at their ends and at intervals of 20 cm along their length strips of conductive glue [10] are used. This procedure effectively 'short circuits' neighbouring straw tubes via the foil. As mentioned in section 3.2, adjacent tubes may otherwise act as elements of a resonating cavity, at frequencies within the bandwidth of the preamplifier.

Modules were initially designed with aluminium foils on the outer facings of the sandwich panels as well. It was proven that their absence has no effect on the mechanical stability of the assembly, nor does it lead to noticeable signal pick-up in one module from an other. Therefore, the external foils were abandoned, in order to reduce the material budget. In case additional shielding will be necessary against pickup from external sources in the actual LHCb environment, it will be provided at station level, not per module.

In early prototyping iterations, straw tubes did not touch the sandwich panels of the module box. They were supported by and positioned in comb structures placed at 50 cm intervals. Given that the straw tubes are in the final design directly mounted on the sandwich panels, it is important that the panels do not bend significantly under the internal gas overpressure. Gas pressure with respect to atmosphere will in no case be above 2 mbar, see section 5.4. Panel deflection has in prototypes been too small to measure reliably. Calculations give a maximum deflection of 70 μm at 2 mbar. Given that anode wires are kept centred in the straw tubes by wire locators placed at 80 cm intervals, a panel deformation of such small amplitude will not affect the operation of the tubes.

Except for the regions above and below the Inner Tracker, modules span the full height of the LHCb acceptance. In order to limit cell occupancies and signal propagation times from avalanche position to preamplifier, full-span modules are electrically split into upper

[10] Tra-con 916D01 or Du Pont 4922 Conductive. Ultrasonic soldering was found to be a viable alternative, but is not preferred because it is labour intensive.

and lower halves. In other words, the electronic channel count is 2 x 64 per layer. The straw tubes and anode wires are split midway along the module length (i.e. near the plane y = 0) with some staggering of the split position among the consecutive module layers of a station. The splitting arrangement is illustrated in figure 5.4. In each of the two layers, a PCB board, 0.8 mm thick and measuring 20 mm in the wire direction, spans the width of the module. It carries soldering pads for the 2 x 64 wires in the layer. After wires have been soldered, covers of glass fibre epoxy (FR4) are glued onto the PCB strips. The covers are shaped in such a way that they join the straw tube sections on either side of the split, in order to ensure proper gas flow through the tubes from one extremity of the module to the other. There is no severe requirement on gas tightness of the splitter arrangement, since the space outside the tubes is being kept under a flow of drift gas as well. Averaged over its length of 20 mm, the material of the wire splitter represents 0.65 % X_0.

The length of dead space at the wire splitter has been kept modest by omitting terminating impedances at the ends of the anode wires. As shown in section 3.2, there is indeed a net advantage to leaving the wire ends electrically open, rather than suppressing signal reflection with a matching impedance. Even in the longest modules, the arrival times at the preamplifier of the direct and reflected signal pulses never differ more than 20 ns, which is within the effective dead time of the ASDBLR preamplifier and thus does not lead to double pulse registration. Superposition of the delayed reflected signal over the direct signal does somewhat increase the ASDBLR dead time per hit, but that is outweighed by the advantage of increased amplitude. This is of most benefit to signals originating near the far end of the anode wire (direct and reflected components are almost in phase) and these are precisely the signals most in need of an amplitude boost (see section 3.2. for a quantitative discussion).

The two extremities of a split-anode module are identical. Not only are the boards for anode wire connection and HV distribution and the front end electronics boards the same, but also the end piece mechanics is identical, although the opposite end pieces have different functions in the path of gas flow. Gas for the 128 tubes of a module enters via a single input line and is distributed into the straw tubes by a manifold that is incorporated in the bottom end piece. Drift gas passes through the wire splitters to the opposite side of the module, where the end piece gathers gas flowing from the straw tubes and sends it to the common output line. Given that the straw tubes can not be guaranteed to be leak tight, it is mandatory that a flow of drift gas is also maintained in the module volume outside the tubes. The gas flow through this buffer volume is maintained by its own input and output lines. The arrangement is schematically shown in figure 5.5. Figure 5.6 shows how the manifold for gas distribution to the tubes was executed in prototypes. Straw tubes fit tightly onto exit holes in the manifold wall. The final design is an elaboration (tubes fit onto protrusions on the manifold wall) of the same principle. The drift gas system is discussed further in section 5.4.

Modules above and below the Inner Tracker have a single, unbroken anode wire. Electrically, such a module is identical to one half of a full-span module. Mechanically and from the point of view of gas flow, it is equivalent to an entire full-span module except for the absence of a wire splitter. For modules mounted above the Inner Tracker it would be simplest to have the gas input and output lines at the top. However, given that the drift gas is heavier than air, filling from the top carries the risk that some air remains trapped there. Therefore, gas input and output will also in these modules take place at the bottom end piece. Connection with the piping of the gas distribution system, located on the station frame, will be made through gas

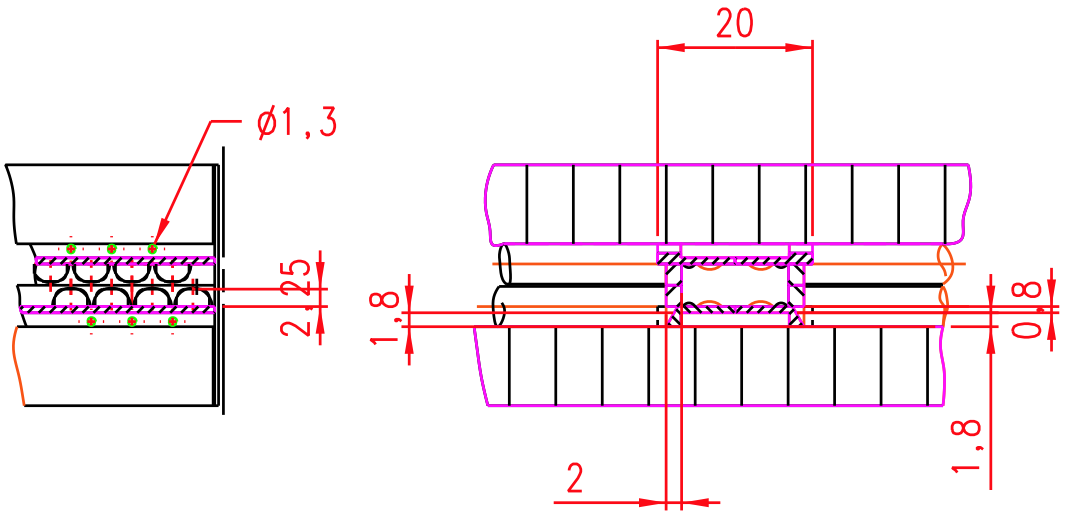

Figure 5.4: Layout of the wire interrupter midway along a module.

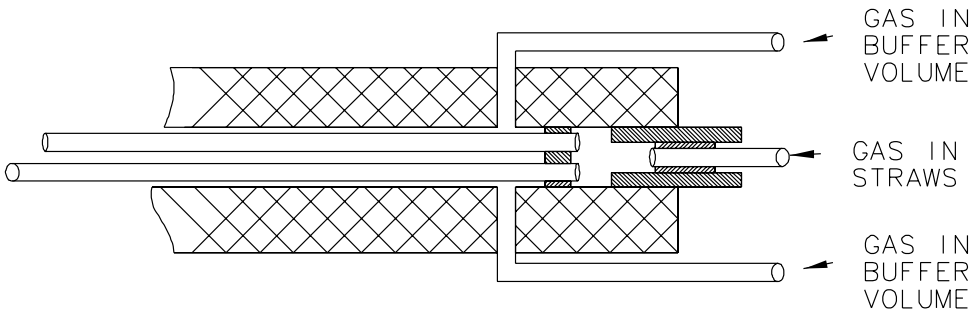

Figure 5.5: Scheme of parallel drift gas flows into the straw tubes and the surrounding buffer volume. Gas enters the straw tubes (shown at the left hand side) through a manifold.

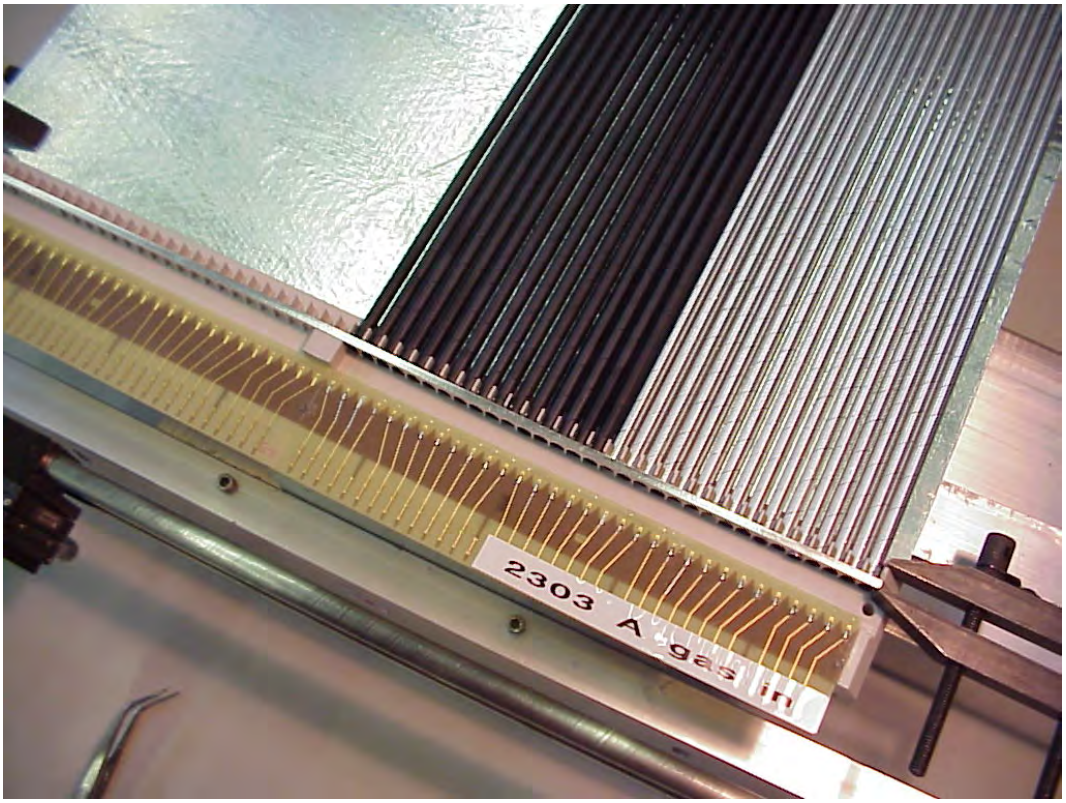

Figure 5.6: Principle of drift gas distribution into straw tubes as implemented in a prototype.

channels inside the sandwich panels of the modules.

Anode wires longer than 1 metre are at intermediary positions supported by so-called wire locators. Typically, these are spaced at intervals of 80 cm. The precise distance necessarily depends on the total wire length to be subdivided and thus varies somewhat from station to station. The largest number of locators per wire section, i.e. between end piece and wire splitter, is two. As an example, their positions are shown in figure 5.7 for the case of station T6. We have experimented with locators of quite different shapes. The final choice, illustrated in figure 5.8, was made on the basis of the following criteria: ease of wire insertion through a series of locators (i.e. time needed for the operation and failure rate), precision of wire centring in the straw tube, minimisation of amount of material and length of the locator, suitability for industrial series production. The chosen design, executed in Noryl N110, is suited for production by injection moulding. The locator essentially consists of two disks at 1 cm spacing from which V-shaped sections have been cut out. The sections have opposite orientations, $\vee$ and $\wedge$. Their overlap leaves an opening of 50 μm diameter for the sense wire. Prototype tests have demonstrated that the 10 mm long piece of locator material introduces an insensitive region that is about 2 mm longer (see section 3.3). Averaged over its length and width, a locator represents 0.45 % X_0.

The chosen interval between wire locators guarantees that the sagitta due to electrostatic forces on a not perfectly centred anode wire remains small. The wires are strung under a tension of 70 g. At the working point of 1550 V for the drift gas mixture $Ar(75)CF_4(15)CO_2(10)$, a wire offset from the straw tube centre of 50 μm at two locators, spaced at 80 cm, leads to a sagitta of 6 μm on top of the 50 μm offset.

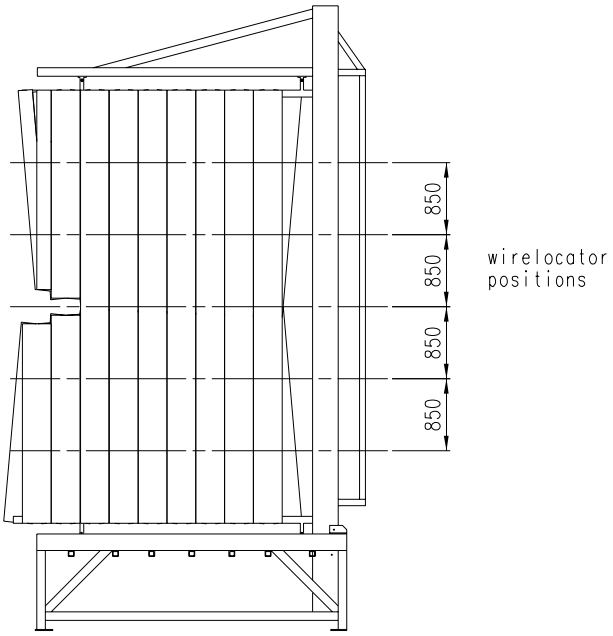

Figure 5.7: Front view of one half of station T6. The horizontal lines indicate the positions of wire splitters (equatorial line) and wire locators.

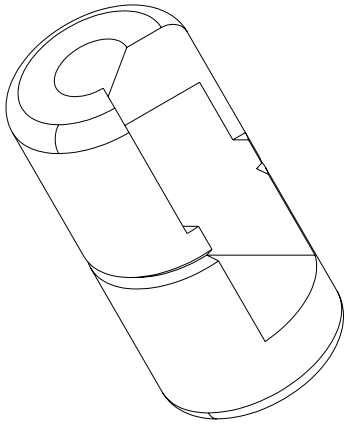

Figure 5.8: Wire locator.

5.1.2 Material budget

The basic material budget of a module corresponds to 0.67 % of a radiation length:

4 x 0.1 mm carbon facing	0.14 %
2 straw tube layers	0.276 %
2 x 10 mm HC core	0.11 %
2 x 20 μm Al foil	0.045 %
gluings	0.1 % (est.)

The breakdown of the value $X/X_0 = 0.276$ % for the straw tube layers is: aluminium outer windings 0.165 %; Kapton XC inner windings 0.091 %; glue 0.02 %. Localised contributions from the lateral strips of the modules and from wire locators and wire splitters must still be added. Expressed as equivalent layers of uniformly distributed material, these two sources respectively contribute 0.07 % and 0.01 %, leading to a sum of 0.75 % X_0 per module. A station with 4 layers of modules thus represents 3.0 % X_0. If it turns out necessary to add pick-up shielding over the upstream and downstream surfaces of a station, this increases to 3.1 – 3.2 %. Summed over all stations, the Outer Tracker material within the LHCb acceptance will thus correspond to 0.24 – 0.26 X_0. Regarding hadronic interactions, the material of Outer Tracker stations T2 – T9 represents 10 % of an interaction length. These numbers do not include material concentrations close to the top and bottom boundaries of the Inner Tracker due to the fact that Outer Tracker modules mounted above and below the Inner Tracker acceptance must be terminated with end pieces. These are essentially equal to one half of a wire interrupter, terminated with an end wall of 0.5 mm FR4 material. From the point of view of material budget they represent 10 mm wide strips of 1.4 % X_0 per module.

The weight of a mechanically complete module of largest length (4.8 metre) is 10 kg. The front end electronics at the two extremities adds 5 kg to the total module weight.

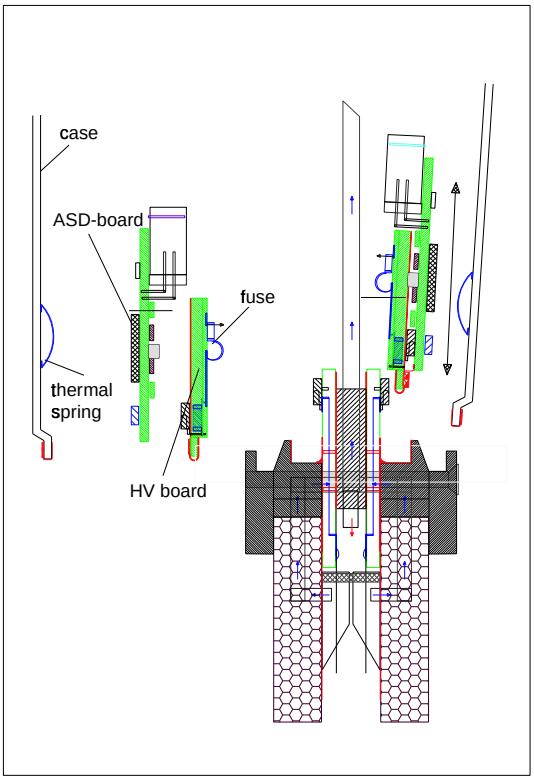

Figure 5.10: Exploded view of the front end boards.

5.1.3 End pieces and front end boards

Arrangements internal to the body of a module (anode wire support, grounding and HV connections, gas manifold) will be identical for all stations. However, due to space constraints, details of front end board mounting and the layout of gas piping and cabling will in the magnet stations be different from stations T6 – T9, where one can afford emphasis on accessibility. The external layout of T2 will essentially follow the magnet station design for practical reasons (same production site).

Figures 5.9 and 5.10 illustrate the end piece layout for the case of stations T6 – T9. The layout for the magnet stations will only differ

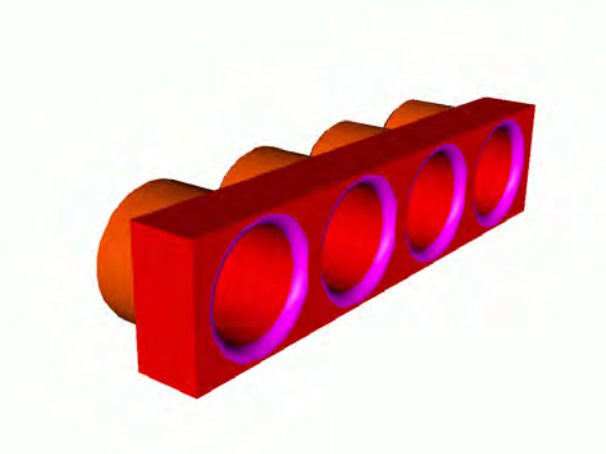

Figure 5.11: Section of the gas distribution block with straw tube sleeves.

in that it adds less to the total module length. The straw tubes fit onto cylindrical protrusions of a gas distribution block made of Ultem, see figure 5.11. Centring of the sense wire ends is assured by wire locators incorporated in the gas distribution block. Each layer of 64 tubes is served by a single HV distribution board. The wires are electrically connected to the HV boards via two PCBs (one for each tube layer) that are part of the mechanical end piece of the module and that carry the wire soldering pads. The connection paths between pads and HV board run within the double layered PCB board. The cathode ground of the tubes is defined via the aluminium foil of the sandwich panel that carries the tubes. The foil extends under the end piece and is over its full width connected to the ground of the HV board. The electrical connection between foil and tubes is made with conductive glue, over a length of several centimetres at the tube ends and additionally at intervals of 20 cm along the tube. Each HV distribution board is fed by a separate branch of the HV system, i.e. the unit of HV modularity is 64 channels. The board contains filter elements, coupling capacitors, protection resistors and fuses. The capacitors are mounted inside the board. The fuses are made of bronze spirals with a protection resistor soldered to that

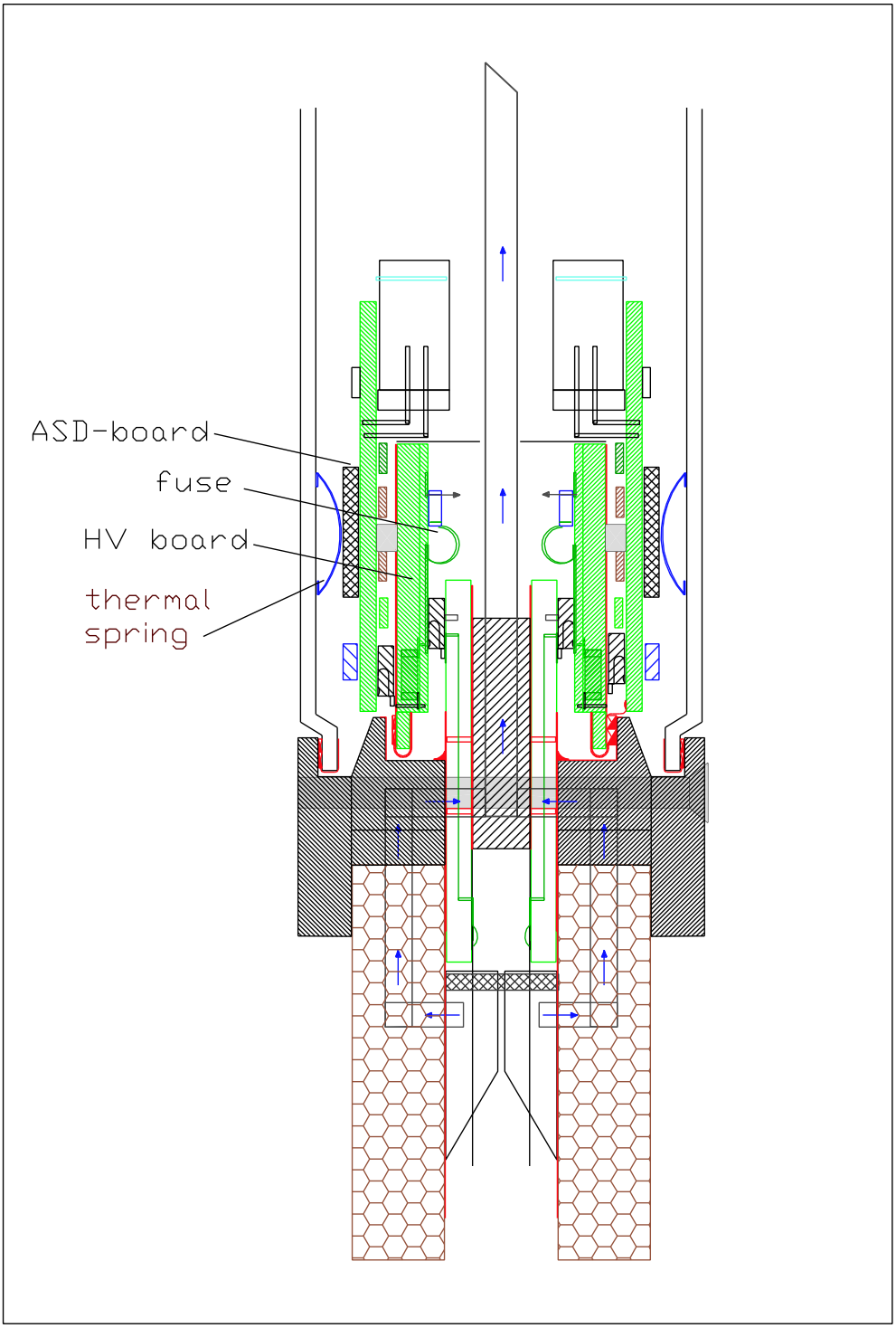

Figure 5.9: Side view of end piece and mounting of front end boards in T6 – T9.

spiral. Resistors are soldered to the board with a solder tin of low melting point. In case of a short, current is drawn by the resistor, the solder tin becomes heated and after a few seconds the connection with the offending straw tube is broken while the other tubes in the module remain operational.

Signals are fed through from the HV boards to front end boards that each carry 4 ASDBLR preamplifier-discriminator chips of 8 channels each, plus one 32-channel OTIS TDC chip. Thus, a module of the standard width of 64 tubes per layer has four front end boards per readout side. The OTIS TDC can safely be placed on the front end board, since it will be produced in radiation hard technology. In case of use of the HPTDC – which is radiation tolerant but not radiation hard – the LVDS outputs of the ASDBLR chips will be transported in groups of 8 towards TDC boards placed away from the detector. Apart from this difference in the front end boards, the arrangement shown in figures 5.9 and 5.10 applies to both cases. The input lines of drift gas at the end piece are shown in figure 5.5. At the opposite end of a module, the same layout serves to collect the gas into the return lines.

5.1.4 Assembly procedure

Wire locators can simply be pushed to their required positions inside a straw tube. The $\vee$-shaped cuts in the locator give it sufficient shape elasticity to be pushed through easily *and* to stay wedged in position without gluing. Straw tubes with inserted wire locators are placed on a template, which consists of an thick aluminium plate machined into a profile that matches a single layer of tubes, see figure 5.12. The lateral definition of the straw tube channels with respect to dowel pin holes in the plate has a precision of 10 μm. The tubes are kept centred inside the template channels by application of an under-pressure through holes

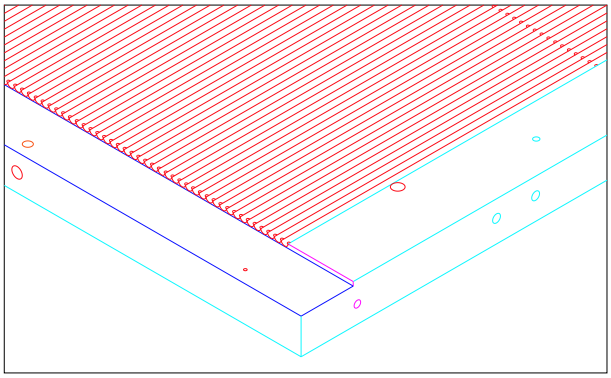

Figure 5.12: Module assembly template.

in the template. A gas distribution manifold is fitted onto the tube ends. A prepared sandwich panel is then placed on top of the array of straw tubes and glued onto the tubes.

Then follows wiring: wires are blown through the wire locators with an air gun or sucked through with an air pump, either method works well. Wires are tensioned with 70 g weights, and soldered and glued onto printed circuit boards — which have also been positioned with respect to the dowel pin holes of the template — at the end pieces and at the wire splitter. During the wiring operation, bending of the assembly of sandwich panel plus straw tube layer is avoided by placing a temporary support panel on top. Two straw tube layers, each carried by a sandwich panel, are then joined face to face; the lateral strips are glued on and closure of the module box is completed by gluing a plug of FR4 material between the PCBs of the two straw tube layers.

Mechanical tolerances are of importance only along the drift coordinate, i.e. along the width of a module. During assembly of a single layer, all positioning of parts can be defined with respect to the dowel pin hole of the assembly template. In prototype modules, wire ends were typically positioned with an r.m.s. spread of 25 μm from nominal with respect to the common fixation reference. In the final design that common reference is the gas manifold block: the

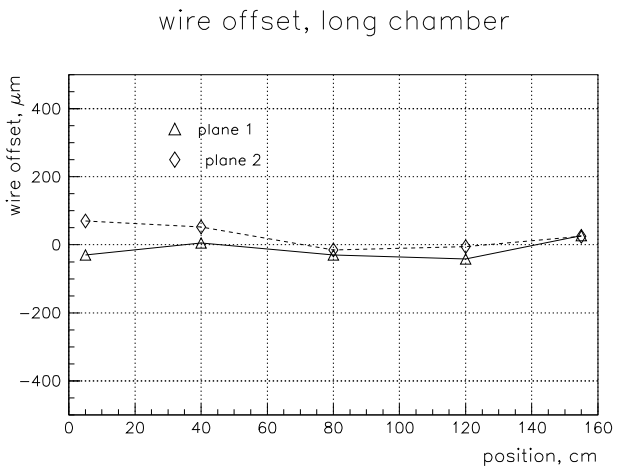

Figure 5.13: Measured wire offsets as a function of position in a 2 × 1.6 m long prototype module.

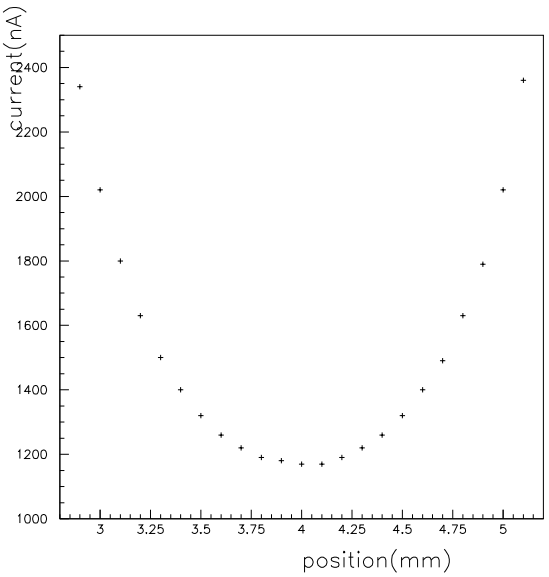

Figure 5.14: Signal current variation with wire offset from the tube centre, which in this plot is at position 4.0 mm

tubes fit onto this block, and inserts within the tube ends position the wires. We expect a similar error on the positioning of the gas block itself with respect to the pin hole. Added in quadrature this leads to a realistically achievable r.m.s. positioning error of individual wire ends of 35 μm. This is equivalent to a mechanical tolerance field of $\pm$ 60 μm, from which number we derive the quality control criterion that each wire end should be within 60 μm of its nominal distance to the reference pin hole. For the absolute wire positioning inside wire locators a comparable precision is estimated: possible offset of the wire hole of the locator from the nominal tube axis and the 50 μm diameter of the hole together lead to an expected tolerance field of $\pm$ 50 – 60 μm. However, this can *not* be checked in any practical way at production time. A layer of straw tubes will as a whole, via the dowel pins which mount the module onto the station frame, have a positioning error of $\pm$ 30 – 40 μm with respect to reference points of station alignment (see section 5.2). In summary, mechanical tolerances are expected to be significantly smaller than the drift coordinate resolution of 0.2 mm per cell. Track analysis will allow to check whether the alignment of wires in different layers within the same station is in accord with the quoted wire positioning accuracies. Figure 5.13 shows wire offsets in a 2 × 1.6 m long prototype module as determined from high-statistics test beam data (wire offset equals the difference between measured drift distance and the predicted value assuming a perfect geometry).

5.1.5 Module acceptance tests

We foresee the following standard tests when a module comes off the assembly line:

- Gas tightness of the module box and flow rate at given driving pressure will be checked.
- Each module will, after conditioning at the HV working point, be tested on operating stability and low dark current.

- With an automated setup, a radioactive source will be moved along the length of the straw tubes and the count rate profile will be recorded. This has been found to be a fast method for localising major errors in the straw tube geometry, such as wrong positioning of wire locators.

The measurement of count rate profiles is not a very sensitive method for the detection of wire offset from the tube centre. As illustrated in figure 5.14, the variation of signal current with wire offset is weak for deviations of the order of the 60 μm tolerance field. Maintenance of tolerances will instead be checked by X-raying every 10th module from each production site. This will be done at one common facility. In addition, randomly selected modules will be tested in a cosmic ray setup.

5.2 Station design

5.2.1 Common principles

The four layers of straw tube modules in a station are mounted on an aluminium frame. There is a spacing of 25 mm between successive module layers in order to obtain sufficient lever arm for a slope measurement of track segments. In the stations placed in the magnet region, this amount of spacing is in fact also necessary for cables and piping. Station thickness in the active region is 199 mm: 4 module layers of 31 mm each, plus 3 intervals of 25 mm free space. Installation around the beam pipe requires that the mounting frame actually consists of two halves (left and right) that can be moved horizontally with respect to the beam pipe, see figure 5.15 for the case of stations T6 – T9. Mounting or dismounting of modules is done while the frame is open, i.e. the two frame sections are loaded with their complement of modules during movement into or out of data taking position. Figure 5.16 shows details of module mounting on a frame. Modules are mounted with dowel pins onto 10 mm thick aluminium precision strips along the top and bottom bars of a half station. The pin hole positions on the mounting strips define the module positioning with respect to alignment reference points on the frame. A mockup for the study of assembly of stations T6 – T9 and of the left-right movement of modules in the station frame is shown in figure 5.17.

Figure 5.17: Mockup for the study of station assembly.

After opening and closing of a station, the positioning of the two halves will not be reproducible to better than a few tenths of a millimetre. Therefore, the alignment monitoring system described in section 5.4 includes lines of sight that provide information on the relative position of the two halves. There is nominally not more dead space between the station halves than between adjacent modules within

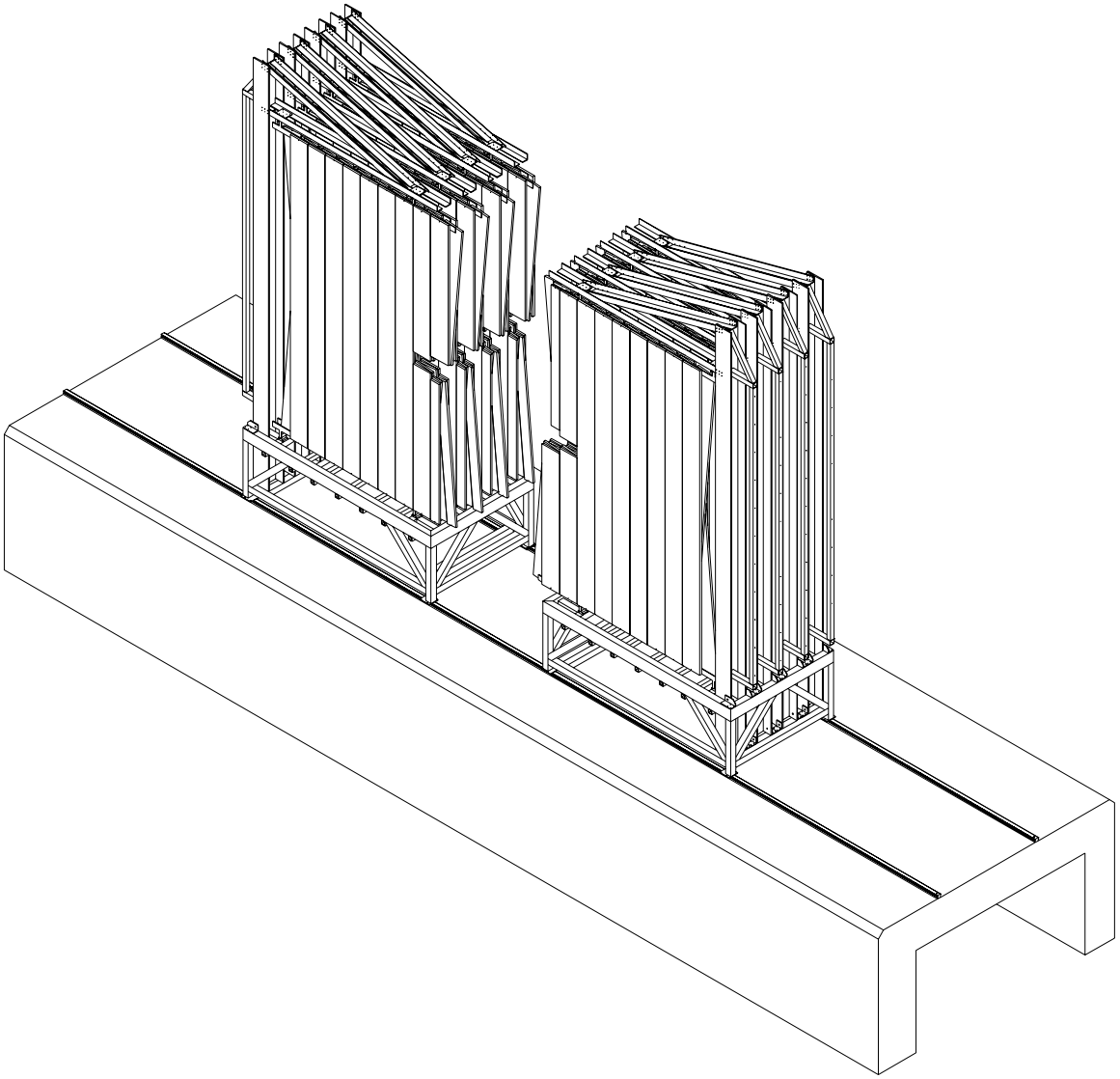

Figure 5.15: Stations T6 – T9 in open position.

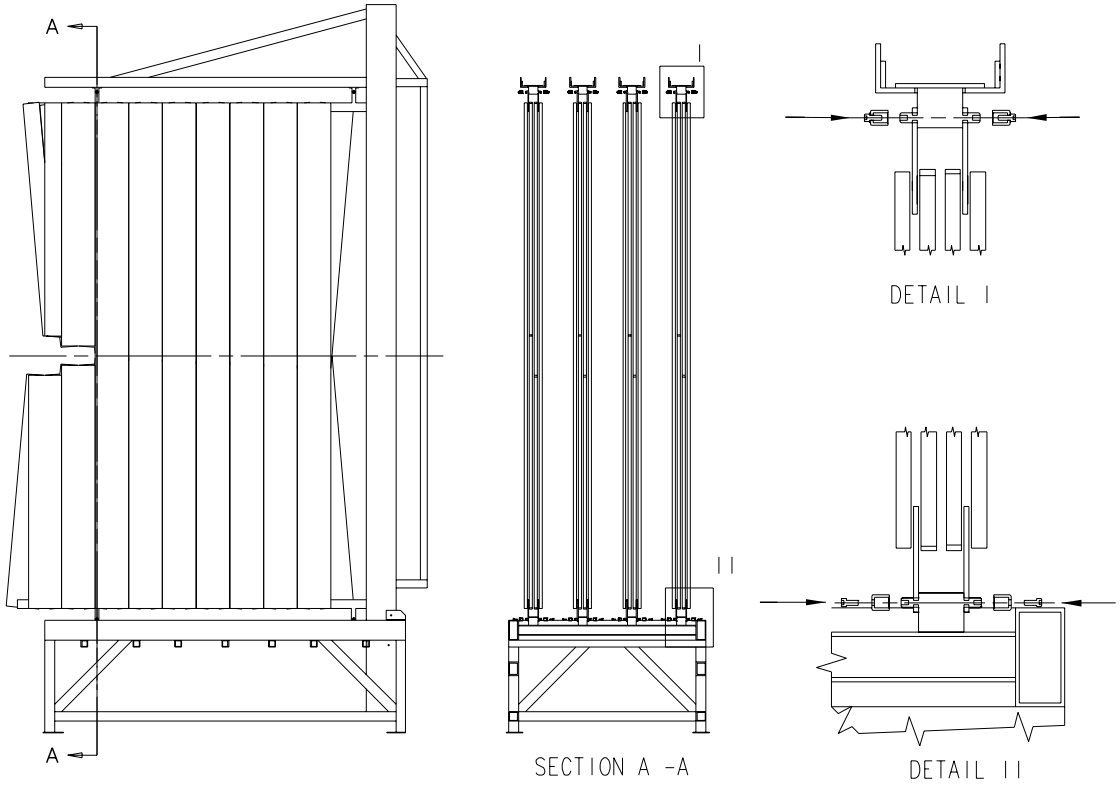

Figure 5.16: Mounting of modules with dowel pins on the top and bottom bars of a station frame. Illustrated is the case of station T6.

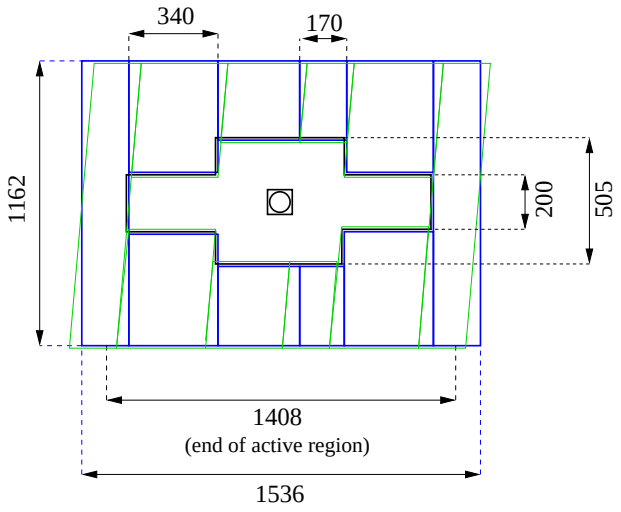

Figure 5.18: Layout of station T2.

one half frame. Therefore, there is no overlap of the left and right halves, with the advantage that they need not be displaced with respect to each other in the beam direction.

While the method of module mounting and the principle of independently movable left – right station halves are common to all stations, specifics of station assembly and installation are necessarily different for T2, T3 – T5 and T6 – T9. The small station T2 will be bolted onto the upstream side of the magnet shielding plate, immediately behind RICH 1. The available space in x and y places no severe restrictions on the layout of front end boards, cabling and piping. Figure 5.18 shows the subdivision of T2 into modules. The stations inside the magnet and the stations in the track seeding region are discussed separately below, starting with the simplest case.

5.2.2 Stations T6 – T9

This rather tightly spaced set of large stations will have a common support structure, see figure 5.15. This solution allows quick and easy retraction of the left and right halves of the assembly to clear the space around the beam pipe, which is necessary whenever the magnet stations must be serviced. The structure essentially exists of two cradles. Movement of the cradles towards and away from the beam pipe will be remotely controllable. Cables and gas pipes will be bundled in cable chains that follow the movement of the cradles. The common support of T6 – T9 provides for a stabler structure than would be the case with thin individual stations of surfaces of the order of 25 m^2.

Figure 5.19 shows the subdivision of a station into modules. The four stations T6 – T9 will have the same size in order to standardise module lengths. The consequence is that the vertical acceptance of T6 – T8 exceeds the nominal LHCb acceptance. The excess length of modules has no significant effect on cell occupancies. In horizontal direction, as many modules of standard width will be mounted next to each other as are necessary to cover the nominal acceptance. The figure illustrates the case of T8 and T9. In T6 and T7, there is one module less on the left and right sides of a plane. The figure shows the subdivision of a plane with vertical modules, but equally applies to the $\pm 5^o$ stereo planes if one imagines each individual module rotated around its geometrical centre. In other words, modules at corresponding positions in the X, U and V planes are in these stations identical. The resulting sawtooth profile along the top and bottom of U and V planes is entirely acceptable, since there are no stringent space limitations. The same sawtooth pattern exists along the boundary with the Inner Tracker, as indicated in figure 5.19. The extent of overlap between Outer and Inner Tracker varies along the width of an Outer Tracker U or V module from nil to $\sin(5^o) \times$ 34 cm = 3.0 cm. The total module surface per plane has in these stations been taken large enough to still cover the corners of the rectangular 300 mrad x 250 mrad acceptance after the 5^o module rotation. Only four different module sizes occur in T6 – T9. All modules to the left and right of the Inner Tracker area are identical. Modules above or below the Inner Tracker come in three types,

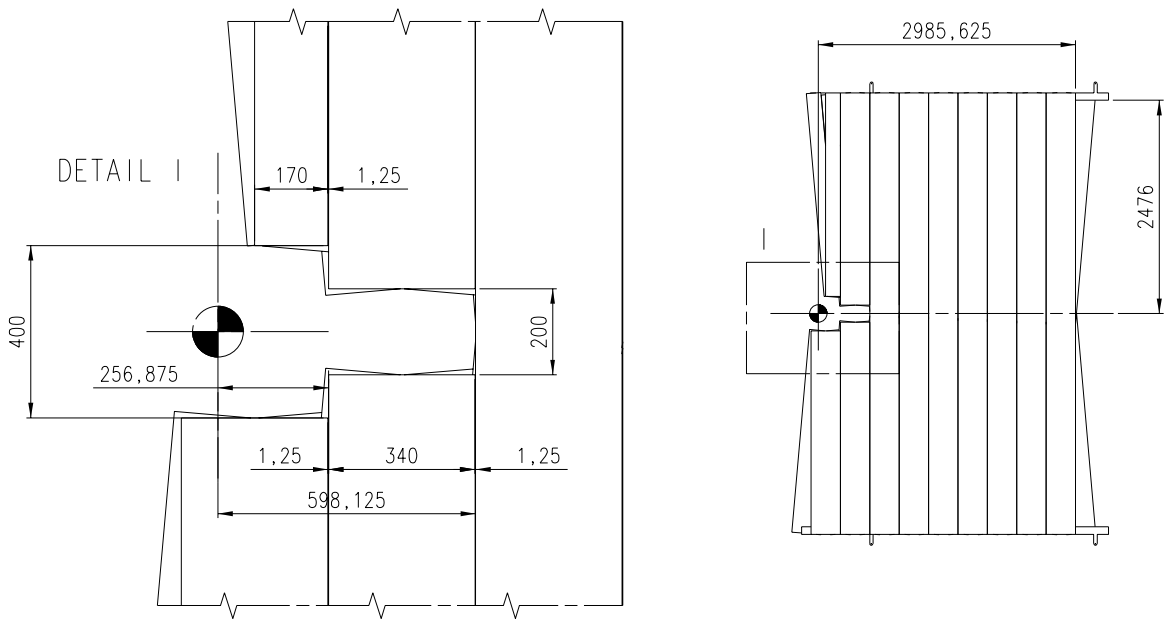

Figure 5.19: Modularity of stations T6 – T9 and detail of the boundary with the Inner Tracker.

two of the standard width of 64 channels but of different length, one of a width of 32 channels.

Cables and piping for drift gas distribution run along the top and bottom of a station frame. The frame also supports the Inner Tracker, via a ladder of carbon fibre rods (see figure 5.20). Given that the Inner Tracker will be displaced in z with respect to the stack of Outer Tracker planes in order to have overlap of the sensitive regions, it is easy to find room for the Inner Tracker supports.

5.2.3 Stations T3 – T5

The magnet layout, described in detail in [49] and illustrated in figure 5.21, places restrictions on the design and installation procedure of stations T3 – T5. The magnet aperture follows the acceptance of the spectrometer, i.e. 300 mrad horizontally and 250 mrad vertically.

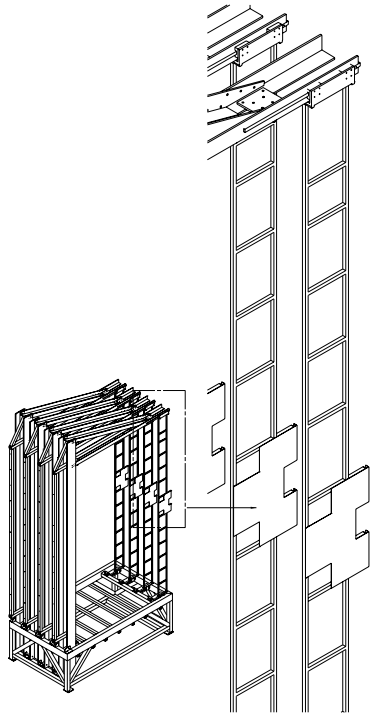

Figure 5.20: Support structure for the Inner Tracker, shown mounted on stations 6 – 9.

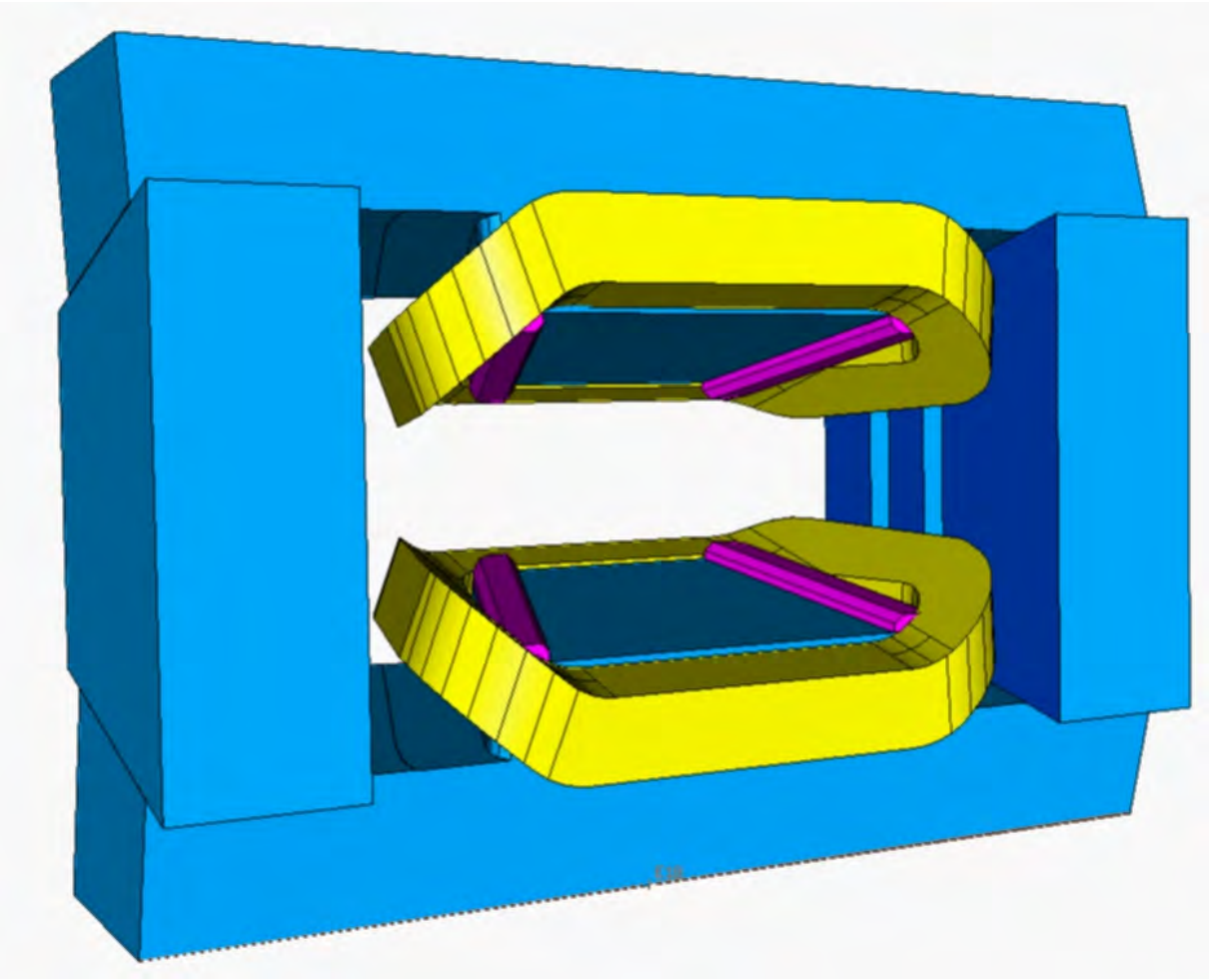

Figure 5.21: View of the LHCb dipole magnet.

In both directions an additional 10 cm has been reserved for mechanical support, front end electronics and services (HV, LV, gas supply, cooling, alignment system) of the tracker stations. Space at the top and the bottom is limited by the iron yoke (T4) and the coils (T3 and T5), at the sides by shims necessary to shape the magnetic field.

The subdivision into modules of station T4 is shown in figure 5.22. Figure 5.23 illustrates the mounting of magnet stations on rails that are bolted onto the iron yoke. Access to the stations is possible by moving them downstream along the rails, out of the magnet. Cables and pipes are guided through cable chains running parallel to the rails. This allows station access without first having to remove pipes and cables. Since the rails follow the 300 mrad acceptance boundary, the left and right halves of a station gradually separate as a station is moved out of the magnet gap. Prior to movement of a station, the Inner Tracker modules must be dismounted. Therefore, the Inner Tracker will in the magnet stations be placed at the downstream side of the Outer Tracker.

Other than in T6 – T9, stereo modules in T3 – T5 must because of space restrictions be truncated to the same outer boundary as the vertically mounted modules, i.e. end pieces and front end boards must be mounted under an angle of 85^o (95^o) to the long module axis. Station T4 is situated inside the yoke. Since the magnet aperture follows the detector acceptance, the gap is narrower at the first plane of T4 than at the last plane. In the horizontal direction this poses no problem, but the vertical acceptance of 2×250 mrad can not be entirely covered by all planes, unless the module length increases from plane to plane (2×5 cm difference between first and last plane). It has been decided to keep module length constant. Loss of acceptance in the last planes can instead be prevented by machining a small step profile into the pole pieces at the location of T4. Calculations have shown that this does not lead to any significant change in the magnetic field map.

Just as in stations T6 – T9, the modules of consecutive planes in a magnet station are connected by means of dowel pins. At the end pieces, the space of 25 mm between detector planes is used as a channel for high and low voltage cables and the cables needed for slow controls. The space will also be used to supply air cooling to the front end electronics. The Inner Tracker detectors are mounted, in the same way as in stations T6–T9, on carbon fibre ladders running parallel to the orientation of the straw tubes. They can be moved horizontally by means of a winder. This is necessary before removing the tracker in order to gain sufficient aperture around the beam pipe while moving the stations downstream.

5.3 Readout electronics

The requirements on the readout electronics are to a large extent determined by hit rates, radiation levels and the LHCb trigger scheme.

Hit rates in the hottest sections of the Outer Tracker will be around 2 MHz per channel at standard LHCb luminosity ($\mathcal{L} = 2\mathrm{x}10^{32} cm^{-2} s^{-1}$) and 4 – 5 MHz at high luminosity ($\mathcal{L} = 5\mathrm{x}10^{32} cm^{-2} s^{-1}$). The annual accumulated radiation dose for electronics located at station edges at standard luminosity is $\leq$12 krad at T2 – T5 and $\leq$5 krad at T6 – T9 [16]. Considerable safety factors must be taken into account when qualifying electronics for on-detector use. According to definitions from the CERN RD49 collaboration, electronics mounted at the outer boundary of Outer Tracker stations must be characterised as radiation tolerant or even radiation hard.

The main components of the Outer Tracker readout system are preamplifier-discriminator chips, time digitisers, and buffers and logic associated with the level-0 (L0) and level-1 (L1)

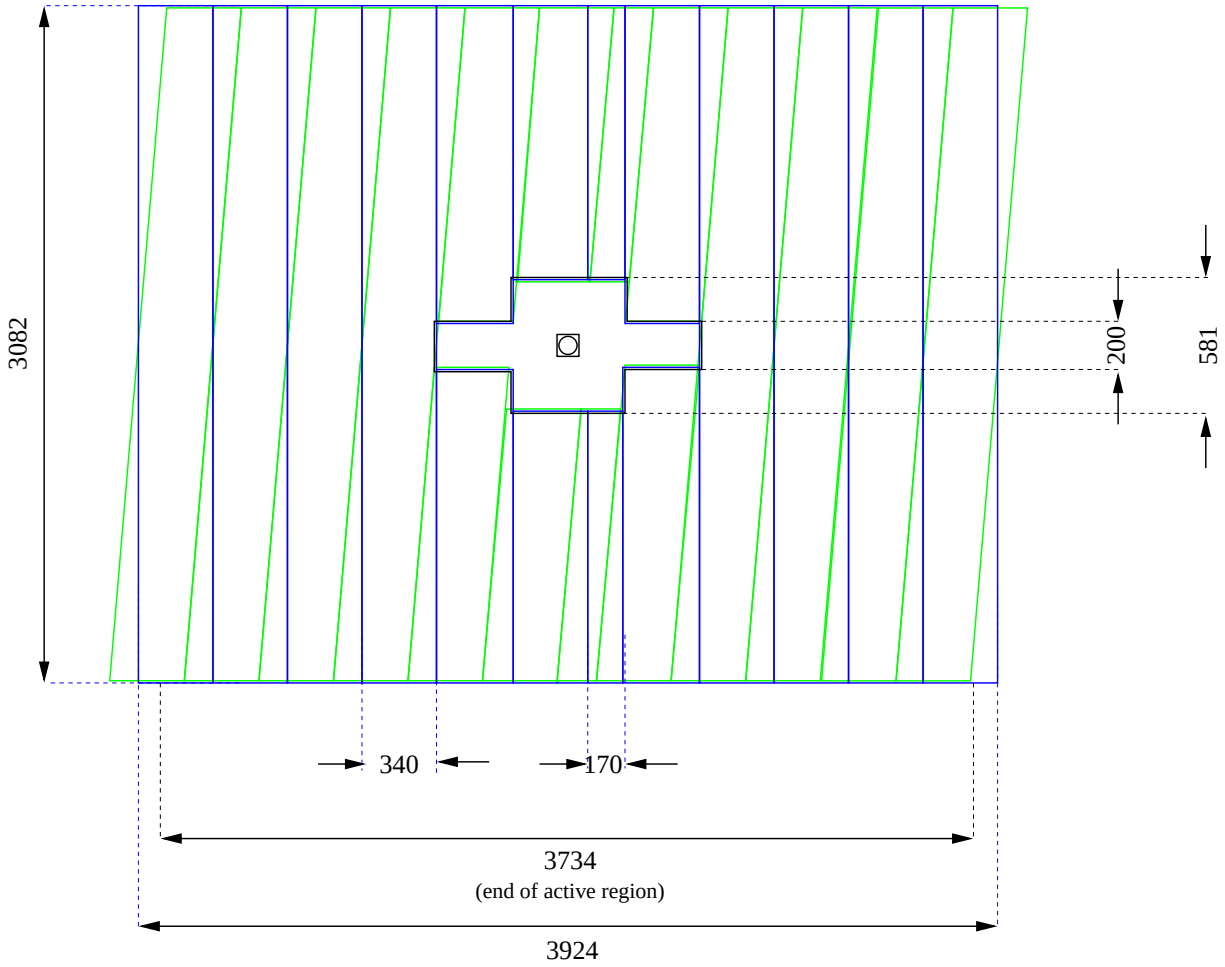

Figure 5.22: Subdivision into modules of station T4.

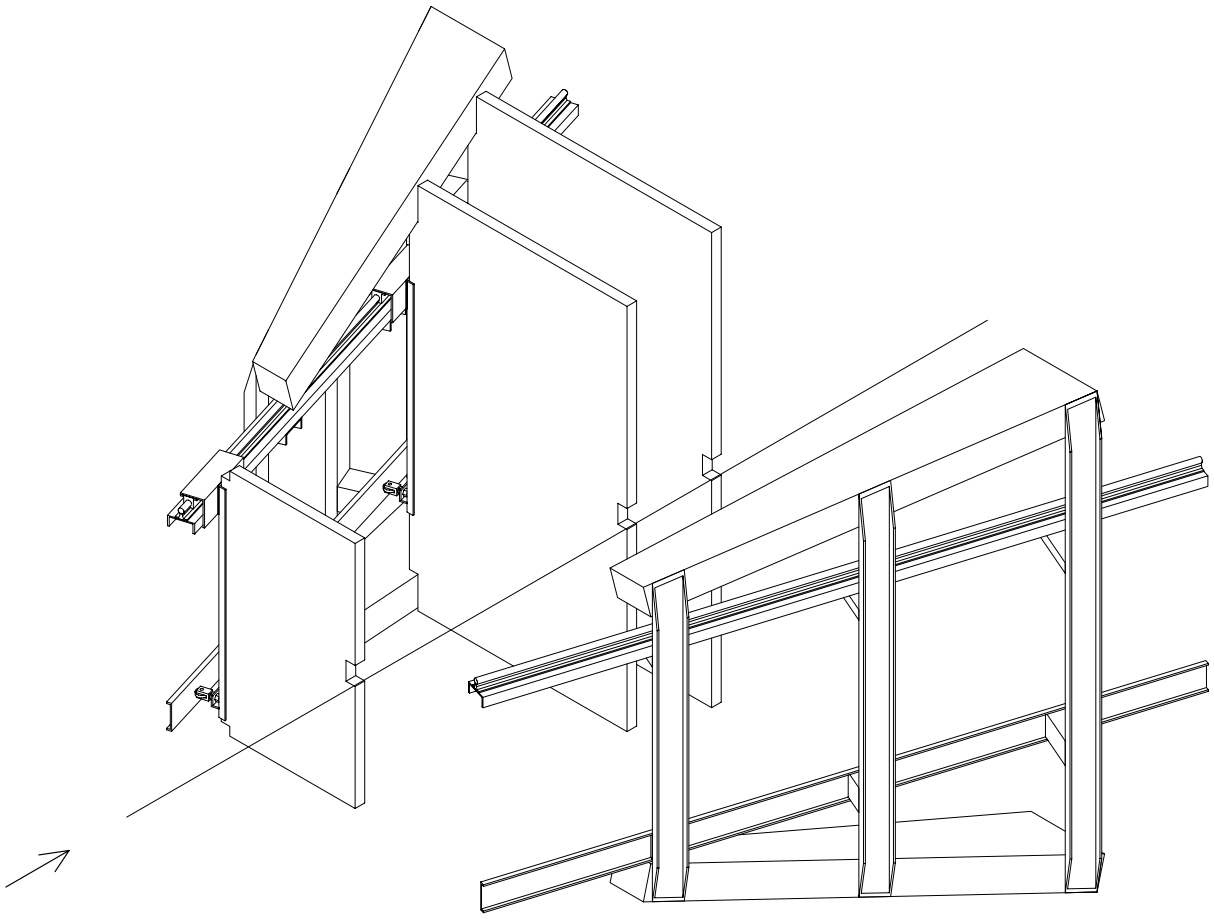

Figure 5.23: View of the mounting of magnet stations.

L0 trigger	
Output rate	1 MHz average
Latency	fixed at 4.0 μs
Dead time	no dead time for 16 consecutive triggers maximum
Format	One bit, clock synchronous distribution
L1 trigger	
Output rate	40 kHz average
Buffer depth	1927 events minimum
Format	Accept-reject in chronological order at L0 accept rate

Table 5.1: Trigger level parameters for the LHCb front-end system.

triggers. Important parameters for both trigger levels are summarised in Table 5.1.

5.3.1 Preamplifier

The ASDBLR chip [4, 5] has been selected as baseline solution. It contains 8 channels of preamplifier, shaper, discriminator and baseline restorer circuitry. The ASDBLR has originally been developed for the ATLAS Transition Radiation Tracker by the University of Pennsylvania. A detailed study [25] of its behaviour on Outer Tracker straw tube prototypes has shown that it matches our requirements very well. Its main characteristics are summarised in Table 5.2. The DC input impedance of the preamplifier is well-matched to the impedance of the straw tubes, but above 10 MHz the impedance of the preamplifier drops. As discussed in section 3.2, 150 Ω series resistors must be added at the preamplifier inputs for proper termination of fast signals. The chip is implemented in the DMILL process, which offers excellent radiation hardness, so it can safely be mounted directly on the detector. The differential outputs are capable of driving sufficient cable length to transport the discriminator signals off-detector. In order to avoid feedback from output cables onto the ASDBLR input stage, one would nevertheless install additional cable driver amplifiers in case the ASDBLR outputs would have to be transported off-detector. (That is *not* foreseen, but would become necessary in case of the fall-back TDC solution, which is not radiation hard.)

ASDBLR Properties		
Peaking time		8 ns
Input impedance	DC	270 Ω
	30 MHz	$\sim$ 180 Ω
Shaping time		20 ns
Dead-time		$\leq$ 40 ns
Radiation tolerance		30 Mrad
Output signals		differential

Table 5.2: Properties of the ASDBLR front-end chip. The quoted radiation tolerance applies only to the DMILL versions.

The designers of the ASDBLR have for the CDF Central Outer Tracker developed the ASDQ [6], which has very similar performance. It is made with the Tektronix Maxim SHPi process. This process offers less radiation tolerance but has a higher yield. The ASDQ is therefore cheaper than the ASDBLR, but it remains to be investigated if its radiation tolerance is sufficient for use on the Outer Tracker stations. The decision whether to use the ASDQ or ASDBLR is not critical because modification of the front-end electronics for either chip will be a minor effort.

5.3.2 Time digitiser

Unlike the other subdetectors in LHCb, which provide pulse height information, the Outer Tracker delivers hit times. Zero suppression of hit time data results in a major reduction of event data volumes and does not require complicated algorithms. It is performed early in the readout chain, upon L0 accept. Of course, zero-suppressed data vary in volume from event to event, which necessitates a system design with considerable safety factors.

TDC and L0 requirements	
Clock speed	40 MHz
Time resolution	< 1 ns
Readout window	50 (75) ns
L0 Pipeline depth	160 events
Trigger rate	1 MHz
L0 derandomiser depth	16 events
Event readout time	900 ns

Table 5.3: Essential requirements for the TDC and L0 buffers and logic.

The TDC chip also contains the L0 latency buffers, derandomisers and logic. An extensive description of the requirements of the LHCb L0 electronics is included in [50]. The main requirements for the TDC are summarised in Table 5.3.

The OTIS TDC

At the ASIC laboratory in Heidelberg, a dedicated TDC chip for the Outer Tracker (OTIS) is under development. The OTIS chip [7] has a clock-driven architecture, which is fully compatible with the LHCb readout electronics specifications. The chip architecture is depicted in figure 5.24. Hit signals appearing at the channel inputs are digitised and stored in a clock-synchronous pipeline buffer during the L0 latency. If no hit appeared in a clock cycle, a zero-word is written in the corresponding pipeline buffer location. Every channel has its own L0 pipeline, channels are not multiplexed except at the readout stage. Upon a L0 trigger, the event data are copied from the L0 pipeline to the derandomiser. Since the Outer Tracker has a signal collection time of 50 ns, two clock cycles will be read out for a single L0 accept. In order not to introduce trigger dead time, the derandomiser buffer has to have effectively twice the bandwidth of the L0 pipeline.

The derandomiser buffers are read out by the readout interface. It multiplexes hit data from the 32 channels and includes the header containing the bunch ID, chip identifier and channel hit map. Zero suppression after the L0 derandomisers is performed on the chip by removing zero-words from the data. The efficient data format makes it feasible to transport all L0 accepted data off-detector without having to install an excessive amount of bandwidth between the L0 and L1 electronics. In the case of very busy events, the OTIS can be protected against exceeding the specified maximum event readout time of 900 ns by truncating the event data. This does not cause hit losses, since the channel hit map is in the header of the event. However, fine time information of the flushed hits will be lost.

The chip features integrated DACs to provide the preamplifier chips with threshold control voltages. The programmable registers and DAC settings are accessible through the I2C bus interface. Because the OTIS is being developed in radiation hard 0.25 μm CMOS technology, it can be placed on-detector. Four ASDBLR preamplifier chips and one OTIS chip will be integrated on a single PCB serving 32 straw tube channels. In other words, a detector module of standard width (64 channels per layer) will carry four front-end boards on each of its end pieces.

The OTIS output interface is a 8 bit wide LVDS parallel bus clocked at 40 MHz. On the signal distribution board, the data from 4 OTIS chips are fed into the 32 bit wide input of a GOL chip [51]. The GOL features a radiation hard serial

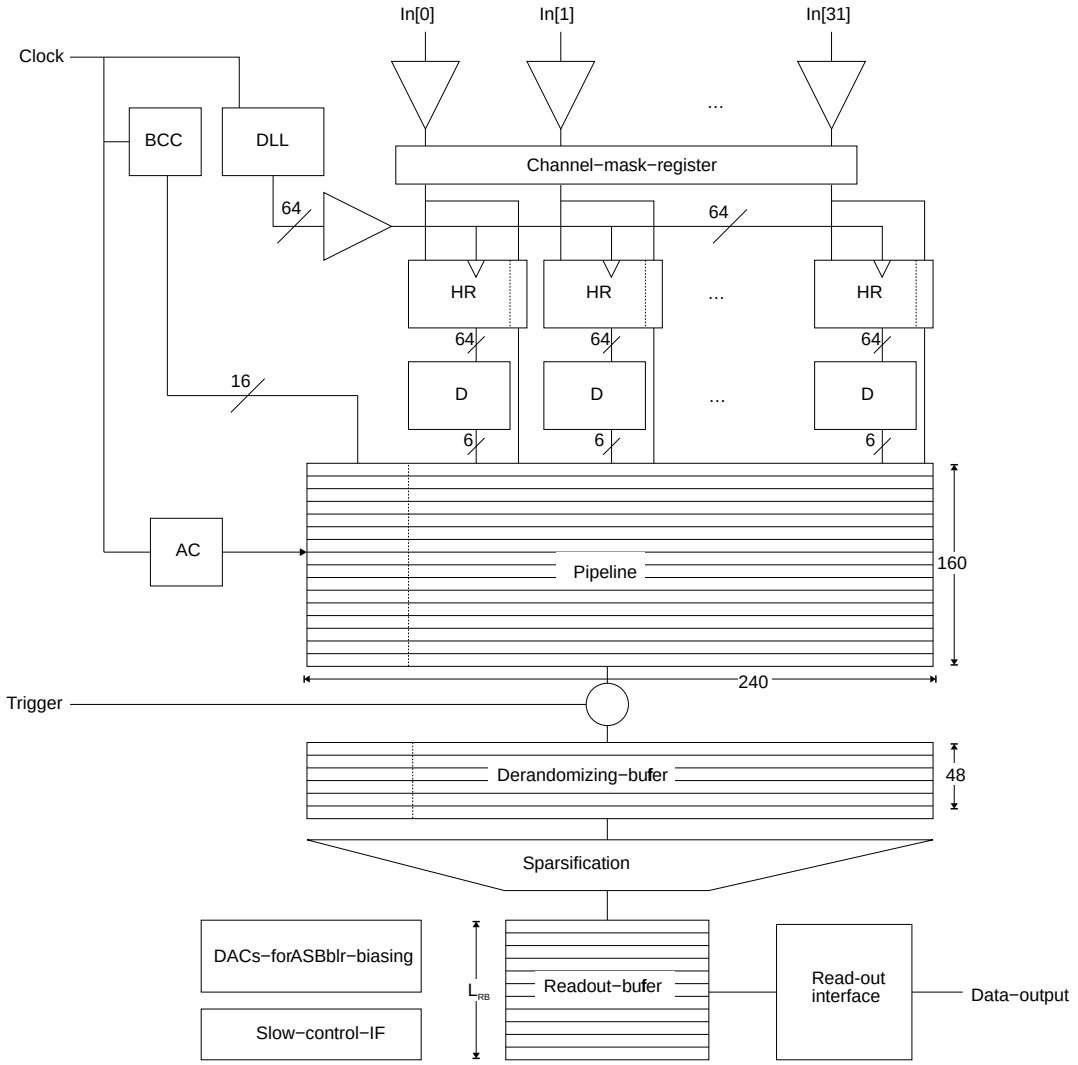

Figure 5.24: Architecture of the OTIS TDC chip. Upon a hit signal on the inputs In[x] the Delay Locked Loop (DLL) state which carries the fine time information is sampled by the Hit Registers (HR). The fine time is encoded in 6 bits and is transferred to the Pipeline by means of D-latches (D). Every clock cycle the Bunch Crossing Counter (BCC) value is copied into the pipeline. The slow control interface (IF) is compatible with the I2C protocol.

link driver which provides 1280 Mbit/s payload bandwidth over optical links. The layout of the OTIS based readout electronics is sketched in figure 5.25.

Fall-back solution

The OTIS chip, specifically designed to meet the Outer Tracker requirements, is still under development. Therefore, it was considered prudent to have a fall-back solution based on an already existing TDC at hand. It was determined that a readout system based on the HPTDC chip [8] developed at CERN can meet our requirements, although with less safety on hit rates and at higher system cost.

Figure 5.26 contains a schematic layout of the HPTDC chip. It is a 32 channel general-purpose design with a data-driven architecture. Every hit signal appearing on the channel inputs is given a time stamp which is multiplexed

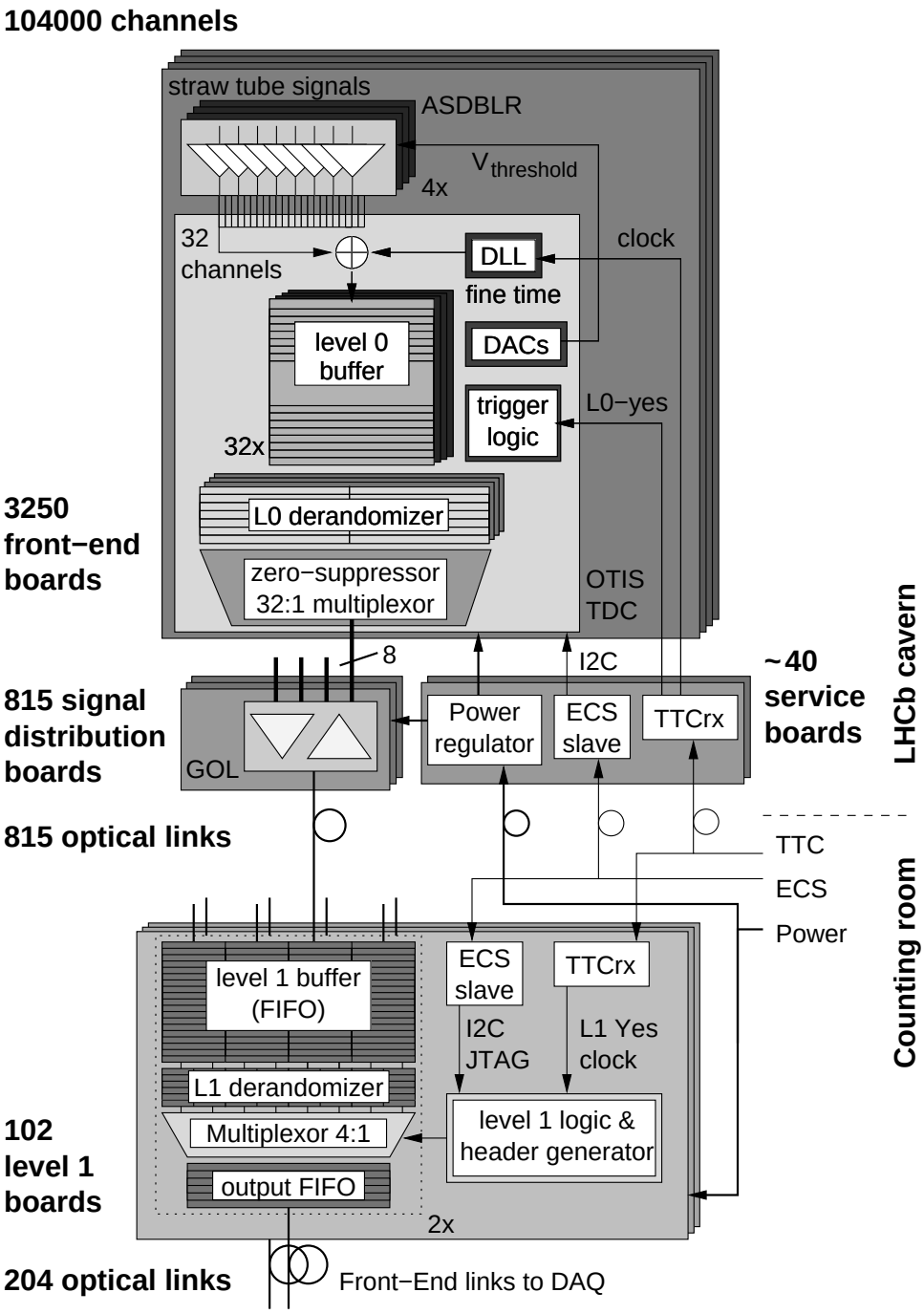

Figure 5.25: Layout of the LHCb Outer Tracker readout electronics based on the OTIS.

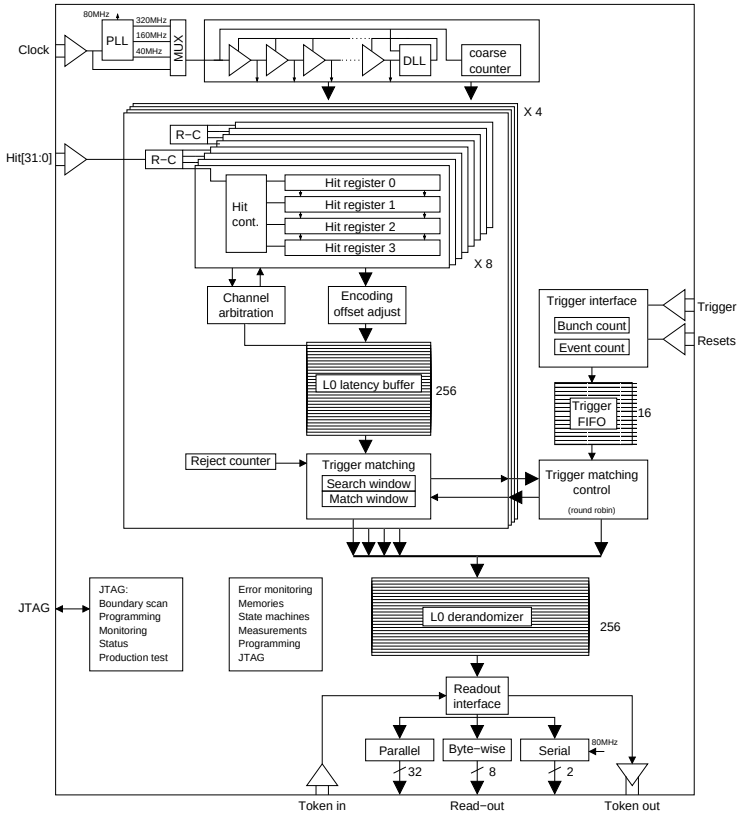

Figure 5.26: Architecture of the HPTDC chip.

and stored in the L0 latency buffers. Upon a trigger accept signal, buffers are scanned for hits belonging to that particular trigger and the matched hits are stored in the L0 derandomiser. A consequence of the HPTDC architecture is that the L0 latency buffers contain already zero-suppressed data.

HPTDC maximum hit rates		
Core clock	32 channels	16 channels
40 MHz	2 MHz	4 MHz
80 MHz	4 MHz	8 MHz

Table 5.4: Maximum recommended channel hit rates for the HPTDC with 32 or 16 active channels and different core clock speeds.

The data-driven and multiplexed chip architecture limits the maximum combined hit rate on all channels of a chip. When comparing expected channel rates with the maximum recommended HPTDC hit rates in Table 5.4, one sees that the hottest Outer Tracker regions will experience rates that are of the same order as the maximum channel rates the HPTDC can sustain when all 32 channels are utilised. Rate fluctuations on small time scales can then cause hit losses. The HPTDC is capable of serving in the Outer Tracker reliably if it is used with 80 MHz internal clock speed and if channels in hot regions of the Outer Tracker (about 25 %) are equipped with HPTDC chips with only 16 active channels. Another consequence of the data-driven architecture is that the event readout time depends on the number of hits in an event. Therefore, the Readout Supervisor cannot a priori protect the HPTDC from trigger losses in the case of very busy events.

The HPTDC has limited radiation tolerance. According to the specifications it can stand up to $\sim$ 30 krad integrated dose. The TDC boards

would have to be situated in near-detector electronics racks, to where the ASDBLR output signals would have to be transported. Each TDC board is designed to host four HPTDC chips.

The output data formats of the HPTDC and OTIS are very different, but anti-fuse FPGAs can convert the redundant HPTDC output data into a data format which resembles the OTIS event encoding. The FPGAs have a clock-synchronous 8 bit wide output bus like the OTIS, so four HPTDCs with accompanying FPGAs can be connected to an on-board GOL chip in a similar way as the OTIS. The L0 accepted data are transported towards the counting room where the L1 electronics are located. For either TDC the L1 system will be the same.

TDC choice

The main milestones and decision moments concerning TDC choice are summarised in Table 5.5. Submits of the timing and memory sections of the OTIS chip have been successfully tested in July 2001. The OTIS development schedule foresees a fully integrated prototype to be available for testing in spring 2002. Before that, further partial circuitry of the chip must be submitted and tested. The decision on TDC choice is foreseen in the second quarter of 2003, after testing of the final OTIS prototype.

A prototype test of a HPTDC based readout system [52, 53] will be completed before the end of 2001. Figure 5.27 shows a board with HPTDC chip and additional logic. In order to be ready for production by mid 2003, the decision on whether or not to proceed with full development of the HPTDC based system must be taken in summer 2002, on the basis of the test results of the first full OTIS prototype.

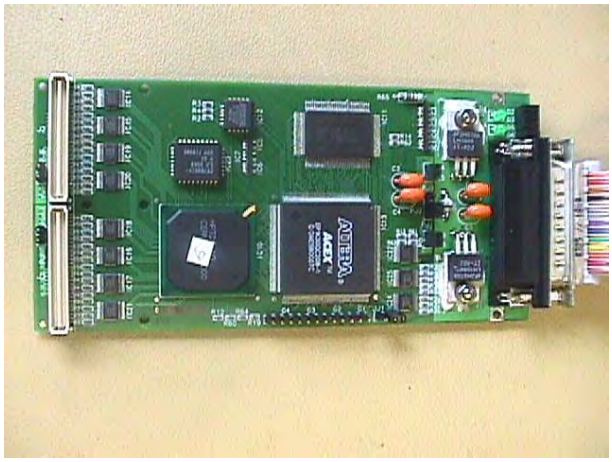

Figure 5.27: Prototype board with HPTDC chip and additional logic.

5.3.3 L1 electronics

The L1 electronics receives L0 accepted data from the TDC chip, checks data tags and flags any errors, buffers the data awaiting the L1 trigger decision and transports L1 accepted events to the DAQ system. The trigger parameters are summarised in Table 5.1. The depth of the L1 buffer is defined to be 1927 events minimum, which in practice means a depth of 2048 events. The design of the L1 electronics does not depend on the TDC choice.

All L1 electronics is will be located in the counting room. Because of the absence of high radiation levels, standard commercial components can be used. With modern high-performance FPGAs a compact implementation of the L1 logic can be achieved. The layout of the L1 electronics is sketched in the lower part of figure 5.25.

Given that the LHCb readout electronics architecture is clock-synchronous, correct time alignment of all front-end chips is essential. Therefore, data tags of incoming events are checked by the L1 electronics on correctness of the bunch and event counter values. Errors are flagged in the L1 header information. Upon a L1 trigger decision, rejected events are removed from the buffer memories and accepted data are multiplexed, formatted and transmitted to the Readout Units. With L0 and L1 trigger rates of 1 MHz and 40 kHz respectively, a multiplexing

Readout electronics milestones	
Functional test of full HPTDC readout chain	10/2001
Submit of full OTIS prototype	04/2002
Final decision on TDC choice	05/2003
Start production of electronics	06/2003

Table 5.5: Milestones in the development of OTIS and HPTDC based L0 electronics.

factor of 4:1 on the L1 boards does not introduce bottlenecks. The data rates quoted in table 5.6 include data formatting overhead and contain a safety factor of 2 in average channel occupancy.

S-links of 1 Gbit/s bandwidth transport data from the L1 electronics to the DAQ system. These links are either connected to the Readout Units (RU) or a Front-End Multiplexer (FEM). The FEM multiplexes front-end links with low average data rates onto a single RU input link to make more efficient use of the RU capabilities and limit the number of RUs required.

5.3.4 Controls

The TTC system [54] will provide the LHC experiments with fast control signals. The TTC front-end chip, the TTCrx (Timing, Trigger and Control ASIC), will be used to supply the LHCb front-end electronics with the following signals:

- 40.08 MHz LHC clock
- L0 trigger
- L1 trigger
- Reset signals
- Synchronous test signals

The functionality of the front-end electronics will be tested with pulses injected at the preamplifier inputs. The test pulse timing and the issuing of the accompanying triggers are taken care of by the TTC system. The segmentation of the TTC system is chosen such that it allows for stand-alone running, calibration, monitoring and debugging of the Outer Tracker sub-detector.

Apart from the fast controls, there is the Experiment Control System (ECS) which has the following tasks:

- Set threshold voltages of the preamplifiers
- Initialise the front-end electronics
- Set and read back programmable registers of front-end chips
- Read back status registers
- Read back data for debugging purposes

These functions are accessible through the JTAG or the I2C bus. LHCb aims to have only a few, standard ECS interfaces. In the counting room area, credit-card PC's will serve as ECS nodes providing the interface buses. For the electronics in the cavern, a radiation tolerant node of a general-purpose slow controls system such as SPECS [55] or CAN [56] will provide the slow controls interface.

5.4 Infrastructure

5.4.1 High voltage system

The granularity of the high voltage distribution system is a crucial issue in its design. If small

Item	Specification	
Detector parameters		
Total channel count	104000	
Maximum channel occupancy	<20%	
Average channel occupancy	5.5%	
Level 0 parameters	OTIS	HPTDC
Preamplifier chip count (8 channel ASDBLR)	13000	
Number of front-end boards	3250	1625
Location of front-end boards	On-detector	
Average level 0 accept rate	1 MHz	
OTIS (32 channel) TDC chip count	3250	
HPTDC chip count (32 or 16 channels used)		4100
Number of TDC boards	3250	1025
Minimum number of bits per digitised hit	8	
Multiplexing at level 0 output	4:1	
Level 0 $\rightarrow$ level 1 link type	optical	
Effective link maximum bandwidth	1.28 Gbit/s	
L0 $\rightarrow$ L1 link count	815	1025
L0 $\rightarrow$ L1 link average data rate*	500 Mbit/s	
Location of level 0 electronics	On-detector	Near-detector
Level 1 parameters	OTIS	HPTDC
Average level 1 accept rate	40 kHz	
Number of channels per level 1 input	128	
Level 1 accepted data multiplexing	4:1	
Number of level 1 boards	102	128
Level 1 average output data rate*	102 Mbit/s	
Location	Counting room	
Readout Unit interface	OTIS	HPTDC
Maximum RU input bandwidth	1 Gbit/s	
Front-End link (S-link) count	204	256
Number of RUs	<35	
Location	Counting room	

Table 5.6: Summary of the LHCb Outer Tracker readout. Differences between the OTIS and HPTDC based implementations are indicated in separate columns.
* Average data rates are calculated with a safety factor of 2 on channel occupancy, i.e. 11 % average occupancy is assumed.

groups of straw tubes are supplied separately, the amount of detector dead area remains small in case a channel failure necessitates high voltage switch off. The cost of cabling, patch panels and supplies, however, increases quickly with granularity. We have chosen to have one HV supply cable per module layer of 64 straw tubes. Two supply cables to different modules are fed by one branch of the distribution system, i.e. the true modularity of the HV system is 128 channels. Such a system can be built at acceptable cost [57]. In case a HV section must be switched off – which fuse protection of the individual straw tube channels should make a rare occurrence – two modules will loose one layer but will retain most of their efficiency, because the second layer is on a different HV section.

The system will consist of three main supplies which each control eight distributor units (figure 5.28). These units have 48 outputs (0-2.5 kV, 500 μA) with current monitoring and protection. They provide a cost effective way to increase granularity, with the possibility to operate sections of the detector at different voltages. The power supplies and distributor crates will be situated in racks in the counting room in the underground cavern. The distributor outputs will be connected to a patch panel in the counting room, which receives $3 \times 8 \times 48 = 1152$ HV inputs. Each input is at the panel split into two outputs to provide 64-channel rather than 128-channel cabling modularity. The outputs from this panel are connected to 2 or 3 patch panels near the detector via 48 cables of $\sim$80 m length, each with multi-wire conductors inside a total diameter of 2 cm. Straw tube modules are finally supplied from the detector patch panels by means of short ($\sim$ 15 m) local cables. High voltage distribution within the modules is described in section 5.1. Ground separation will be provided by a ground decoupling circuit at the detector side. It will break ground loops between detector stations and the counting room and also between different stations.

Straw tubes close to the beam pipe will experience hit rates up to 2 MHz. The average charge induced by a minimum ionising particle at the nominal voltage of 1550 V with the selected gas mixture will be about 100 fC. This corresponds to a maximum current of 200 nA per tube and a maximum current of 26 μA per HV section of 128 tubes. If a safety factor of 2 is included to account for a background of low energy highly ionising scattered particles and another factor of 4 to allow the possibility of a higher working point, a limit for a possible maximum current of 200 μA is obtained. Distributor modules that are able to provide a current of 500 μA can therefore be safely used.

In addition to providing a well-regulated voltage and DC current, the system should also include a variety of safety and interlock features that allow to turn off any supply that exceeds preset operating limits. The slow controls of the HV system will use the same protocols as other LHCb subdetectors. The main high voltage supply unit can be accessed by an Ethernet coupling and it provides control to the distributor units. The monitoring will certainly include operating voltage and current but may also provide information about the temperature and status of power supplies, the status of external interlocks, etc.

5.4.2 Drift gas system

The preferred operating gas is the non-flammable mixture $Ar(75)CF_4(15)CO_2(10)$. This composition has been used in various measurements in the test beam studies and fulfils the requirements of the detector in the LHCb environment. The basic function of the gas system is to mix the three components in appropriate proportions and to distribute the clean gas mixture into the individual Outer Tracker

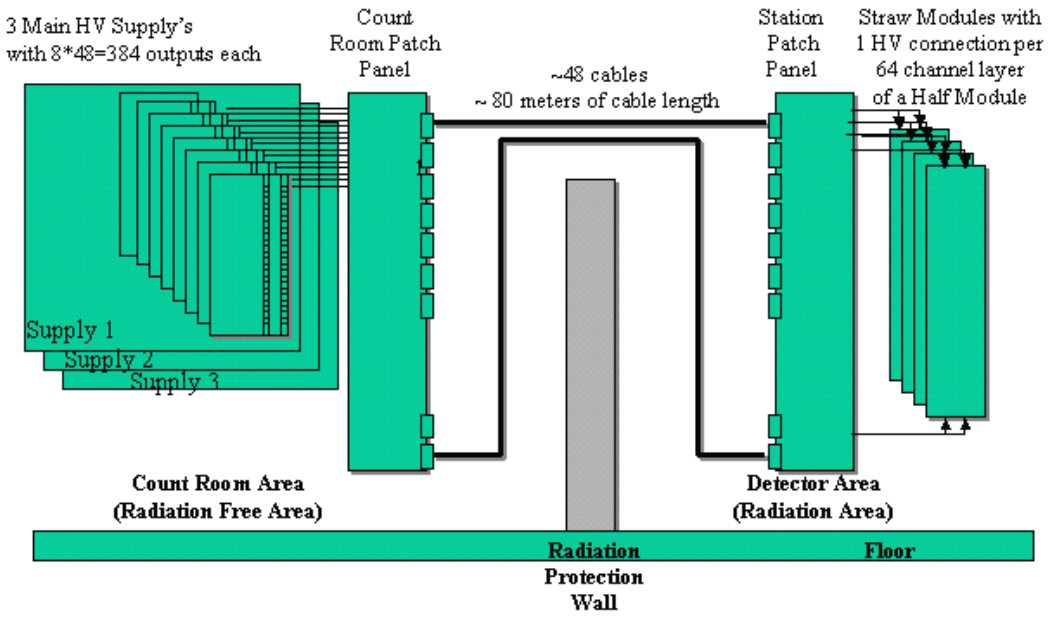

Figure 5.28: Block diagram of the high voltage system.

modules [58]. The total gas volume of 4.7 m^3, which comprises the straw tubes and the remaining volume of the modules, will be circulated in a closed loop system. This allows a sufficient gas exchange through the detector, in particular if the mixture contains a high cost component, tetrafluoromethane (CF_4). The gas system consists of a mixing module, situated at the surface in the gas building of the experiment, and a closed circulation loop, which includes the distribution, pressure regulation and purifier (Fig. 5.29). The distribution racks will be placed in the cavern behind the radiation shielding and are therefore accessible even during LHC running. There are 40 gas distribution channels to the detector. Each channel serves several Outer Tracker modules, where the number depends on the volume of the modules. The gas will be circulated with an expected regeneration rate of 90 % using in-line gas purification. An average gas exchange rate of one volume replacement every two hours is foreseen, which leads to a flow rate of 2.4 m^3/h. A pump in the return line allows the gas to be compressed to approximately 300 to 500 mbar overpressure, before returning to the surface and recycling through the purifiers. Either a frequency controlled pump or a back-pressure regulator in parallel to the pump controls the pressure to 0.3 mbar below atmospheric pressure at the inlet of the compressor. A set of twin purifier cartridges each filled with two cleaning agents will limit and stabilise the oxygen and water contamination in the gas. A humidity and an oxygen meter will measure the impurity concentration before and after the purifier. In order to monitor drift time stability and to allow on-line efficiency plateau measurements, boxes housing small straw tubes are implemented in the gas distribution system. The existing DELPHI supply and return pipes between the SGX building and the UX cavern will be reused by the LHCb experiment and hence for the Outer Tracker gas system. The gas control will follow the general recommendations of

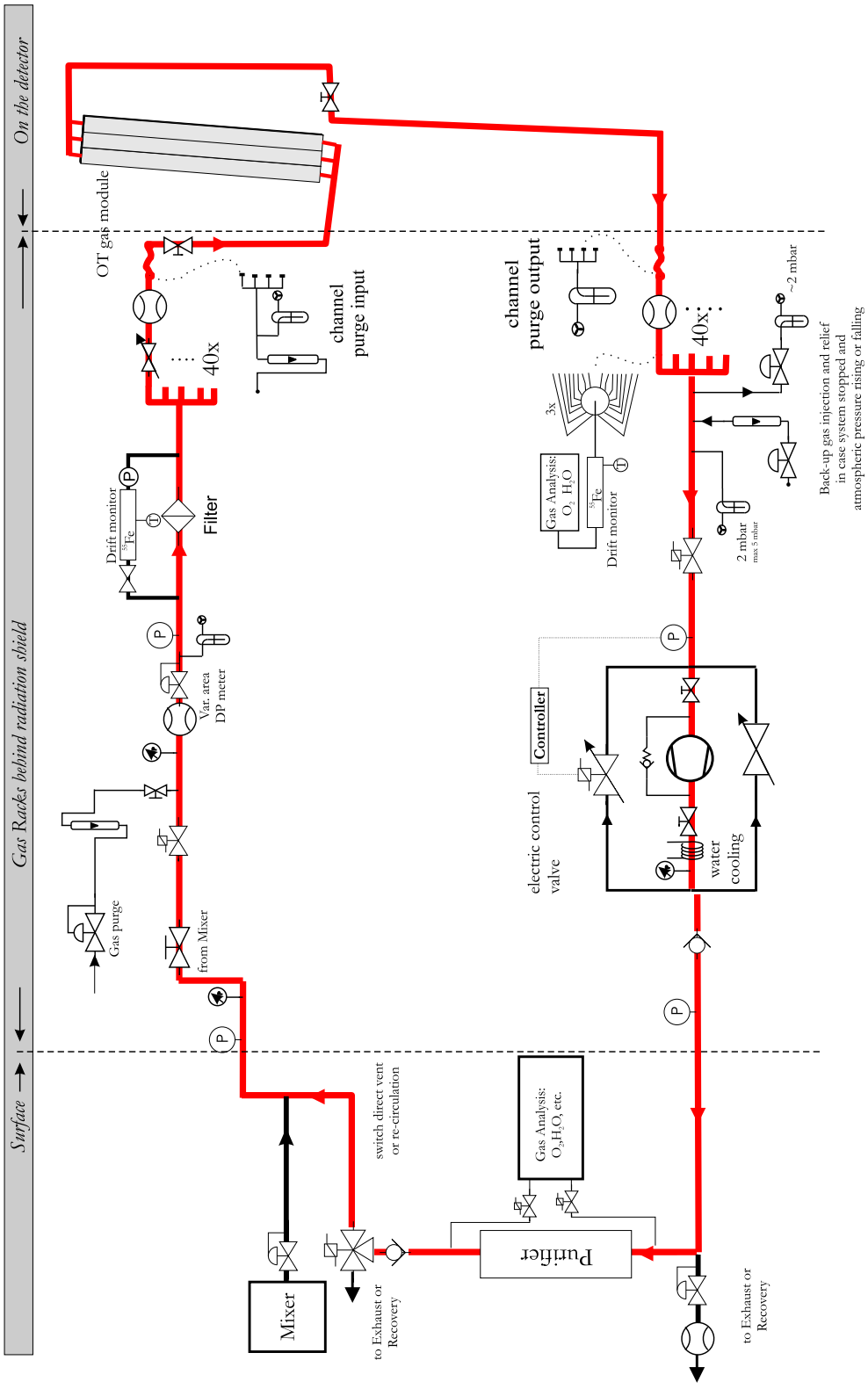

Figure 5.29: Schematic pipe and component drawing of the Outer Tracker gas system

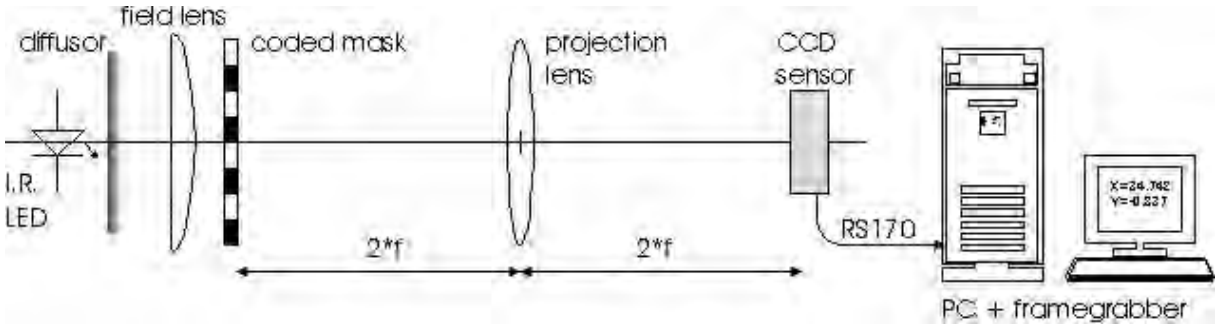

Figure 5.30: Principle of operation of the RASNIK alignment monitoring system

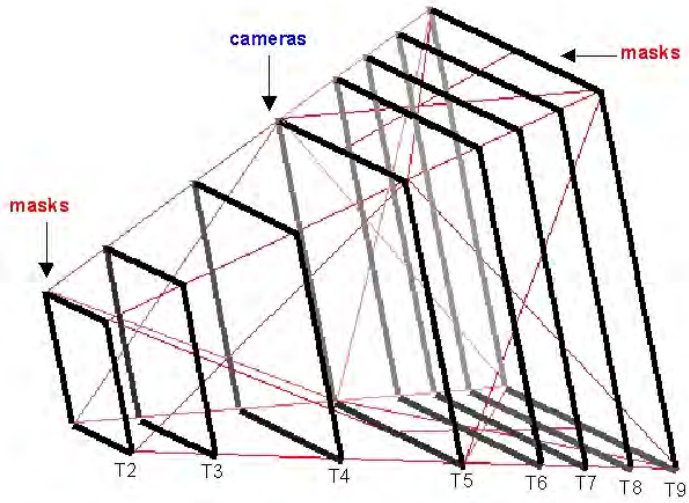

Figure 5.31: The design of the alignment system for the Outer Tracker stations T2 – T9 with 58 RASNIK monitor lines. The thick squares represent the frames of the stations.

the Joint-Control-Project of the LHC experiments (JCOP).

5.4.3 Alignment monitoring

Errors in the mechanical alignment of the detector components can significantly degrade the precision of track reconstruction and momentum measurement. While final alignment will be done on the basis of track reconstruction, it is considered worthwhile to monitor station alignment with a hardware system. Since it will register relative movements of stations as a function of time, its information is a valuable input for track reconstruction. A natural assumption for the required precision of alignment monitoring is that the alignment error should be smaller than the expected detector resolution for track measurements. The single cell resolution of about 200 μm translates in a resolution of $\sim$70 μm on station level in the optimum case where all eight layers register a hit. The alignment error should then be smaller than 30 - 40 μm for a negligible contribution.

The alignment system will be based on the RASNIK monitors developed at NIKHEF [59]. The basic idea of the RASNIK system is to project a finely detailed image through a lens onto a CCD camera, see figure 5.30. If any of these three elements moves, there will be a corresponding movement of the image on the CCD camera. The lightsource is a 3 x 3 grid of infrared-emitting LEDs. These LEDs illuminate a coded mask. The mask consists of black-and-white squares in almost a checkerboard pattern. Since only a small section of the mask is seen, the coded non-repeating pattern is used to obtain a unique position. The image is focussed with a simple convex lens placed near or at half-way point between the mask and the camera. Since the movement of the lens by a distance *d* in a direction perpendicular to the axis defined by the mask and the CCD camera causes displacement of the image of the mask by a distance *2d*, the transverse position of the lens can be calculated from the image position by means of image processing of a CCD pixel frame. Movements along the axis are measured by noting the change in the size of the image. The resolution in the longitudinal direction is better than 30 μm. The maximum transverse measurement range of the system is limited only by a diameter of the mask. Test bench measurements are reported in [60]. They show that the system provides stable and accurate measurements for alignment corrections. A resolution of 2-3 μm for the coordinates transverse to the optical axis was observed, with very good linearity and uniformity of the RASNIK response.

The proposed system is shown in Fig. 5.31. It consists of 58 RASNIK monitor lines [61, 62]. The frames T2, T5 and T9 are treated as reference frames. The masks are mounted on the T2 and T9 frames. All cameras are mounted on the T5 frame. The measured positions of the lenses mounted on all other frames allow the calculation of their displacement with respect to the reference frames. The RASNIK lines shown in Fig. 5.31 denote symbolically two or three physical RASNIK monitors shifted slightly in vertical position. The diameter of the RASNIK lines should be as small as possible, in order to fit in the limited space available for stations inside the magnet. Tests show that 3.5 cm diameter is sufficient for proper performance of the monitor with 5-6 m distance between mask and camera [60]. Station alignment will be monitored once every few minutes. The measurements will be stored in a data base that can be accessed by the track reconstruction software.

5.4.4 Safety aspects

The Outer Tracker detector will follow the CERN safety rules and codes, CERN safety document SAPOCO42 and European and/or inter-

national construction codes for structural engineering as described in EUROCODE 3. The following points were discussed in the Initial Safety Discussion (ISD) [63] with the CERN Technical Inspection and Safety (TIS) Commission:

1. The Outer Tracker gas mixture $Ar(75)CF_4(15)CO_2(10)$ is not flammable. The gas reservoirs under pressure will be located in the surface building. The gas distribution system will be built according to the appropriate rules.

2. All major loads will be checked by finite element calculation, such as ROBOT, and movable parts will be equipped with safety control.

3. The effects of Seismic activity will be studied in collaboration with TIS according to the response curve valid for CERN.

4. About 1152 HV channels will be run at 1.5 - 2.0 kV. The current per HV channel will be $\leq 200\mu A$. The low voltage supply to the detector read-out is below 3.5 V. The total power dissipation is $\leq$ 60 kW on the detector stations and $\leq$ 10 kW in the counting rooms in the cavern. Appropriate interlocks and current monitors will be installed together with interrupts at the source.

No major problems concerning the Outer Tracker design have been identified during the Initial Safety discussion.

6 Project organisation

6.1 Schedule

The project schedule is summarised in fig. 6.1. It covers the period from submission of this report to spring 2006, when the first LHC beam collisions are anticipated. The full set of tracking stations is scheduled to be commissioned and operating by that time.

Preparation for production

Several tasks remain on the road towards production readiness:

1. A straw tube module of the largest length, incorporating all design details and produced in a way that closely resembles the construction method for series production, will be built and tested before freezing the module design of stations behind the magnet (T6 – T9) in December 2001. The same holds for the modules that are to be used in the magnet region (T2 – T5).

2. Station installation and cable routing inside the magnet structure is complicated. It needs to be checked with installation of a prototype station frame inside a 1:1 magnet model. The model is expected to be ready by the end of 2001. There will also be a test assembly of the frame structure of one half of a track seeding station. This is foreseen in the first quarter of 2002.

3. The engineering design of modules and support structures will be reviewed after the tests mentioned above. Preparation of production drawings has started in summer 2001 and will be finished for all module variants by mid 2002. The drawings for the standard module of T6 – T9 will be ready in January 2002. A preproduction run of several modules of this type will serve to debug tools, fine-tune assembly procedures and reliably determine the throughput time per module.

4. A full prototype readout chain based on the HPTDC will be tested before the end of 2001. After verification of this fall-back solution, manpower will be concentrated on development of the preferred solution based on the OTIS TDC, for which the decisive test is planned in the first quarter of 2003.

Production

The Outer Tracker contains 560 straw tube modules: 256 modules (32 in each of the 8 stations) with single-sided readout above or below the Inner Tracker region, 304 modules (ranging from 8 in T2 to 56 in T8 and T9) with two-sided readout that span the full vertical acceptance. It is intended to have a further 10 % of replacement modules available by mid 2005, which adds up to a total of 620 modules. There will be five module assembly lines. At least two of these will stay operational beyond 2005 for further production of reserves when needed. Almost all parts will be ordered in industry. The production rate per assembly line is 1 module every 3 work days, the throughput time of a module including acceptance testing is 10 work days. The manpower needed for producing and testing of one module is estimated at 48 man hours. In principle, the sum of 620 modules can at the quoted rate on 5 assembly lines be produced in less than 2 years. One must anticipate that the real production time will be closer to 2.5 years due to occasional problems with tooling, parts delivery and man power availability. The schedule of fig. 6.1 allows for 3 years.

The production of station frame elements is a relatively light task. The smaller stations can be fully assembled at the module production site, but for the larger stations that is not a

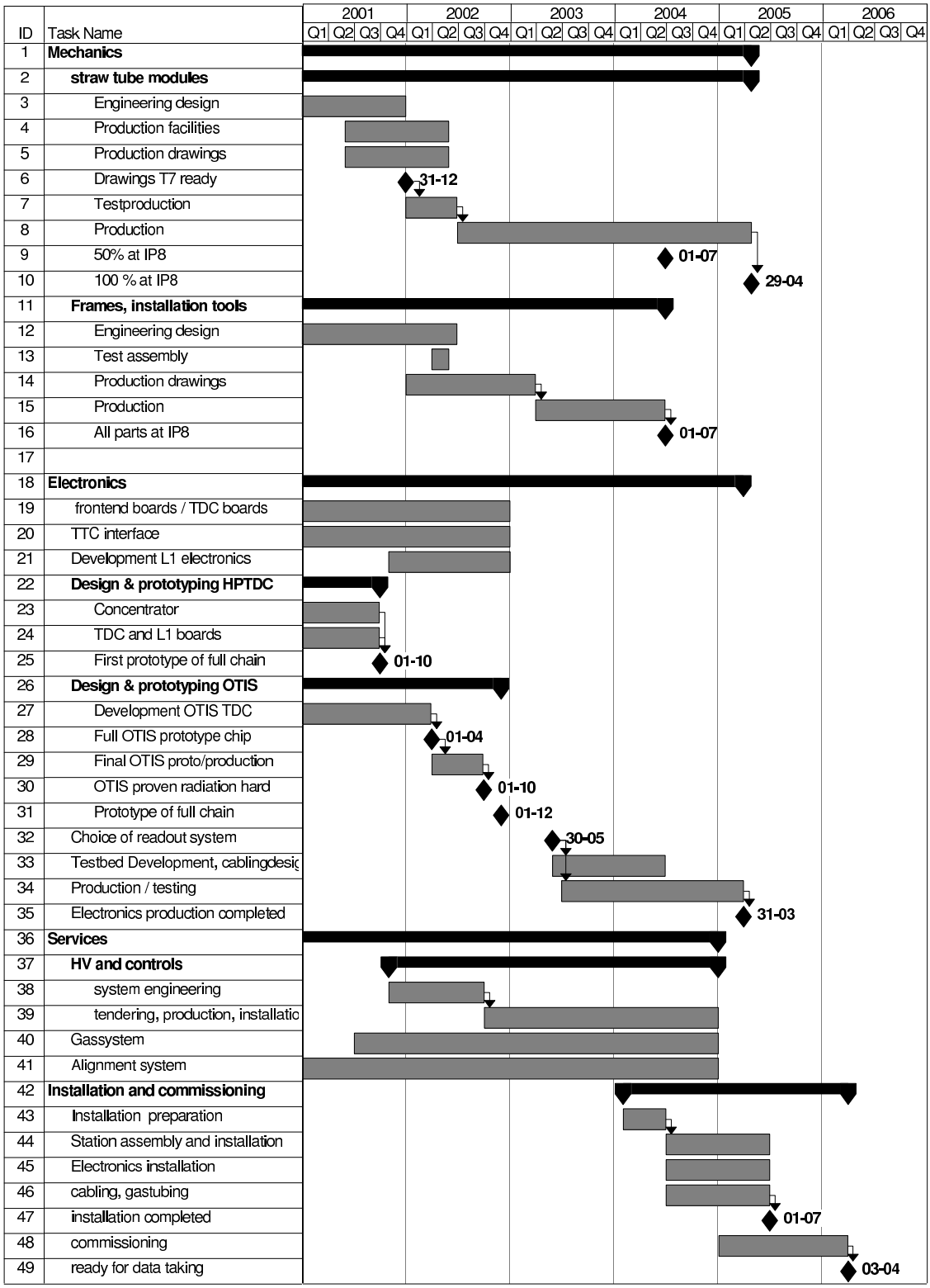

Figure 6.1: Outer Tracker project planning.

practical option. Modules and frame elements – all essentially 1-dimensional objects, easily transported and stored – will be assembled to full stations at CERN.

The choice of readout chain – based on OTIS TDC or on HPTDC – will be made in the second quarter of 2003. The HPTDC solution will be launched for production if it were to become evident that the OTIS chip would not be ready on time. Apart from the custom made OTIS TDC chip, no electronics components will be used that are specific to LHCb. We keep an eye on availability and delivery times of components. Production and testing of the readout electronics is scheduled to be completed by March 2005.

The components of the drift gas circulation system have been defined in consultation with the LHC Gas Group. The system does not contain exotic elements and will be ready before detector commissioning starts.

Installation and commissioning

All frame parts and modules for about half of the stations will have arrived at CERN from the production sites by mid 2004. Module deliveries will be completed in the second quarter of 2005. Assembly of the large track seeding stations T6 – T9 will take place at CERN. This includes frame assembly, mounting of modules and front end electronics, cabling at station level and tests after station integration on gas tightness, high voltage stability and electronics noise behaviour. The complete stations will be properly stored prior to transportation and final installation in P8. The CERN group will take responsibility for the necessary infrastructure for these procedures.

The magnet and the RICH 1 detector must be in place before installation of the tracker stations. Magnet installation and mapping of the field will indeed be completed before 2004 [49] and RICH 1 will by mid 2004 be in place [1]. Installation of all stations will take place between June 2004 and June 2005. The installation of stations T3 – T5 in the magnet region requires manoeuvring space at the location of stations T6 – T9. This does not mean that installation of the set T6 – T9 must wait, since these can easily be retracted from the beam pipe on their movable frame structure to allow room for insertion of T3 – T5 into the magnet gap. Readout electronics and services (drift gas, HV and LV systems) will be available to start commissioning of individual stations immediately after their installation. Full system commissioning (readout under common DAQ control, detector control through the ECS system, setting up of the alignment monitoring system) can start shortly after mid 2005, when all stations are installed.

6.2 Milestones

The project planning of fig. 6.1 is to our present knowledge realistic. Important dates are listed in table 6.1.

Timely completion of the project essentially hinges on two issues. First, the proper production rate of straw tube modules must be maintained. Given that module production will be spread over five sites, this will require close attention to logistics and quality control. Second, in order to keep sufficient time for tendering, production and testing of electronics, the TDC choice must not be delayed beyond the first half of 2003. The decision will be based on tests of a full prototype chain of each option, so the final electronics design can for either outcome be completed very soon after the TDC decision is taken. The project schedule leaves 9 months for system commissioning after installation of the last station.

Milestone	Date
Mechanics	
Engineering design of modules completed	12/2001
Engineering design of frames completed	6/2002
Start of module production	6/2002
Start of frame production	3/2003
All frame parts at IP8; start of station assembly	6/2004
Last modules to IP8	4/2005
Last station installed	6/2005
Electronics	
TDC choice	5/2003
Start of electronics production	6/2003
All electronics produced and tested	3/2005
Project	
Commissioning completed	3/2006

Table 6.1: Outer Tracker milestones

Task	Institutes
Mechanics	
Modules T2 – T5	Heidelberg, Krakow
Modules T6 – T9	Beijing, NIKHEF, Warsaw
Frames T2 – T5	Heidelberg, Krakow
Frames T6 – T9	Beijing (production), NIKHEF (design)
Electronics	
Before TDC	NIKHEF
From TDC to DAQ	
Baseline design	Dresden, Heidelberg, NIKHEF
Design of fall-back solution	Krakow, NIKHEF
Production and testing	Beijing, Dresden, Heidelberg, NIKHEF
Services	
Drift gas	CERN, Krakow
High voltage	CERN, NIKHEF
Alignment	Warsaw
Controls	NIKHEF
Installation coordination and infrastructure	CERN

Table 6.2: Sharing of responsibilities

6.3 Division of responsibilities

Institutes currently working on the LHCb Outer Tracker project are: NIKHEF, Amsterdam; Institute of High Energy Physics, Beijing; Research Centre of High Energy Physics, Tsinghua University, Beijing; CERN; Technical University of Dresden; Physics Institute, University of Heidelberg; Institute for Nuclear Physics and University of Mining and Metallurgy, Krakow; Soltan Institute for Nuclear Physics, Warsaw. The two institutes in Beijing will pool their resources and act as a single group.

The sharing of the main project tasks is listed in table 6.2. Specific Outer Tracker software developments for DAQ, controls and monitoring are understood to be included under the appropriate items. Track reconstruction software must be developed in a holistic fashion, not for the Inner and Outer Trackers separately. This work is done in the framework of a Tracking Task Force which is closely linked to the two hardware projects. The responsibility for detector mechanics (modules plus frames) is divided between two groupings of institutes. Heidelberg and Krakow take care of stations T2 – T5. NIKHEF, Beijing and Warsaw build stations T6 – T9. The principal development locations of the two options for the readout electronics are Heidelberg (baseline solution) and NIKHEF (fall-back solution). CERN will have responsibility for the drift gas and high voltage systems, for coordination of *in situ* assembly of stations and for installation coordination. Procurement will be centralised at CERN, Heidelberg and NIKHEF.

6.4 Costs

The total cost of the Outer Tracker system is 9.3 MCHF, see table 6.3. This is 10 % above the estimate in the Technical Proposal, but less than has been foreseen in the LHCb Memorandum of Understanding, which was prepared when the number of Outer Tracker channels went through a maximum. At that time the channel pitch had already been reduced, the number of detector planes not yet.

The mechanics costing includes the 10 % of spare detector modules that will be produced. Tools and consumables do not appear as an item in the costing table, since they are comprised in the production infrastructure provided by the participating institutes. In electronics, spares have been included by costing the system for 110 k channels rather than the installed number of 103.5 k. If it were to become necessary to adopt the fall-back solution, the cost of electronics would increase to 6490 kCHF for 110 k channels. The price difference of 920 kCHF with the baseline solution is due to increased cabling cost and a larger numbers of crates. The pricing of most major items, together representing about 70 % of the total cost, is based on preliminary quotes from industry or comparable recent purchases.

Item	Unit	Quantity	Cost (kCHF)
Detector modules			**2720**
Sandwich panels	m^2	1185	
Straw tubes	km	265	
Sense wires	km	265	
Wire locators	1000 pcs	500	
End piece mechanics	piece	1240	
End piece PCBs	board	1900	
Wire splitter PCBs	board	670	
Side strips	m^2	228	
Faraday cage	piece	950	
Glue	kg	400	
Conductive glue	kg	70	
Alu foil and other small parts			
Gas connectors, piping	module	560	
Assembly templates	piece	5	
Electronics			**5570**
HV boards	board	1720	
FE boards	board	3440	
ASDBLR preamp	chip	13800	
OTIS TDC	chip	3440	
Signal distrib. boards	board	860	
GOL chip	chip	860	
L1 boards	board	110	
Optical receivers	piece	880	
L1 buffer memories	piece	880	
L1 buffer controller FPGA	piece	880	
Multiplexer FPGA	piece	220	
S-link piggy back PCB	piece	220	
TTCrx and ECS interface	piece	110	
Crates (L1, control)	crate	16	
HV power	system	1	
LV power	system	1	
Cabling and connectors			
Frames and installation			**560**
Frames	piece	8	
Support T2 – T5			
Support T6 – T9			
Installation tools			
Services			**450**
Drift gas	system	1	
Alignment monitoring	system	1	
ECS	system	1	
TOTAL			**9300**

Table 6.3: Outer Tracker project cost. Boards are understood to include passive components and connectors.

References

[1] LHCb RICH Technical Design Report, CERN/LHCC/2000-0037, LHCb TDR 3.

[2] LHCb Technical proposal, CERN/LHCC 98-4 LHCC/P4.

[3] M.Benayoun. R.Forty and G.Wilkinson, "Tracking, tracker layout and RICH performance", LHCb 2001-100.

[4] B. Bevensee *et al.*, "Progress report on the development of a bipolar ASIC for the ATLAS Transition Radiation Detector", ATLAS note INDET-NO-080, September 1994.

[5] B. Bevensee *et al.*, "A Amplifier Shaper Discriminator with Baseline Restoration for the ATLAS Transition Radiation Tracker", IEEE Transactions on Nuclear Science, vol. 43, 1996.

[6] W. Bokhari *et al.*, "The ASDQ ASIC for the front end electronics of the COT", CDF Tracking note 4515, December 9, 1999.

[7] H. Deppe *et al.*, "Proposal for the LHCb Outer Tracker front end electronics", LHCb 2001-015.

[8] J. Christiansen, "High performance general purpose TDC specification", at http://micdigital.web.cern.ch/micdigital/hptdc/hptdc_manual.pdf

[9] J. Christiansen, "Requirements to the L0 front-end electronics", LHCb 99-29.

[10] L.G. Christophorou *et al.*, Nucl. Instr. and Meth. **163** (1979) 141.

[11] ATLAS Inner Detector Technical Design Report, CERN/LHCC/97-17, ATLAS TDR 5.

[12] S. Suvorov (HERA-B collaboration), private communication.

[13] M. Sans (COMPASS collaboration), private communication.

[14] U. Wiedner (COMPASS collaboration), private communication.

[15] G. van Apeldoorn, Th. Bauer and J. Steijger, "Aging studies of straw tube chambers", LHCb 2001-003.

[16] V. Talanov, "Absorbed dose levels in the LHCb detector", LHCb 97-017.

[17] L.Hajduk *et al.*, "First cross talk results for the Krakow chamber", http://chall.ifj.edu.pl/∼lhcb/outer.html

[18] V.Gromov and T.Sluijk, "Electrical properties of various types of straw tubes considered for the LHCb Outer Tracker", LHCb 2001-001.

[19] Rutger van der Eijk, "LHCb Outer Tracker prototypes", LHCb 2000-057.

[20] I. Gouz, L. Hommels and G.W. van Apeldoorn, "Beam tests of LHCb Outer Tracker prototypes in 2000", LHCb 2001-011.

[21] I. Gouz, Th. Bauer and L. Hommels, "Beam tests of a full-scale prototype of the Outer Tracker straw tube modules", LHCb 2001-098.

[22] L.Hajduk *et al.*, "OT prototype (May 2000)" and "Results for the second prototype", http://chall.ifj.edu.pl/∼lhcb/outer.html

[23] W.Hulsbergen *et al.*, "Calibration of Hera-B Outer Tracker chambers in a cosmic ray setup at NIKHEF", HERA-B note 00-014, 2000.

[24] T. Sluijk *et al.*, "The beam test electronics for the LHCb Outer Tracker", NIKHEF electronics report ERT 00/02/15.

[25] V. Gromov *et al.*, "Study of operational properties of the ASDBLR chip for the LHCb Outer Tracker", LHCb 2000-054.

[26] J. Christiansen, "32-channel TDC with on-chip buffering and trigger matching", talk given at 3rd Workshop on Electronics for LHC Experiments, London, England, 22-26 Sep 1997. In: Electronics for LHC experiments, London 1997, pp. 333-337.

[27] W.S. Anderson *et al.*, Nucl. Instr. and Meth. **A323** (1992) 273.

[28] H. Deckers *et al.*, "Beam test of honeycomb drift chambers", HERA-B note 98-060.

[29] http://consult.cern.ch/writeup/garfield/

[30] T. Sjöstrand, "High-energy physics event generation with Pythia 5.7 and Jetset 7.4", Comput. Phys. Commun. **82** (1994) 74.

[31] P.Bartalini *et al.*, "Tuning of multiple interactions generated by PYTHIA", LHCb 1999-028.

[32] QQ - the Cleo event generator, http://www.lns.cornell.edu/public/CLEO/soft/QQ

[33] http://lhcb-comp.web.cern.ch/lhcb-comp/SICB/html/sicbug.html

[34] GEANT Detector Description and Simulation Tool, CERN Program Library Long Writeup W5013 (1994).

[35] GAUDI User Guide, http://lhcb.cern.ch/computing/Components/Gaudi_v5/gug.pdf

[36] M.Merk *et al.*, "An improved digitization procedure for the Outer Tracker", LHCb 2001-055.

[37] M.Merk and M.Needham, "Occupancy Results with the new Outer Tracker simulation", LHCb 2001-085.

[38] R.Hierck, M.Merk and M.Needham, "Outer Tracker occupancies and detector optimization", LHCb 2001-093.

[39] J. van Tilburg, "Matching VELO tracks with tracks from the Main Tracker", LHCb 2001-117.

[40] R. van der Eijk *et al.*, "Performance of the LHCb OO track fitting software", LHCb 2000-086.

[41] R. van der Eijk *et al.*, "Addition of the vertex detector measurements to the track fit", LHCb 2001-021.

[42] O.Steinkamp, "A possible layout of an Inner Tracker silicon detector", LHCb 2000-109;
P.Sievers, "The LHCb silicon Inner Tracker", LHCb 2001-108.

[43] R. van der Eijk *et al.*, "Track Reconstruction for LHCb", LHCb 1998-045.

[44] R.Forty, "Track seeding", LHCb 2001-109.

[45] R.Hierck, "Track following in LHCb", LHCb 2001-102.

[46] R. van der Eijk *et al.*, "Performance of the combined LHCb track reconstruction algorithms", LHCb 2001-113.

[47] J. van Tilburg, "Matching VELO tracks with seeding tracks", LHCb 2001-103.

[48] http://lhcb-comp.web.cern.ch/lhcb-comp/SICB/html /AXSELECT.html

[49] LHCb Magnet Technical Design Report, CERN/LHCC/2000-007, LHCb TDR 1.

[50] J.Christiansen, "Requirements to the L0 front-end electronics", LHCb 2001-014.

[51] P.Moreira *et al.*, "G-link and Gigabit Ethernet compliant serializer for LHC data transmission". NSS 2000 paper, http://proj-gol.web.cern.ch/proj-gol/publications.htm.

[52] A.Zwart, "B-timizer, a 32 channel time digitizer with L1 buffer for the LHCb Outer Tracker chambers", NIKHEF electronics report ETR 2001-01, draft 1.0; recent version: http://www.nikhef.nl/∼albert/

[53] P.Kapusta *et al.*, "F1 simulation" and "Concentrator", http://chall.ifj.edu.pl/∼lhcb/electronics.html

[54] CERN RD12 collaboration, http://ttc.web.cern.ch/TTC/intro.html.

[55] D.Breton and P.Cros, private communication and presentation sheets at http://lhcb-elec.web.cern.ch/lhcb-elec/meetings/Electronics_workshop_jan01/agenda.htm.

[56] http://itcowww.cern.ch/SI/canbus/Welcome.html.

[57] T.Sluijk, "Proposal for a LHCb Outer Tracker high voltage system", NIKHEF electronics report ETR 2000/11/15.

[58] F.Hahn *et al.*," LHCb Outer Tracker gas system proposal", LHCb 2001-086.

[59] A. van der Horst and H. van der Graff, "Measurements on RASNIK", NIKHEF internal report, February 1995, and http://www.nikhef.nl/pub/departments/et/ccd rasnik.

[60] M.Adamus *et al.*, "The results of the RASNIK optical alignment monitoring system for the LHCb Outer Tracker detector", LHCb 2001-004.

[61] J.Mendys and M.Szczekowski, "Simulations of the optical alignment system for the LHCb Outer Tracker detector", LHCb 2001-005.

[62] M.Adamus, A.Nawrot and M.Szczekowski, "Alignment system for the Outer Tracker detector in the LHCb experiment", LHCb 2001-006.

[63] TIS-GS/WW/2001-013, "Initial Safety Discussion (ISD) for the LHCb Outer Tracker", 31/08/2001.